

FLORIDA INTERNATIONAL UNIVERSITY

Miami, Florida

ADVANCE SOLUTIONS FOR VOLTAGE CONTROL AND OPTIMIZATION  
IN SMART GRIDS

A dissertation submitted in partial fulfillment of the  
requirements for the degree of  
DOCTOR OF PHILOSOPHY

in

ELECTRICAL AND COMPUTER ENGINEERING

by

Temitayo Olayemi Olowu

2021

To: Dean John L. Volakis  
College of Engineering and Computing

This dissertation, written by Temitayo Olayemi Olowu, and entitled Advance Solutions for Voltage Control and Optimization in Smart Grids, having been approved in respect to style and intellectual content, is referred to you for judgment.

We have read this dissertation and recommend that it be approved.

---

Sumit Paudyal

---

Jean Andrian

---

Sakhrat Khizroev

---

Norman Munroe

---

Arif I. Sarwat, Major Professor

Date of Defense: September 16, 2021

The dissertation of Temitayo Olayemi Olowu is approved.

---

Dean John L. Volakis  
College of Engineering and Computing

---

Andrés G. Gil  
Vice President for Research and Economic Development  
and Dean of the University Graduate School

Florida International University, 2021

© Copyright 2021 by Temitayo Olayemi Olowu

All rights reserved.

## DEDICATION

To The Almighty God, for His mercies endureth forever, to my wife Oluwamayokun, my sons Samuel and Elijah, and my parents Gabriel and Rachael.

## ACKNOWLEDGMENTS

I would like to express my sincere gratitude to my advisor Dr. Arif Sarwat for his continuous support of my Ph.D study and related research, for his patience, and motivation. Besides my advisor, I would like to thank the rest of my thesis committee: Dr. Sumit Paudyal, Dr. Jean Andrian, Dr. Sakhrat Khizroev and Dr. Norman Munroe, for their insightful comments and encouragement to widen my research from various perspectives. I would like to thank my colleagues in Energy, Power and Sustainability Group for the various interactions and discussions we had during the course of my PhD. I am also grateful to Florida Power and Light, for giving me the opportunity to be part of various industry projects through their collaboration with my advisor. This dissertation was supported by the National Science Foundation under grant number 1553494, UGS Disertation Year Fellowship, and Petroleum Technology Development Fund (PTDF-Nigeria).

ABSTRACT OF THE DISSERTATION  
ADVANCE SOLUTIONS FOR VOLTAGE CONTROL AND OPTIMIZATION  
IN SMART GRIDS

by

Temitayo Olayemi Olowu

Florida International University, 2021

Miami, Florida

Professor Arif I. Sarwat, Major Professor

Voltage optimization and control of distribution networks is of uttermost importance to distribution system operators. The performance of the entire distribution network depends on the voltage profile of the system. The aim of this dissertation is to develop threefold advanced solutions that can effectively address and mitigate the voltage control and optimization issues of the smart grid. The first objective of this thesis is to develop accurate methods to quantify and analyze the expected variability of individual and aggregated PV systems which significantly impact the voltage profile of grid-interfaced PV systems. We develop an improved statistical formulation, propose the use of power spectral density and implement a new wavelet design using least squares optimization for PV aggregation and variability analysis. Using these proposed methods, we show that the aggregation results relay different percentages in reduction in the variability of the aggregated PV plants. The results show that the relative sizes of the PV fleets significantly impacts the reduction in intermittencies of the aggregated system by as much as 57%. The correlations between these sites significantly influences the reduction in variability of the aggregated PV systems.

The second objective is Mathematical modeling-based and Heuristic-based voltage control and optimization algorithms with coordinated use of SIs, OLTC/VR and capacitor banks for optimal power flow (OPF). These algorithms were validated using standard IEEE test feeders. The results of the proposed OPF algo-

rithms show the effectiveness of optimally coordinating multi-mode, multi-droop settings SIs with legacy voltage control devices on the same feeder for effective voltage control. Based on the case study, the results show that prioritizing the use of SIs can help optimize and efficiently use the existing legacy devices, reduce the number of tap changing by 28% and improve the capacitor bank utilization by 17%. The third objective is the development of design optimization algorithms for solid state transformers for distribution feeder voltage regulation and control. The proposed algorithms for medium/high frequency transformer optimization achieve efficiency above 98%. With appropriate selection of the design variables, power density of around  $4W/cm^3$  was achieved. The proposed simplified and cost-effective voltage regulation controllers were able to effectively regulate the output voltage around the desired value. A laboratory scale experimental setup is implemented to validate the proposed optimization algorithms and controllers with the experimental results in agreement with the simulation values.

## TABLE OF CONTENTS

CHAPTER	PAGE
1. INTRODUCTION . . . . .	1
1.1 General Statement of Problem Area . . . . .	1
1.2 Motivation and Purpose of Research . . . . .	2
1.3 Literature review . . . . .	3
1.4 Research Objectives and Original Contributions . . . . .	5
2. A REVIEW OF FUTURE CHALLENGES AND MITIGATION METH- ODS FOR HIGH PHOTOVOLTAIC PENETRATION . . . . .	9
2.1 High PV Penetration Challenges . . . . .	11
2.1.1 Challenges with Present Level of PV Penetration . . . . .	11
2.2 Envisaged Future Challenges of Very High PV Penetration . . . . .	12
2.2.1 Future Impacts of EVs . . . . .	15
2.2.2 Smart Cities . . . . .	15
2.2.3 Future Impact of Solar Eclipse with High PV Penetration . . . . .	16
2.2.4 Big Data, Communication and Cybersecurity Issues . . . . .	20
2.3 Existing Solutions with Future Directions . . . . .	22
2.3.1 The Use of MIR and RPFR . . . . .	22
2.3.2 DCI and Smart Inverter Functionalities . . . . .	24
2.3.3 Dynamic and Composite Energy Storage Systems . . . . .	25
2.3.4 Solid State Transformers . . . . .	27
2.3.5 Optimal Energy Routing . . . . .	29
2.3.6 Distribution Supervisory Control and Data Acquisition (D-SCADA) with Advanced Distribution Management System (ADMS). . . . .	30
2.3.7 Advanced Relay Communication and Protection Coordination (AR- CPC) . . . . .	31
2.3.8 Geographic Smoothing and Optimal Location of PV Systems . . . . .	32
2.3.9 Optimal Dispatch of Renewable Energy Sources . . . . .	32
2.3.10 Demand Response Management . . . . .	33
2.3.11 Big Data Solutions . . . . .	34
2.3.12 The Use of Artificial Intelligence . . . . .	36
2.4 Summary of Present and Future Challenges with Suggested Combina- torial Solutions and Future Direction . . . . .	37
2.5 Summary . . . . .	40
3. AGGREGATION OF PHOTOVOLTAIC SYSTEMS FOR INTERMIT- TENCY REDUCTION . . . . .	42
3.1 Introduction . . . . .	42
3.2 A Case Study and analysis of Four PV Sites located in Florida . . . . .	46
3.2.1 Aggregation Analysis . . . . .	48
3.2.2 Power Spectral Density Analysis . . . . .	52
3.2.3 Discrete Wavelet Application . . . . .	53
3.3 Summary . . . . .	56



4. OPTIMIZATION ALGORITHMS FOR SMART INVERTER AND VOLT- AGE CONTROL LEGACY DEVICES . . . . .	58
4.1 Optimal Power Flow Methods . . . . .	60
4.2 Mathematical modeling based Optimal Droop Setting of Smart Invert- ers in Coordination with Legacy Grid Devices . . . . .	61
4.2.1 Modelling of SI Modes and Settings . . . . .	61
4.2.2 Feeder voltage sensitivity analysis and modelling . . . . .	66
4.2.3 Optimal Power Flow Formulation . . . . .	69
4.2.4 Proposed Hierarchical Coordination . . . . .	70
4.2.5 2S-OPF . . . . .	71
4.2.6 2S-HOPF . . . . .	72
4.2.7 Simulation Results and Analysis . . . . .	75
4.2.8 Active and reactive power dispatch . . . . .	79
4.3 Heuristic-Based Optimization Algorithm . . . . .	84
4.3.1 Multi-Objective Optimization Formulation . . . . .	85
4.3.2 Constraints Formulation . . . . .	86
4.3.3 Test Feeder and Simulation . . . . .	87
4.3.4 Simulation and Results . . . . .	88
4.4 Summary . . . . .	91
5. MULTIPHYSICS AND MULTIOBJECTIVE DESIGN OPTIMIZATION OF MEDIUM AND HIGH FREQUENCY TRANSFORMER FOR SOLID- STATE TRANSFORMER APPLICATIONS . . . . .	94
5.1 Proposed Multi-Objective Optimization Algorithm and Theoretical For- mulation . . . . .	97
5.1.1 Design Optimization Objectives Formulation . . . . .	97
5.1.2 Design Optimization Variables and Constraints formulation . . . . .	100
5.2 Steady State Multiphysics formulation . . . . .	105
5.2.1 Electromagnetic Field Physics Model . . . . .	105
5.2.2 Thermal Physics Model . . . . .	105
5.2.3 Fluid Dynamics Model . . . . .	106
5.3 Simulation Results and Analysis . . . . .	106
5.3.1 Multiphysics simulation results . . . . .	110
5.3.2 FEA-based vs Analytical solution . . . . .	113
5.4 Experimental Implementation and Results . . . . .	114
5.5 Summary . . . . .	117
6. AC-AC MATRIX CONVERTER FOR SST . . . . .	119
6.1 Introduction . . . . .	119
6.2 Proposed control methodology and design of switching logic . . . . .	121
6.3 High Frequency Transformer Design and optimization with leakage in- ductance management strategy . . . . .	124
6.4 Simulations and Results Analysis . . . . .	127
6.4.1 HFT optimization results . . . . .	127
6.4.2 MC-based SST simulation results . . . . .	130
6.5 Summary . . . . .	131

7. VOLTAGE-CONTROLLED RESONANT DC/DC CONVERTER FOR SST APPLICATION . . . . .	132
7.1 Theoretical Analysis and modelling of resonant DC-DC Converter . . .	133
7.2 Proposed Voltage Regulation Controller . . . . .	135
7.3 Simulation Results and Analysis . . . . .	137
7.4 Experimental Results and Analysis . . . . .	139
7.5 Summary . . . . .	141
8. CONCLUSIONS AND FUTURE WORK . . . . .	142
8.1 Future work . . . . .	145
VITA . . . . .	171

## LIST OF FIGURES

FIGURE	PAGE
2.1 Top 10 PV installed capacities in the world [1] . . . . .	9
2.2 Solar PV net capacity additions by application segment, 2017-2022 [2]	10
2.3 Classification of various challenges with PV integration. . . . .	13
2.4 Top 10 Solar States in US (Installed capacity through 2020 in MW) [2]	14
2.5 A future scenario with high PV penetration. . . . .	14
2.6 The effect of 21 August 2017 on PV generators in the US. . . . .	17
2.7 The effect of 21 August 2017 on PV generators in the US. . . . .	18
2.8 Integration of an MIR . . . . .	24
2.9 Basic block diagram of an RPFR . . . . .	24
2.10 Block diagram of the integration of DCESS. . . . .	27
2.11 A conceptual design of a solid state transformer . . . . .	28
2.12 ADMS architecture and its typical features. . . . .	31
3.1 FEC 1.4 MW PV Located on FIU Engineering Campus . . . . .	47
3.2 PV fleet locations on Google map . . . . .	47
3.3 A 10-Day PV Power Output of the four PV plants . . . . .	49
3.4 Fleet relative variability of each PV sites and aggregation. . . . .	51
3.5 Fleet relative variability of each PV site and aggregation. . . . .	51
3.6 Fleet relative variability of each PV site and aggregation. . . . .	52
3.7 PSD Plots for the four PV Fleet. . . . .	53
3.8 PSD for the aggregated fleet. . . . .	53
3.9 Wavelet design based on a single day PV generation . . . . .	54
3.10 Variance estimation of the details discrete wavelet coefficients (a) Co- efficients 1 of individual PV sites (b) Coefficients 2 of individual PV sites . . . . .	55
3.11 Variance estimation of the details discrete wavelet coefficients (a) Co- efficients 1 of aggregated PV sites (b) Coefficients 2 of aggregated PV sites . . . . .	56
4.1 Volt-Watt curve. . . . .	62

4.2	Volt-VAR curve. . . . .	63
4.3	(a) SI operating region in Volt-VAR (P/Q priority) mode [3] (b) CPF operating quadrants for active and reactive power dispatch. . . . .	65
4.4	A distribution grid-connected PV systems with CAPS and OLTC/VR. . . . .	67
4.5	Flow chart of the proposed 2S-OPF algorithm. . . . .	71
4.6	Flow chart of the proposed 2S-HOPF algorithm. . . . .	72
4.7	IEEE 123 test node system with ten PVs integrated. . . . .	76
4.8	Optimal Tap positions on cloudy day for VR <sub>1</sub> -VR <sub>4</sub> (a) 2S-OPF (b) 2S-HOPF. . . . .	77
4.9	Optimal Tap positions on clear day for VR <sub>1</sub> -VR <sub>4</sub> (a) 2S-OPF (b) 2S- HOPF. . . . .	78
4.10	Optimal SI modes and Settings (a) cloudy day 2S-OPF (b) cloudy day 2S-HOPF (c) clear day 2S-OPF (b) clear day 2S-HOPF. . . . .	80
4.11	Optimal SI modes and Settings (a) cloudy day 2S-OPF (b) cloudy day 2S-HOPF (c) clear day 2S-OPF (b) clear day 2S-HOPF. . . . .	81
4.12	(a) P-Q dispatch cloudy day (b) P-Q dispatch clear day (c) P-curtailment (cloudy and clear day) . . . . .	82
4.13	Voltage Profiles of $PV_1$ and $PV_2$ on a cloudy day. . . . .	83
4.14	Voltage Profiles of $PV_1$ and $PV_2$ on a clear day day. . . . .	84
4.15	Total voltage deviation (a) Cloudy day (b) Clear day. . . . .	84
4.16	Proposed Heuristic-based optimization algorithm . . . . .	85
4.17	IEEE 34 node test feeder with PV locations . . . . .	88
4.18	(a) Voltage Profile of (a) Node 822 (b) Node 864 . . . . .	89
4.19	Voltage Profile of Node 840 . . . . .	89
4.20	Voltage Profile of Node 846 . . . . .	89
4.21	Voltage Profile of Node 848 . . . . .	90
4.22	Voltage Profile of Node 890 . . . . .	90
4.23	kVAR injection on nodes 844 and 848 by shunt capacitors . . . . .	91
4.24	Hourly losses in the system . . . . .	91
5.1	Schematic of a resonant LLC DAB Converter . . . . .	102
5.2	An LLC DAB converter equivalent circuit . . . . .	102

5.3	Gain curves of the resonant converter with $L_m/L'_1 = 5$ . . . . .	104
5.4	The proposed multiphysics-based, multi-objective optimization algorithm . . . . .	104
5.5	3D plot of the POS of the proposed optimization algorithm . . . . .	109
5.6	(a) Frequency sweep of POS at rated power of the HFT (b) Power sweep of POS at rated frequency of the HFT . . . . .	109
5.7	3D Surface plots based on Power-Frequency sweep of $HFT_1$ and $HFT_2$ 110	
5.8	Flux density distribution of $HFT_1$ and $HFT_2$ at rated power and frequency . . . . .	111
5.9	Temperature distribution of the HFTs with natural air colling velocity of 1 m/s (a) for $HFT_1$ (b) for $HFT_2$ . . . . .	111
5.10	Velocity distribution of the air around the HFTs (a) for $HFT_1$ (b) for $HFT_2$ . . . . .	112
5.11	FEA-based $HFT_2$ vs Analytical optimization result . . . . .	114
5.12	HFT implementation and experimental setup . . . . .	115
5.13	$HFT_1$ Resonant current and primary DAB converter switching pulses (a) Open circuit resonant current and switching signals (b) Short circuit resonant current and switching signals . . . . .	115
5.14	$HFT_2$ Resonant current and primary DAB converter switching pulses (a) Open circuit resonant current and switching signals (b) Short circuit resonant current and switching signals . . . . .	116
5.15	Input and Output Power at Low power level (a) $HFT_1$ (b) $HFT_2$ . . .	116
6.1	Switching modes for the proposed controller . . . . .	121
6.2	Schematic of a direct AC-AC converter with the proposed controller .	123
6.3	Flow chart of the proposed HFT optimization algorithm . . . . .	125
6.4	Optimal Frequencies vs Number of turns from Pareto solutions . . . .	127
6.5	Flux density distribution of the optimized HFT . . . . .	128
6.6	(a)3D plot of Pareto-optimal values of the objective functions (b)HFT's efficiency with varying frequency and output power . . . . .	128
6.7	(a) Plot showing the MC-SST input voltage, primary current, secondary voltage and secondary output current(b) Plot showing voltage across Primary switches and switching signal as well as the resonant current within the LC tank . . . . .	129
6.8	Plot showing voltage across secondary switches and their switching signals . . . . .	130

7.1	Converter equivalent circuit . . . . .	133
7.2	Surface gain plot of the resonant under varying load and frequency with $L_m/L'_1 = 5$ . . . . .	135
7.3	Conceptual plot of the proposed controller . . . . .	135
7.4	Six operation modes of the proposed controller . . . . .	136
7.5	Converter with the proposed controller . . . . .	138
7.6	Plot of changes in input voltage, regulated output voltage and resonant current . . . . .	138
7.7	Primary converter switches voltage and current . . . . .	139
7.8	Experimental setup to validate the proposed controller . . . . .	139
7.9	(a)Output voltage with input voltage set at 40V(b)Output voltage with input voltage set at 50V . . . . .	140
7.10	(a)Primary converter gate signal showing ZCS.(b)Plot of voltage across resonant capacitor . . . . .	140
7.11	Plot of input/output voltage and resonant current. . . . .	141

# CHAPTER 1

## INTRODUCTION

### 1.1 General Statement of Problem Area

The integration of large amount of PV systems comes with a number of challenges (on the feeders) which include voltage and frequency instability, reverse power flow, feeder losses, harmonics, complexity in protection coordination, thermal issues on cables amongst others [4, 5]. Several method of solutions have been proposed in literature to address some of these feeder issues at high level of PV penetrations. This include dynamic voltage control and optimization using PV smart inverters (SI), PV aggregation and fleet management and deployment of solid state transformers (SSTs) [6]. PV aggregation methods can be used to naturally reduce the variability in PV power output which can effectively reduce the feeder voltage fluctuations.

Studies have shown that aggregation of PV systems over areas with different weather parameters such as global horizontal irradiance (GHI), ambient temperature and cloud speed could provide a natural way smoothing out the output power of aggregated PV systems [7] . Effective aggregation of PV fleets largely depend on the correlation of the local weather parameters. Accurately quantifying the variability of the individual PV and aggregated PV becomes important in siting of the PVs for geographic smoothing as well as determining the optimal design of other solutions (such as energy storage systems) that need to be used to mitigate these fluctuations.

At high level of PV penetration, voltage control becomes a big challenge. The use of smart inverters (SI) have shown to provide an effective and economical way of voltage control. According to the IEEE 1547-2018, depending on the expected variability and level of PV penetration on the feeder, SIs are allowed to participate in voltage regulation alongside traditional legacy voltage regulating devices (such

as On/Off Load Tap Changers, Capacitor banks and Reactors) [8–11]. Optimal coordination of the operations of these voltage control devices becomes very important for effective voltage management on the distribution feeders. Also for voltage control (similar to SIs), SSTs are fast becoming a good alternative to traditional low frequency transformer for voltage regulation and control. Some of the benefits of SSTs include ease of control, bidirectional power flow, very high power density (significant reduction in transformer size as a result of high frequency operation), power factor correction, reactive and active power control, harmonic cancellation, voltage sag and swell mitigation among others [12, 13]. Though still plagued with some challenges such as lower efficiency, reliability as well as durability, SSTs are projected to be the future voltage conversion and control devices in the smart grid.

## **1.2 Motivation and Purpose of Research**

With increasing level of photovoltaic (PV) penetration, more voltage control responsibilities are being placed on SIs and other intelligent means of voltage control and optimization such as the use of solid state transformers. Traditionally, many electrical utility companies use transformers load tap changers (On/Off LTCs), voltage regulators, capacitor banks and reactors to carry out voltage regulation on their respective feeders. But, the drive towards achieving smart distribution systems has lead to the need for more intelligent voltage control and optimization techniques. Also, the use of Advanced Distribution Management Systems (ADMS) by utilities means voltage optimization of distribution systems can be executed remotely by updating the voltage control settings of grid-edge devices in order to achieve the optimal performance of the grid. This dissertation takes a three-fold approach to addressing voltage control and optimization issues on the grid. Since the voltage control problems with increased PV penetration is as a result of the intermittent nature in the power generation from the PV systems, this



dissertation tries to develop methods of analyzing and quantifying the variability of single and aggregated PV systems. PV aggregation under varying geographical weather parameters is capable of providing a relatively reduced variability in aggregated PV thereby reducing the possible fluctuation on voltage profile at grid level. The second approach proposed in this research is to develop voltage control and optimization algorithms that allows for an effective coordination of the use of SIs and existing legacy devices. While the third approach in this work is to develop control and optimization algorithms that improves the overall efficiency and power density of SSTs. SSTs provide ease of control, bidirectional power flow, voltage sag and swell compensation, DC port for PV and battery integration, harmonic mitigation and cancellation, power factor correction among other advantages compared to the traditional low frequency transformers.

### **1.3 Literature review**

The variability of aggregated PV systems is dependent on several factors such as the distance between the PV sites, the correlation between their irradiance and atmospheric temperature, the relative cloud speed, amongst others. Several methods for estimating the variability of aggregated plants over a wide area was developed by authors of [14–21] and validated. Their validation showed that the variability of these aggregated PV plants strongly depends on the correlation in the variability of each individual plants in the study. The study in [14] also showed that the correlation of individual plant depends on the time scale used as well as the separation between individual plants. The existing methods of quantifying the variability of single and aggregated PVs need to be improved based on their accuracy. Several SI functions have been proposed to allow for dynamic and autonomous control of the feeder voltage. These functions include the Volt-VAR (with and without a hysteresis band, with a rise/fall rate-of-change limit, with

an adaptive set-point, with a low pass filter rate-of-change limit), constant power factor (less than unity), dynamic reactive current injection (DRCI), Watt-Power Factor among others [9–11, 22–25]. The dynamic operation of SI voltage control depends on the curve selection for the desired voltage control setting. This makes the selection of the right coordinates of the curve of great importance. Also coordinating the voltage control between SIs and existing legacy devices becomes very important with increased penetration of PV systems. Though some algorithms have been developed, more work needs to be done on modeling the SIs for optimal power flow. Also for voltage regulation, solid state transformers are fast becoming an attractive alternative to the existing low frequency transformers. With the drive towards achieving a smart grid, the use of space efficient and intelligent power conversion and control devices becomes very important. According to [13, 26], some of the desirable features of SSTs include control of bidirectional power flow, ability to carry out reactive power compensation, harmonic cancellation and isolation, multi-port interfacing with DC sources and loads, voltage regulation, voltage sag correction, fault isolation etc. The galvanic isolation in SSTs is provided using the the high/medium frequency transformers (H/MFT). Various types of SST topologies have been proposed in literature, this include the direct AC-AC, AC-DC-DC-DC-AC, AC-DC-AC, and AC-DC-DC-AC topologies [26–28]. Some of the challenges associated in design of SSTs include their efficiency, cost and power density. Since the power transfer efficiency of SSTs depends on the efficiency of their H/MFTs, accurate numerical design optimization algorithms are very essential. Most of the H/MFTs algorithms in literature and based on analytical equations which often leads to less accurate optimization and high discrepancies between the simulation and experimental results. In order to make the cost of SSTs affordable for massive deployment on the distribution feeder, simplified controller are required. Most SST controls in literature often uses expensive controllers such as Digital Signal Processors (DSPs) and Field Programmable Gate Arrays (FPGAs).

## 1.4 Research Objectives and Original Contributions

In this research, threefold-solution that addresses distribution feeder voltage optimization and control are developed and implemented under the following objectives:

### 1. PV fleet aggregation variability analysis for intermittency reduction

Since the aggregation of PV systems with varying weather parameter is capable of providing a natural way of smoothing out the output of aggregated PV generation consequently improving the voltage profile, this objective seeks to analyze and quantify (using real data) different variability reductions that can be achieved using PV aggregation. This objective presents a three proposed methods for PV aggregation variability analysis. We use the Pearson correlation method to correlate the actual PV generation in order to calculate the correlation of the time series power output of four PV sites in Florida. An improved statistical formulation for aggregated PV variability estimation is proposed. The second method proposed for this analysis is the use of Power Spectral Density for analysis of the aggregated PV variability while the third approach involves designing a wavelet (for PV output) using least squares optimization for PV aggregation analysis. Using the aforementioned proposed approaches, this research analyzes the variability of four PV power plants located in Florida and their respective aggregation using real world data acquired from these PV plants.

These sites have different installed capacities and different irradiance correlation coefficients. The DC power output of each PV site are aggregated

with each other and the aggregation of the entire four PV plants is also analyzed. The results shows different percentages in reduction in the variability of the aggregated pairs of PV plants as well as the aggregation of the entire fleet of four PV sites. It also shows the impacts of the sizes of the aggregated PV sites on each other. This study will provide an insight into how utility-scale PV sites can be located and aggregated to reduce the variability of the entire fleet with higher PV penetration thereby reducing the effects of their intermittent nature on the grid.

## **2. Coordinated voltage control and optimization algorithms using Smart Inverters at High PV penetration.**

The use PV's SI provides an economical and more effective way of voltage control and optimization especially fast varying voltage fluctuation on the distribution feeder. Effective coordinated control of the SIs with existing voltage control devices in the grid becomes very important. This objective presents both mathematical modeling and Heuristic-based approach for voltage optimization on distribution feeders. The mathematical based approach formulates of four voltage control modes (Volt-Watt, Volt VAR P-priority, Volt VAR Q-priority, constant power factor (CPF: leading and lagging) for SIs. We proposed the use of Heaveside step function to model the rate of reactive and active power injection/absorption of the SI based on the voltage at the POI which is presented as part of the OPF formulation. Presents the first effort to explore a multi-mode and multi-droop settings SIs on the same feeder for effective voltage control and optimization. The proposed technique allows the SI to switch between modes and different droop settings at different hourly time scales in the optimization. We Propose a dual time-scale two-stage optimal power flow formulation with low resolution time scale (one-hour) for the CB, OLTC/VR, SI modes and settings operation and high resolution (one-minute) time scale for the active and re-

active power dispatch. This thesis presents the first effort in literature to model and co-optimize all the essential SI modes proposed by IEEE 1547-2018 on a single feeder and makes the SI modes control variables in the optimization formulation. We develop an Hierarchical Optimal Power flow algorithm. The proposed algorithm sequentially couples the optimization algorithm's three voltage control devices (SIs, OLTC/VR and CB). The SIs modes and settings are optimized first to enable them carry out the much of voltage regulation by using most of their available active and reactive power control capabilities. The CB status and the OLTC/VR tap position are optimized respectively afterwards. The first stage OPF is formulated as a Mixed Integer non-Linear Program (MINLP) while the second stage is formulated as a non-linear program (NLP). The proposed approach is validated using the IEEE 123, unbalanced three-phase test feeders. The result of the two proposed algorithms show the effectiveness of using a multi-mode, multi-droop settings SIs on the feeder for effective voltage control using both the 2S-OPF and 2S-HOPF. The 2S-HOPF algorithm provides improved voltage control using more of the SIs's resources by injecting/absorbing more reactive power, curtailing more active power consequently reducing the number of tap changing by 28% compared to the 2S-OPF algorithm. The 2S-HOPF also increase the CB utilization by  $\approx 17\%$  Using the Heuristic based approach, a multi-objective optimization technique for volt-Var control using genetic algorithm is presented. The proposed technique is implemented on the IEEE 34 bus distribution feeder. The simulation results showed a reduction in the overall system power losses, minimized reactive power injection, optimal SI power factor settings and ideal conservative voltage reduction.

### **3. Design optimization of solid state transformers for distribution feeder voltage regulation**

Similar to SIs, solid-state transformers (SST) can be used to effective voltage

control and regulation. One of the main challenges with the deployment of SSTs is their efficiency, cost and power density. In order to address these issues, this objective proposes a multi-physics-based, multi-objective optimization of high and medium frequency transformers (M/HFT) for SST application. The proposed method allows for improved efficiency and minimize the discrepancies in the simulation and experimental performance of the M/HFT. The M/HFT optimization algorithm (based on time-harmonic electromagnetic, thermal and fluid physics model coupling) minimizes the volume of the HFT, total cost as well maximizes its efficiency. A case study of  $20kW$ ,  $10kHz$  is investigated and its Pareto Optimal Solutions (POS) presented. The simulation results show the various dependencies of the design variables on the proposed objective functions which verifies effectiveness of the proposed algorithm. The POS show that efficiencies above 98% can be achieved with appropriate selection of the design variables. From the POS, two case studies of the HFTs (referred to as  $HFT_1$  and  $HFT_2$  using  $AMCC - 100$  and  $AMCC - 250$  amorphous cores respectively) are further investigated based on multiphysics numerical models. An experimental implementation of the optimized HFTs ( $HFT_1$  and  $HFT_2$ ) is integrated with a self-tuned dual active bridge converter to validate their performance. The experimental measurements from the HFTs are in very good agreement with the optimization results. This objective also proposes two novel controllers for DC-DC and AC-AC converters for SST application using resonant current control. The proposed simplified controller are cost-effective and can be implemented using simple logic gates eliminating the need for expensive DSP and FPGA controllers.

## CHAPTER 2

### A REVIEW OF FUTURE CHALLENGES AND MITIGATION METHODS FOR HIGH PHOTOVOLTAIC PENETRATION

The growing concerns for the depletion of the ozone layer and climate change [29, 30], partly caused by power generation from conventional sources, have stirred several projections by several countries for large-scale integration of renewable energy sources into their grids [31, 32]. Consequently, the proliferation of power generation from photovoltaics (PV) systems compared to other forms of renewable energy sources has increased in recent years [33, 34]. The fall in the prices of solar PV panels and the supporting policies made by various government of many countries have also aided the growth in PV deployments [35]. Figure 2.1 shows the top 10 countries with solar PV installations in the world. China, with abundant rare earth metals, accounts for almost 34% of the total world's installed capacity with more than twice that of United States (with the second largest PV installation capacity in the world).

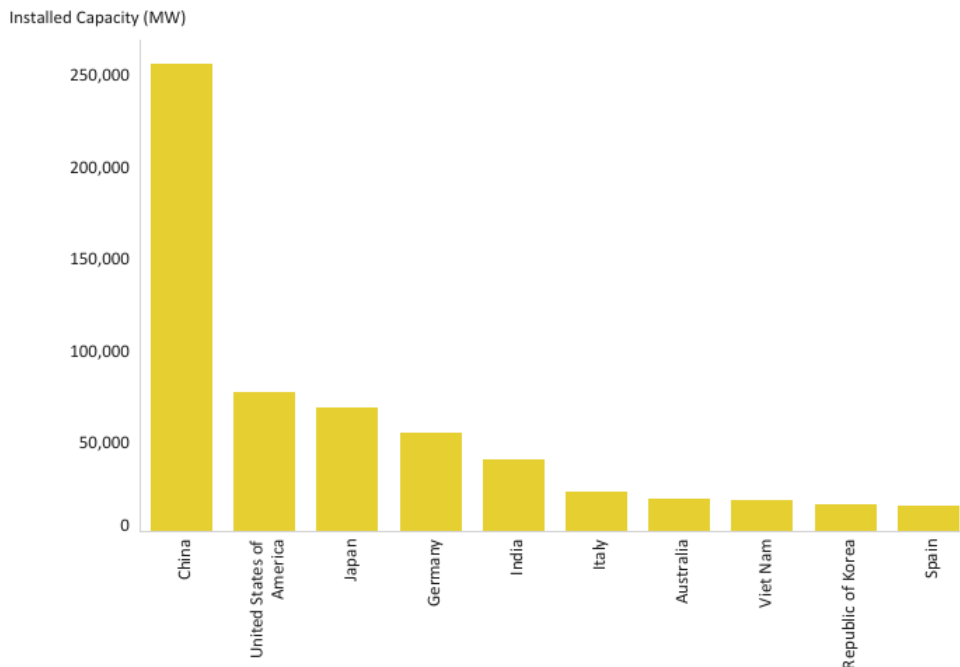


Figure 2.1: Top 10 PV installed capacities in the world [1]

Figure 2.2 shows a consistent increase in the installation and capacity addition of PV globally. Over 375 GW of PVs were installed between 2017-2019.



Figure 2.2: Solar PV net capacity additions by application segment, 2017-2022 [2]

A paper presented by [36] indicated that over half of solar installations in US are connected to the distribution system. According to [37], there was a 76% rise in residential PV installation capacity in the first quarter of 2015. In Germany, more than 70% of the installed PV total capacity is tied to the low-voltage (LV) distribution grid [38]. The increase in PV penetration into the distribution grid, however, has its own challenges. The severity of these challenges most times becomes aggravated with the increasing level of PV penetration [39]. These challenges also depend on the point of interconnection of the PV systems on the grid [40, 41], as well as the state and nature of legacy devices already installed on the grid. The proliferation of PV systems tied to the low voltage distribution grid makes it imperative to review the challenges (both present and future) on distribution grid network systems with high PV penetration and also propose some possible solutions to mitigate these challenges.



## 2.1 High PV Penetration Challenges

Various definitions for the PV penetration level have been presented in different studies. According to [42], PV penetration is defined as the ratio of maximum PV power to the maximum apparent power of the load. In [43], PV penetration is defined as the ratio of total PV energy generation to total energy generation. Cheng et al. [44] defines it as the ratio of total PV name-plate to the annual circuit peak load. Authors of [45] defines PV penetration on the low voltage network as:

$$PV_{pen} = \frac{S_{PV\ feeder}}{n_{loads} S_{peak}} \quad (2.1)$$

where  $S_{PV\ feeder}$  is the PV power installed under a given feeder,  $n_{loads}$  the number of consumers tied to the feeder, and  $S_{peak}$  an estimated value of peak PV power at the feeder. These definitions [42–45] are regarded as traditional definitions with several limitations according to [46]. The limitations in these definitions include the effects of PV in voltage regulation, the possible over-voltage due to earth fault and the possibility of islanding when there are light loads on the feeders.

Various works gave different percentage values as high PV penetration. Authors of [47] suggested values greater than 20% of total generation, while reports by [48, 49] consider high penetrations to levels up to 15% and 50%, respectively. Although there is no literary standard as to what percentage of PV penetration constitutes a high PV penetration, as a rule of thumb, many works suggest that at penetration above 15%, the challenges of high PV penetrations becomes noticeable [50, 51].

### 2.1.1 Challenges with Present Level of PV Penetration

Several countries have achieved some relatively high level of PV integration. Presently, Germany has about 20% with close to 50% of peak demand [52], California in the US have achieved 20–25% penetration [53], and Hawaii has already achieved a

19% with studies showing a possible 55% penetration [54]. Several studies have been carried out on the various challenges of the present level of PV penetration [4, 5, 38, 42, 55–78].

The intermittent nature of the PV output, its lack of inertia [79] like synchronous generators, and the unidirectional power flow nature of the distribution network present a huge challenge for high PV penetration. The summary from references [4, 5, 38, 42, 55–78] as presented in Table 2.3 shows the various challenges within the context of the present PV penetration level and its challenges, most of which are still incipient. The various challenges with PV integration is classified in to four segments based on their areas of impact as shown in Figure 2.3.

## **2.2 Envisaged Future Challenges of Very High PV Penetration**

Globally, there have been consistent increase in PV penetration by power utility companies. Figure 2.4 shows the present PV generation in 10 states in the US [1]. Nevada, California, Hawaii, and Vermont are all projected to have solar penetration levels above 20% by 2021 [80] and the total generation of 135 GW in 2040 in the US [2].

This continuous increase in PV penetration will obviously pose more technical challenges in the future, definitely more than what we have at the moment. With high level of PV penetration, a sudden change in cloud movement or an expected solar eclipse could lead to some serious ramping in the PV output. This could be as high as 60% of the power output in within a fraction of a second [81], and 63% of PV output capacity within a minute [82]. This ramping would have greater effects which a very high level of PV penetration—say 50%. New control strategies have to be developed to cope with these impending challenges. Improvements have to be made in weather forecasting in other to call into action storage facilities

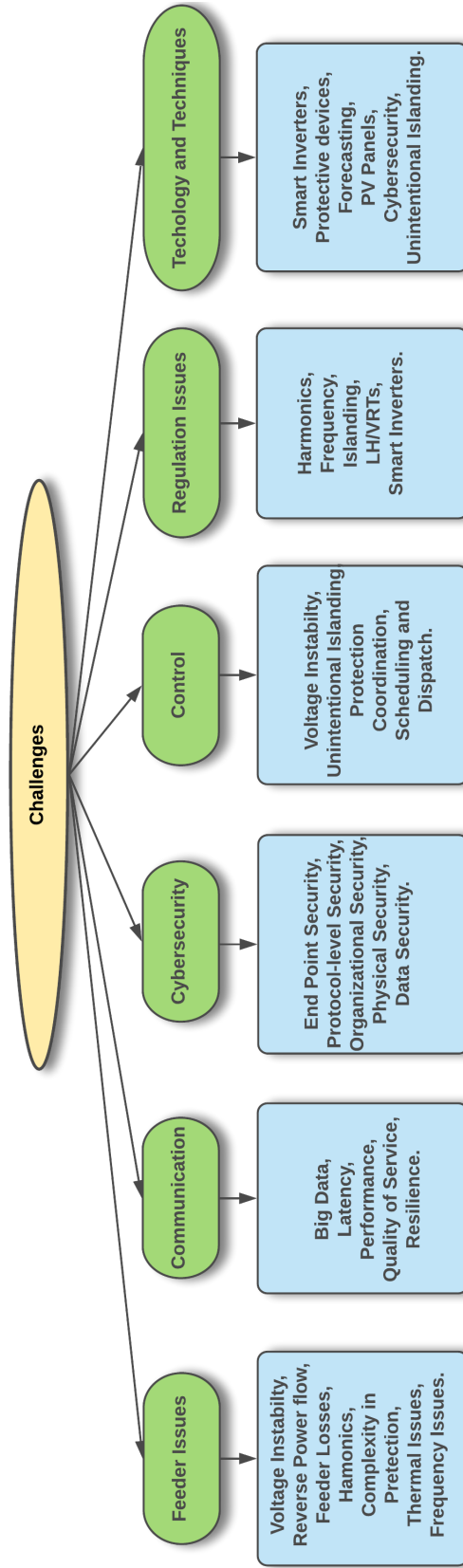


Figure 2.3: Classification of various challenges with PV integration.

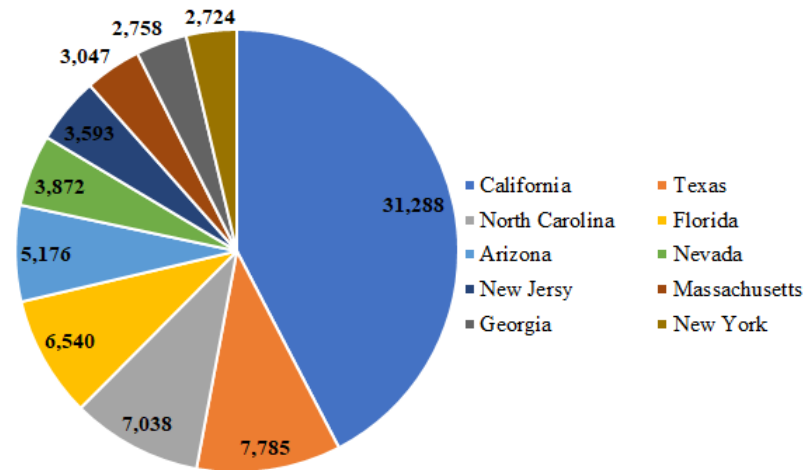


Figure 2.4: Top 10 Solar States in US (Installed capacity through 2020 in MW) [2]

and other forms of energy generations to mitigate the severe ramping of the PV output.

The increasing penetration of PV systems requires a proactive approach to the future scenarios. Figure 2.5 shows a typical future smart grid in the presence of more smart cities, smart home systems, plug-in hybrid electric vehicles (PHEVs), more utility-scale PV systems and increased prosumers.

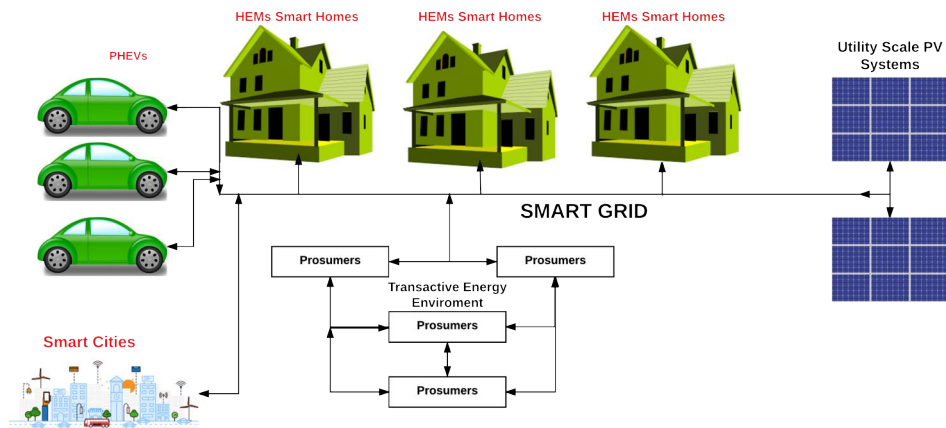


Figure 2.5: A future scenario with high PV penetration.

### **2.2.1 Future Impacts of EVs**

Since its launch in the automotive market in 2010, the use of EVs has increased drastically. Over 2.1 million of EVs were sold in 2019, with global stock of about 7.2 million EVs in use. Using the IEA mobility model, there's a projection of over 140 million units of EVs in the market by 2030 [83]. These vehicles are projected to drive the future of the automobile industry. Authors of [84, 85] suggested that EVs are inevitably going to play a major in the dynamics of the smart grid system in the future. A study carried out by [86, 87] showed the effect of various levels of penetration of EVs into the smart grid at different seasons of the year. When EVs are being charged or discharged in large numbers, there would definitely be some significant challenges on the overall grid stability and power quality [88]. Belmin Memisevic et al. [89, 90] showed that PEVs do have impacts in peak load and power losses, as well as overloading the transformers with a high level of EV penetration and uncontrolled charging. Though high PV penetration could help mitigate this power loss, it would violate voltage limitations through a period of high solar insulation. With companies unveiling their various on-road dynamic wireless charging technologies that would inevitably be powered with solar panels, the level of impact of these systems on smart grid with high PV penetration is yet to be ascertained.

### **2.2.2 Smart Cities**

Internet of Things (IoT) enabled smart cities would allow billions of devices and systems to be connected through the Internet [91]. The concept of smart economy, governance, people, mobility, buildings, services, infrastructure, surveillance, planning and environs means a whole new technical challenges for the smart grid with high PV penetration.

Achieving sustainable power supply for the realization of smart cities means the smart structures would have their own energy management systems [92]. Most of the buildings for smart cities are proposed to be Net-zero-energy buildings (NZEBS). These are buildings with extremely low energy demand. Such buildings are designed with very high energy efficiency. There is little difference in the energy demand by the building and energy supplied to the building can be made up by the installation of renewable energy (RE) systems on the building. A NZEB building can supply its excess power generation to the grid [93]. This is in tandem with the distributed energy systems for a smart grid. Many more rooftops, parking garage solar PV systems will be developed with the NZEBs.

There is also a projected increase in shared renewables such as community solar system [94]. These systems would form some micro grids that would also be integrated with the larger grid system for a bidirectional energy transfer. This would also usher in the new concept of the nanogrid which would enable individuals with power generation capabilities from renewable energy sources to become prosumers (both energy consumer and producer) [95]. There would be future clusters of several prosumers connected through the nanogrid to the main grid as shown in Figure 2.5.

With the certain dependence of smart cities on renewables, especially the use of PVs, the variability of PV power output is expected to pose some technical changes that have to be mitigated.

### **2.2.3 Future Impact of Solar Eclipse with High PV Penetration**

Solar Eclipse occurs when the moon (which is opaque) passes between the sun and the earth. The prediction of this occurrence is usually accurate with the time and areas to be affected known.

The first of such event that had a huge impact on PV generation happened on 20th of March 2015 in Europe. A total of 21 GW of power was lost within 90 min [96], while Germany lost 9 GW of installed capacity within 75 min [97]. Many continental European countries also had some slight frequency stability issues during the eclipse [98]. Another solar eclipse occurrence is expected in Europe by 2021 and 2026. There is a projection that the total PV installation in Europe will rise to 170 GW and 250 GW by 2021 and 2026, respectively [99], As a consequence, the occurrence of an eclipse in 2021 and 2026 eclipse would be more challenging.

The 21 August 2017 solar eclipse in North America also came with its own challenges. A report by [100] showed that PV power generation from utilities fell by 3.5 GW and rooftop solar installation power lost an estimate of 1.5 GW in California. North Carolina's generation was estimated to drop from 2.5 GW to 0.2 GW. Figure 2.6 [101] shows how the obscurity of the solar eclipse affected the PV power generation in 10 states in the US. The obscurity was estimated as a percentage of the scenario with total solar eclipse .

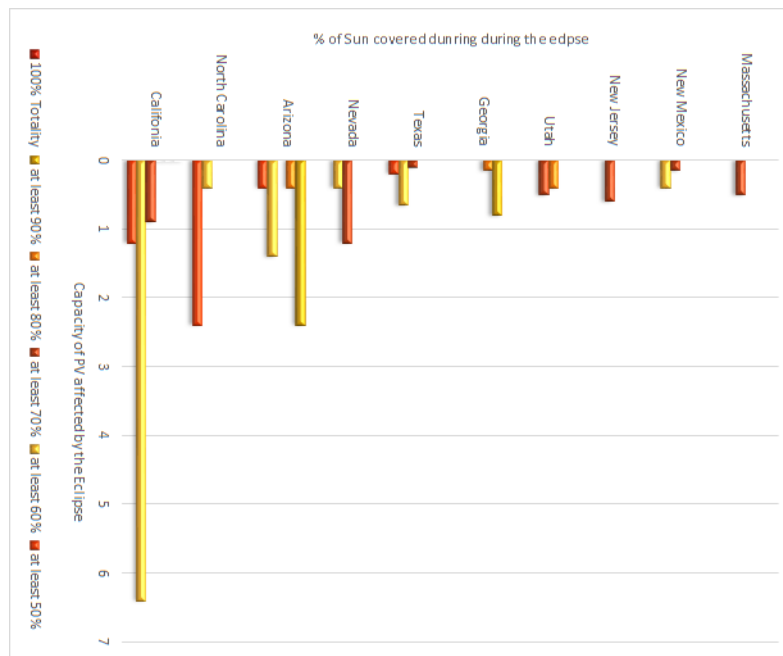


Figure 2.6: The effect of 21 August 2017 on PV generators in the US.

Figure 2.7 shows the data plot of the actual AC power generation from two PV sites in Florida. One of the PVs (System A), with an installed capacity of 1.2 MW, is located on Florida International University (FIU), Engineering Campus while the other with a name plate capacity of 356 kW (System B) is located at Daytona in Florida. The FIU PV site showed a total drop in power generation of 660 kW within 60 min (1:45 p.m. to 2:45 p.m.). That is approximately a ramp

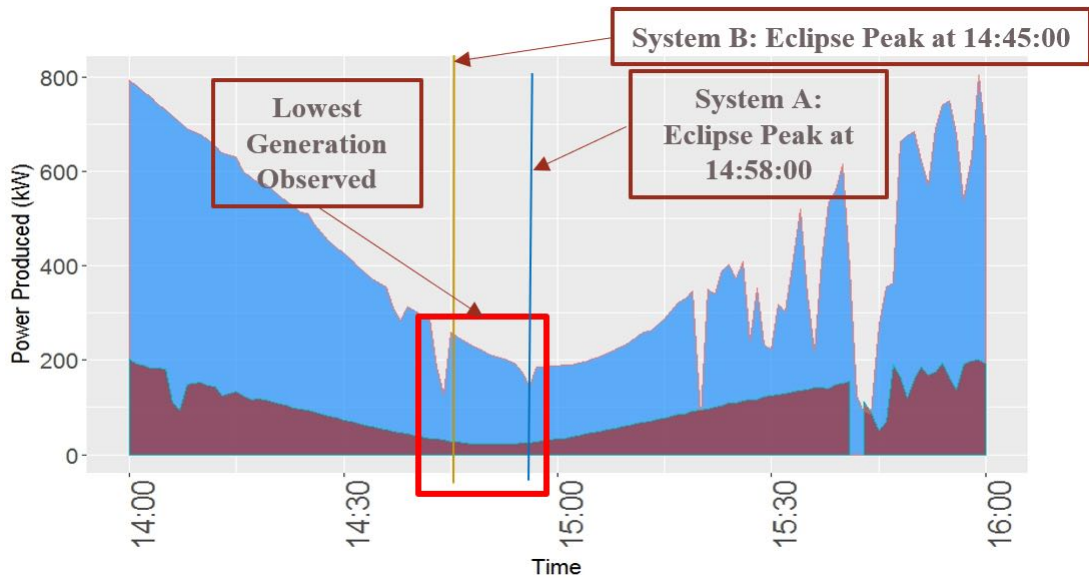


Figure 2.7: The effect of 21 August 2017 on PV generators in the US.

rate of 11 kW/min. The other PV site in Daytona ramped from 251 kW at 1:00 p.m. to 25 kW at 2:58 p.m. This is equivalent to a ramp rate of 2.3 kW/min. The present level of penetration of the FIU PV is approximately 16%, based on the load on the feeder where the PV is connected. An impact study of this event was carried out. The system was able to cope with the loss in power generation. The power quality at the point of interconnection wasn't compromised. Obviously, with higher level of penetration, such occurrences will pose more challenges to the grid. The North American continent is also expected to witness another solar eclipse on the 8th of April 2024 [102, 103]. It is projected, with the present PV installation growth, that the total utility-scale PV generation in the US would rise to 50 GW by 2022 [2]. This implies that no less than 50 GW of PV capacities is expected to be connected to the grid when the next solar occurrence would occur



in 2024. The ramping effects of 21 August 2017 solar eclipse events were mitigated with adequate forecast and preparations. Several other sources of power such as fossil fuel were used to offset the drop in power generation so as to maintain power system stability [100].

With the increased drive towards a higher level of PV penetration, it is quite obvious that the technical challenges of future occurrence of solar eclipses will be more prominent. This chapter takes a look at the various challenges that could impede the stability of the smart grid with high level of PV integration and proposes several solutions that would help mitigate some of these issues. The GridWise transactive energy (TE) framework (Version 1.0) [104] defined the TE as a future electrical system (infrastructure) where the balance of supply and demand is achieved in a dynamic way. This is done within a framework of economic and control mechanism and each of the operators in the transactive environment gets value for their participation (inputs). The smart grid dictionary [105] also defined TE as a *'software-defined grid managed via market-based incentives to ensure grid reliability and resiliency. This is done with software applications that use economic signals and operational information to coordinate and manage devices' production and/or consumption of electricity in the grid. Transactive energy describes the convergence of technologies, policies, and financial drivers in an active prosumer market where prosumers are buildings, EVs, microgrids, VPPs or other assets.'*

Future TE scenario would involve total decentralization of the energy power flow. A multidirectional path for electricity would evolve. The TE architecture allows prosumers to transact energy within themselves at the distribution levels. TE would lead to the deployment of home energy management systems (HEMSs). A future TE scenario would involve total decentralization of the energy power flow. A multi-directional path for electricity would evolve. The TE architecture would allow prosumers to transact energy within themselves at the distribution level [106]. Most prosumers in the TE environment would have rooftop PV systems.

The TE framework would encourage the proliferation of prosumers which would consequently increase the level of PV penetration. This future scenario with the nature of PV power generation is expected to pose a whole new challenge on the smart grid.

#### **2.2.4 Big Data, Communication and Cybersecurity Issues**

With increasing PV installations (both utility scale and rooftops), real time data acquisition and transmission becomes very crucial for efficient monitoring, management and control. The next decades will usher in the installation of hundreds of thousands of devices for different data-related purposes. This would consequently lead to some big data, communication and cyber-security challenges.

##### **Big Data**

With increasing penetration of distributed energy resources (DERs), such as PV in smart grid, there would obviously be an astronomical increase in the volume of data. These include, consumer energy utilization pattern data, smart meter data, data for managing, control and maintenance of devices (such as PMUs, IEDs, relays, etc.) data from generation, distribution and transmission networks, and operational data . These volume of data as a result of increasing PV penetration conforms with the seven big data characteristics, which are

1. Volume: There is an increase in the size of the data (smart inverter data, PV generation data, weather data, temperature data, data for forecasting, etc.) due to increasing PV penetration.
2. Velocity: The speed at which these data need to be acquired and transmitted increases. There is a need for real time control and data acquisition.
3. Variety: There is an influx of data from different sources. There is heterogeneity in the data sources including data from weather stations, PMUs,

inverters, meters, power quality meters and other sensors. They usually have different format and structures which need to be processed.

4. Veracity: The accuracy of the data being transmitted and introduction of noise from the devices and other external sources.
5. Volatility: The length of time to store the acquired data.
6. Validity: This refers to the timeliness of the data, i.e., the value of the data is bound by time, after which it becomes irrelevant or invalid for processing.
7. Value: This refers to the end contribution of the smart grid big data in terms improving grid reliability, efficiency and resiliency.

## **Communication**

The importance of an efficient and reliable communication architecture in a smart grid cannot be overemphasized . There is certainly no realization of a smart grid without adequate and efficient communication infrastructure and network. With increasing PV penetration, the need for a highly efficient communication architecture becomes imperative. According to , the main requirements for communication infrastructure include an adequate Quality of Service (impacted by latency and bandwidth), interoperability, scalability, security and standardization. The massive data intrusion as a consequence of increased PV penetration could affect the Quality of Service (QoS). Achieving low latency (time delay in data transmission) and adequate bandwidth while maintaining adequate efficiency and reliability becomes a very big challenge.

## **Cybersecurity**

The influx of large data across the network, as a consequence of increased PV penetration, poses some cyber-physical challenges. The deployment of communication infrastructures for data transmission and acquisition creates vulnerabilities

for cyber attacks. Usually, the attackers try to take the advantage of the vulnerable parts of the communication architecture by attacking both the measurement and control signals . For instance, a cyber attack on smart inverter communication and control signal on a feeder that has high level of PV penetration could lead to voltage and frequency instability. Smart inverter settings (such as Low/High Voltage Ride Through, Frequency Ride Through, Volt-VAR, and Frequency-Watt) remotely controlled through a Supervisory Control and Data Acquisition System (SCADA), could be changed by an attacker, which could lead to a cascade of stability problems in the grid .

## **2.3 Existing Solutions with Future Directions**

Several solutions have been proposed in literature to address these challenges. Obviously more work still needs to be done, especially in the future scenarios earlier mentioned. Table 2.1 shows a list of acronyms based on literature and some suggested solutions.

Amongst the solutions that have been proposed and deployed over the years with suggested future directions include:

### **2.3.1 The Use of MIR and RPFR**

The minimum import relays are relays that are designed to disconnect grid-tied PV connected systems whenever their output falls below a particular threshold value. It's also used to trip the grid-tied PV system from the network whenever their output goes above the 25% of the actual service load. Figure 2.8 shows a typical set up of how the MIR can be integrated with a grid-tied PV system [46]. The MIR communicates with the grid-tied inverter system to disconnect whenever the output falls below a threshold value. While the RPFR is designed to disconnect the grid-tied PV system when the power flow from the utility falls

Table 2.1: Acronyms for Solutions.

MIR	Minimum Import Relay
RPFR	Reverse Power Flow Relay
SI	Smart Inverter
<i>SI<sub>LC</sub></i>	Smart Inverter with Load Control
SI+DLHC	Smart Inverter with Dynamic Load Harmonic Control
D-SCADA	Distribution Supervisory Control and Data Acquisition
AMI	Advanced Metering Infrastructure
ADMS	Advanced Distribution Management System
ST	Smart Transformer
ARCPC	Advanced Relay Communication and Protection Coordination
FRT	Fault Ride Through
OER	Optimal Energy Routing
IED	Intelligent Electronic Device
DCESS	Dynamic and Composite Energy Storage Systems
GS	Geographic Smoothing
VVWO	Volt-VAR/Watt Optimization
DERMS	Distributed Energy Resource Management System
GIS	Geographic Information System
CIS	Customer Information System
STLF	Short Term Load Forecasting
SE	State Estimation
MDMS	Meter Data Management System
FLISR	Fault Location, Isolation and Service Restoration
OMS	Outage Management Systems
CRM	Customer Relationship Management

to zero or changes to the opposite direction. This relay trips to prevent back feed upstream of the feeder or to neighboring feeders [46, 77, 107–112].

Figure 2.9 is a typical block diagram of the RPFR according to [109]. The relay constantly monitors the direction of power flow by taking current and voltage input from the CT and PT. A reversal in the direction of flow of power causes the relay to send a trip signal to the RPFR breaker to disconnect the grid-tied PV system. The MIR and RPFR have a vital role to play in mitigating the effects of reverse power flow and possible voltage instability issues.

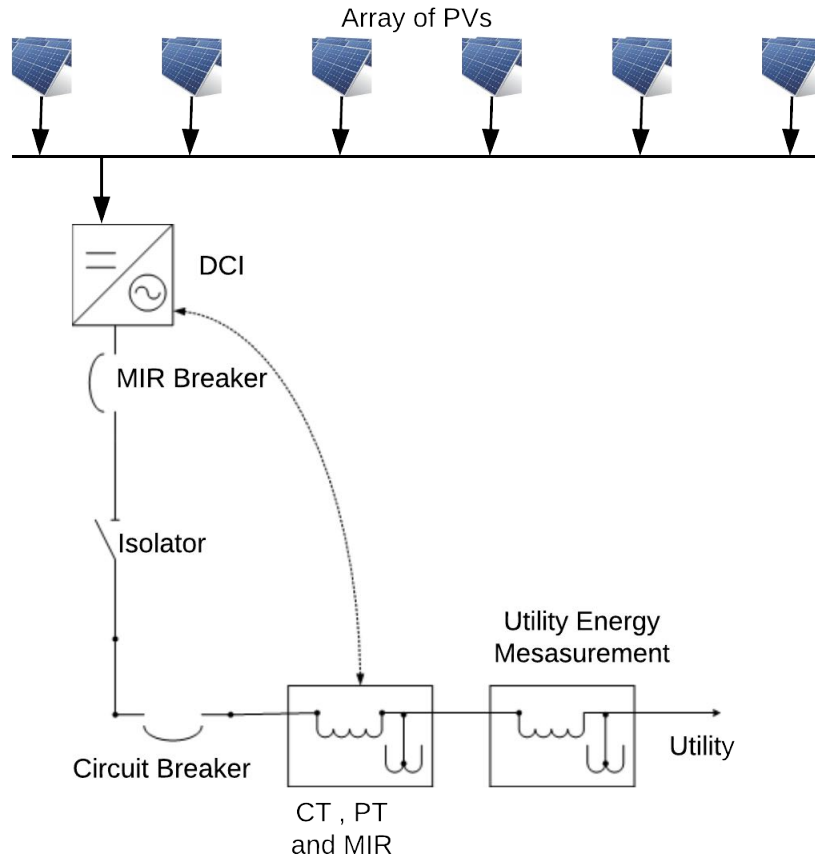


Figure 2.8: Integration of an MIR

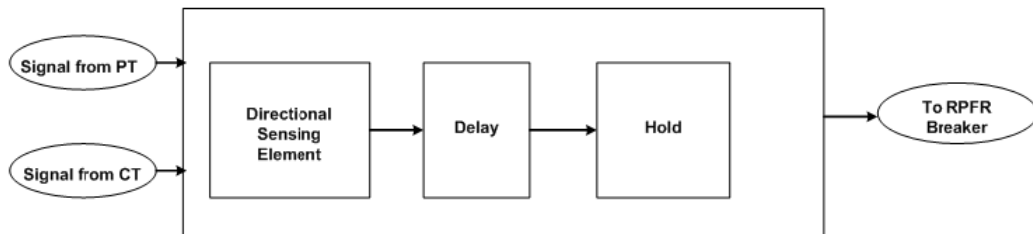


Figure 2.9: Basic block diagram of an RPF

### 2.3.2 DCI and Smart Inverter Functionalities

The DCI are inverters that can dynamically control its output power by ramping up or down based on the loading condition on the feeder the grid-tied inverter is connected to [46, 107]. The loading on the feeder is constantly monitored and a control signal can be sent to the inverter to cut down or ramp up its power output based on the load profile on the feeder. This type of inverters can help mitigate against reverse power complementing the use of MIR and RPF. Also, smart

inverters will have a vital role to play in the future smart smart grid. The IEEE 1547a as amended in 2014, allowed the use of smart inverters for voltage regulation on the feeders. The recent IEEE 1547-2018 [113] describes the various standards for inverter-based DER integration with the grid. With high PV penetrations, these functionalities of smart inverters can help mitigate many of the challenges associated with increasing PV (both utility scale and rooftops) penetration in the smart grid. New smart inverter functionalities (as presented in Table 2.2) such as dynamic load control, dynamic harmonic control, frequency deviation support, output scheduling and future functionalities would be required to help support the smart grid [114–117]. More responsibilities for the grid would lie on the smart inverters. More functionalities would also be required for future smart inverters. The major concern for power utility companies is usually the smart inverter setting that should be used for the several rooftop grid-tied PV systems. Most inverters at this scale are usually set at a power factor of unity to allow for maximum active power injection for maximum revenue to the small scale prosumers. New regulations for rooftop PV smart inverter settings will be needed as the number of grid tied rooftop PV continues to rise. With a well developed framework for smart inverters functionalities with high PV penetration, the use of legacy devices such as capacitor banks, On/Off load tap changers (OLTCs) and voltage regulators might become unnecessary for voltage optimization and control.

### **2.3.3 Dynamic and Composite Energy Storage Systems**

Several articles have been published on how the use of energy storage systems can help to mitigate the impacts of the variability in the output renewable energy sources such as the PV systems. Dynamic energy storage is an energy storage that has some prediction, forecast, dynamic scheduling and control capabilities [118]. This type of storage system will enable an efficient power curtailment,

Table 2.2: Smart Inverter Functionalities.

<b>Functionalities</b>	<b>Sub-Functionalities</b>	<b>Specific Settings</b>
Voltage Ride Through (VRT)	Low/High VRT	Voltage, Duration (time)
Frequency Ride-Through (FRT)	Low/High FRT	Frequency, Duration (time)
Dynamic Volt-VAR/Watt Control Ramping	Volt-VAR, Volt-Watt	Volt-VAR/Watt Curves Ramp rates
Power Factor setting/control		Values
Soft start	Ramp rate, Time delay	
Limit Real and Reactive Power	Enable/Disable	
Frequency-Watt		Frequency-Watt Curve
Dynamic Current Support		
Output Scheduling		Time of start, Time to end, Real and Reactive power value, operational schedule
Frequency Deviation Support		
Control of Reactive Power Dynamically.		
Dynamic Load Control		
Dynamic Harmonic Control		

reliable power smoothing and drastic reduction in the uncertainties associated with renewable energy generation. Composite or hybrid energy storage systems that uses both battery and capacitors (such as ultra and supercapacitors) have been proven to help mitigate both the fast ramps and slow ramps for grid-tied PV systems. The fast response time of capacitors when properly controlled could be used to mitigate the effects of fast ramp rates caused by fast moving clouds with PV generation [119, 120]. Figure 2.10 shows how a typical DCESS architecture can be integrated with the smart grid.



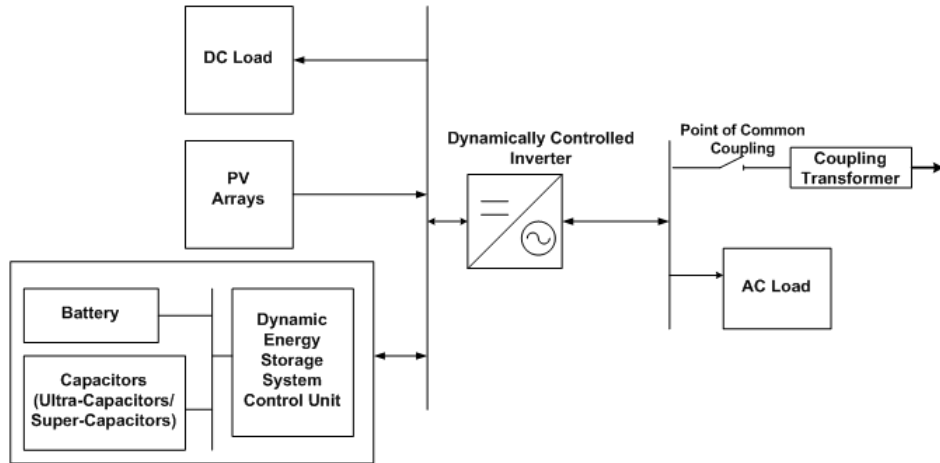


Figure 2.10: Block diagram of the integration of DCESS.

### 2.3.4 Solid State Transformers

The use of solid-state transformers would be highly beneficial to the future smart grid. This is due to its capability of interfacing as an AC and/or DC grid system and ease of dynamic control [121]. Consequently, these capabilities would allow ease of integration of distributed energy resources (DERs), such as EVs, high penetration PVs, energy storage, etc. The SSTs have the capability to improve power quality, protection and communication [122, 123]. Figure 2.11 shows a conceptual design of a typical solid state transformer with a three-phase high voltage AC input and one-phase AC voltage output . A typical SST has an AC-DC converter at its input, a DC-DC converter with a high frequency transformer (typical 10–20 kHz) and DC-AC converter at its output.

According to Wensong Yu et al. [124], SST could provide the benefits to the future smart grid within the following context.

1. Management of fault scenarios
  - Limiting of currents especially during fault scenarios
  - The ease of connecting and disconnecting of circuits attached to it
2. Power Management

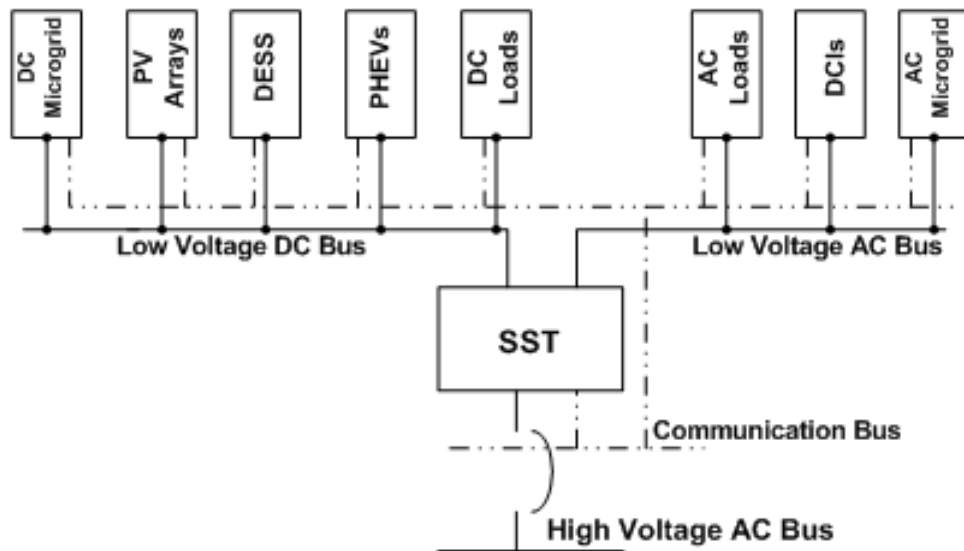


Figure 2.11: A conceptual design of a solid state transformer

- Ease and possibility of controlling the power flow in the system and the distribution feeder's power factor
- The ease and flexibility of changing and controlling the customer's and/or the feeder's voltage.
- It can provide DC power when needed
- SSTs can be used to mitigate system harmonic which is one of the drawbacks of inverter-based DERs
- The capacity of ride through during abnormal situations
- It can provide support for the DERs when on the islanding mode

### 3. Energy Management Support

- Capability to for real time energy storage monitoring
- Capability for power control and dispatch
- SST can be integrated into the mix of demand side management

The present challenges with SST applications include lower efficiency compared to the electromagnetic induction based transformers, complexities is in protection,

balancing of voltage and currents, communication and control, and insulation for high voltage levels [125]. Active research is ongoing to address these issues especially in application into the smart grid architecture.

### **2.3.5 Optimal Energy Routing**

With the integration of several prosumers and DERs (also in a microgrids) in the mix of power generation, the routing of these generated power to meet the load demand in the most efficient way becomes a big challenge . Several optimal energy routing algorithms and power electronic topologies have been proposed and developed over the years. On the optimal routing algorithm development, amongst other authors, Hong et al. proposed the use of game theory based energy routing algorithms [126], while Kado et al. formulated the use of cost-scaling-push-relabel approach [127]. Additionally, several topologies of power routers have been developed over the years. Kado et al. developed a multi-port routers for AC or DC power transfer [128], Hayashi et al. developed a digital grid router with bi-directional energy flow capabilities [129], an energy router that has the capability of intelligently managing energy flow between microgrids [130] was developed by Liu et al., and the use of smart AC/AC conversion systems [131] was developed by Kordonis et al. The basic functional requirement of a very good energy routing architecture is an efficient power electronic converter design, low latency in information exchange, highly reliable communication medium, high level of information and data security, and intelligent grid connectivity [132–136]. The development of an optimal and efficient energy routing algorithm would ensure an efficient energy transfer from the generating units to the load points. These would minimize the feeder losses and also improve the stability of the grid with a high penetration of PVs.

### **2.3.6 Distribution Supervisory Control and Data Acquisition (D-SCADA) with Advanced Distribution Management System (ADMS).**

The ADMS is a software architecture that allows automated management of the grid infrastructure by optimizing the distribution system, providing an outage restoration procedure that is automated. It also has an important feature called Fault Location, Isolation and Service Restoration (FLISR), which automatically locates a fault, isolate the faulty section (using automated switches) and restore services to the non-faulted part of the network. With high PV penetration, installation of more rooftop PVs, electric vehicles, integration of micro and nano grids, and other distributed energy resources (DERs), the ADMS will allow for smooth integration and efficient management of these sources. It will also be used as the base for implementing conservative voltage reduction and VVWO in the grid. Figure 2.12 shows an ADMS architecture with its features according to reference [137]. This architecture features integration of several enterprising softwares through the enterprise bus. The ADMS features, such as short term load forecasting (SLTF), distribution planning, and distribution energy resources management systems (DERMS), would allow for ease of dynamically control of the grid and improvement of the grid reliability and resiliency. The integration of this architecture at the utility substations will definitely mitigate many of the challenges associated with increasing PV penetration and other DERs [138–140]. From a utility company’s experiences [138], the major challenges with smooth integration of this architecture with the existing grid systems include interoperability of these enterprising softwares from the different vendors providing them, modeling of the existing infrastructure on the softwares, validation of the solutions provided by these architectures as an optimal one and many other unique challenges.

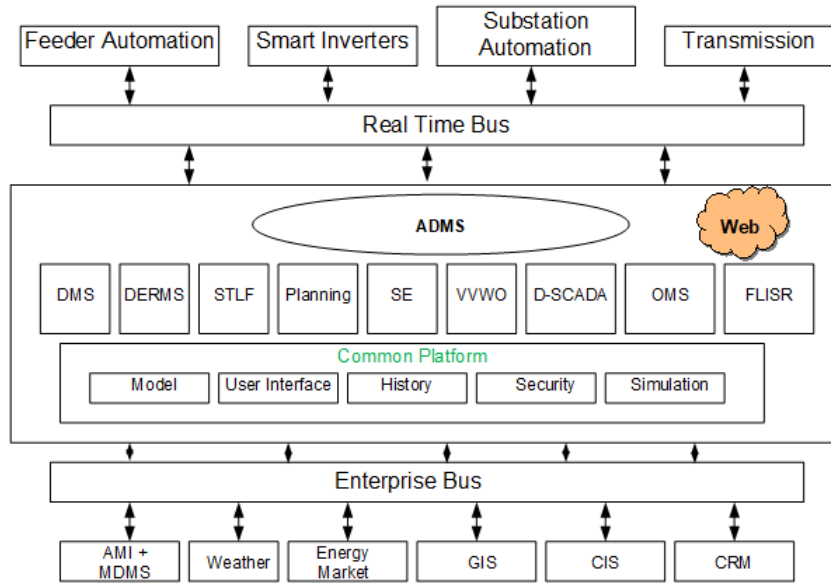


Figure 2.12: ADMS architecture and its typical features.

### 2.3.7 Advanced Relay Communication and Protection Coordination (ARCPC)

The reliability and the resilience of a smart grid architecture is dependent on the effectiveness of its protection systems. Many authors have proposed several adaptive and intelligent protection systems that use IEDs [141–147]. The IEDs, such as digital protective relays (DPR), have the capability to sense voltage, current and frequency, issue control commands, and process and communicate data. The adaptive protection scheme should be capable of some self-awareness, self-reconfiguration and self-healing. More recently, the idea of using a multi-agent system based protection system for the smart grid was proposed [148–151]. An agent is usually referred to as any hardware or software that is capable of intelligent and autonomous operation based on its intended design objectives [152, 153]. This multi-agent architecture can be easily deployed for optimal protection coordination. The protection architecture agents can be broken into the relay agent, the DER agent and the equipment agent. These agents would be linked together with a communication infrastructure [148–151, 154, 155]. Overall, more adaptive

and intelligent techniques of protection coordination need to be developed to cope with the future dynamic nature of the smart grid with increased PV penetration.

### **2.3.8 Geographic Smoothing and Optimal Location of PV Systems**

Fleet management with optimal sizing and siting of PV systems would help mitigate against some challenges as a consequence of the intermittent nature of PV [156–162]. Several factors such as feeder losses, voltage profile, cost, line ampacity and the existence of previous PV installations are some of the primary factors to be considered when siting and sizing a PV on an existing feeder. Depending on the correlation in the Global Horizontal Irradiance (GHI) of different locations, aggregating PV systems could potentially reduce the variability (and ramp rates) in the output of the aggregated PV systems. For sites that have very small correlation values, the aggregation of PV in these areas could lead to a large reduction in variability of the aggregated PV compared to each of the PV site. Aggregating PV sites with very strong correlation in GHI will produce less reduction in variability in the aggregated PV site. This is often referred to as geographical smoothing of PV power output. This is mostly applicable to utility scale PV systems. Several case studies have shown the effects and benefits of PV aggregation [163–167].

The optimal location of PV systems along a feeder with the objective of minimizing losses, reducing the possibility of reverse power flow, and preventing over-voltage could be of immense benefit with higher levels of PV penetration.

### **2.3.9 Optimal Dispatch of Renewable Energy Sources**

Being the two fastest growing sources of power generation from renewable energy sources, several studies have shown the benefits (the complimentary nature of solar irradiance and wind speed ) of hybrid generation from a mix of renewable energy

sources such as wind and PV systems . Other distributed energy resources (DERs), such as battery energy storage and most recently tidal , have been proposed as part of a composite hybrid system to address the challenges of power generation from PV systems alone. Several techniques and algorithms have been proposed to determine the optimal mix and capacity dispatch using a hybrid of these renewable energy resources. For optimal sizing of a hybrid of Wind+PV+battery, Akram et al. and Singh et al. proposed the use of iterative search algorithms and particle swarm optimization, respectively. Authors of also proposed the use of the crow search algorithm (CSA) for optimal sizing of PV+Wind+Tidal+Battery with its economic analysis. Figure shows a block diagram with the integration of wind systems and other DERs with the PV system. Each of these DERs would have its own control mechanisms for optimal dispatch of its generation. From the dispatch, scheduling and economic point of view, necessary algorithms can be developed to determine what amount (forecasting) of these sources would be available at a given point in time as well as the price signals (economics) to be used to determine the optimal dispatch of these hybrid sources.

### **2.3.10 Demand Response Management**

To ensure grid (nano-grids, micro or the macro smart grid) stability, which could be threatened with high PV penetration, power generation must be able to meet the load demand plus the losses associated with transferring the power from the point of generation to the load. Conventionally, the generated power is usually controlled to meet the load demand at all times. The use of demand response management (DRM) techniques allow for a dynamic control (such as load shedding/curtailing, load shifting) of the load to match the energy generation in real time. The benefits of DRM include a reduction in power generation and costs to meet the load demand, reduction in variation of prices , increased reliability of

the system , improved management of system congestion and improvement of the overall system security . The use of DRM algorithms provide an excellent way of overcoming the variable nature of power generation from PV systems by dynamically controlling the load to match the power generation. Some of the proposed algorithms for DRM include:

- The use of large time constant loads to create a virtual energy storage which is used to smoothen the intermittent output of PVs through DRMs .
- An IoT-based, real time smart-direct load control (S-DLC) was proposed by . The algorithm creates a schedule for the customer loads, then controls and optimize the loads (which already has an intelligent electronic devices (IED) embedded) through a load shedding and forecasting algorithm.
- Karapetyan et al. proposed an event-based DRM using the greedy approach for customer load curtailment. An integer programming problem was formulated which estimated the amount of loads to be curtailed while using the maximum available generated power .
- Sivaneasan et al. proposed a DRM algorithm that controls the air-conditioning and ventilation systems in a building. Whenever there is a drop in PV power generation, the developed systems adjust the air conditioning system by putting into consideration the well-being of the occupants of the building. This system incorporates a battery storage management system and a load shedding algorithms that is based on the level of priority of the loads

The use of state-of-the-art DRM algorithms would be a vital tool in addressing the intermittent nature of power generation from photovoltaic systems.

### **2.3.11 Big Data Solutions**

The characteristics (volume, heterogeneity, speed and veracity) of the data involved in operating a smart grid with high PV penetration constitutes a big data



challenge . Solutions to big data challenges needs a data storages with high capacity and very high processing speed. Some of the available solutions that can be leveraged on to solve the big data challenges are highlighted below.

### **Data Processing Frameworks**

As mentioned earlier, the data volume necessitates the use of some big data processing framework. Examples of existing data processing frameworks that can be used include: Flink, Spark, Storm, and Hadoop .

### **Cloud Computing Frameworks**

The use of cloud computing in big data allows utility companies to achieve some level of flexibility and efficiency in managing the their data. Some available cloud service models that can be leveraged in a smart grid with high level of PV penetration include:

- Software as a Service (SaaS)
- Infrastructure as a Service (IaaS)
- Platform as a Service (PaaS)
- Data as a Service (DaaS)
- Communication as a service (CaaS)
- Monitoring as a Service (MaaS)

### **Post-Cloud Computing Networks**

To address the central architecture-based cloud computing frameworks (which is usually plagued by congestion, latency and reduced Quality of Service (Qos)), several other post-cloud computing paradigms have been proposed . These include, Fog Computing , Mobile Edge Computing (MEC), and Dew Computing . These new post-cloud computing paradigms ensure improved security, reduction in

bandwidth, better scalability, improved visibility and decreased latency . These computing paradigms can be leveraged on to address the computing challenges that will arise with increased penetration of PVs in the smart grid.

Other solutions that have been proposed to solve the challenges that emanates from big data include the use of game theory , and machine learning algorithms, such as deep learning , selective encryption , and defense-in-depth (DiD) .

### **2.3.12 The Use of Artificial Intelligence**

The deployment of artificial intelligence (AI) could help to better integrate new PV and the existing ones with the grid. AI has the ability to use machine learning algorithms to analyze new and historical data, carry out some predictions and forecasting, execute some control operations and make some intelligent decisions. The use of AI can be deployed in weather forecasting (which includes irradiance, temperature, wind speed and cloud speed), determining the optimal size of PV systems, smart inverter controls, tracking of PV's maximum power point, system optimization and control, accurate estimation and identification of solar cell parameters and models, and diagnosing faults in PV systems . AI uses machine learning algorithms, which is usually classified into Supervised and Unsupervised learning. Examples of supervised learning techniques includes

- Random Forest
- Deep Learning
- Generalized Linear Models (GLM)
- Decision Trees
- Gradient Boosting Machine (GBM)

Unsupervised learning techniques include:

- Principal Components Analysis (or Dimension Reduction)

- Anomaly Detection
- Clustering

According to [1], AI algorithms that have been applied to PV systems include: Neural Networks (NN), Fuzzy logic (FL), Simulated Annealing (SA), Genetic Algorithm (GA), Ant colony (ACO), Particle Swarm Optimization (PSO), Adaptive-Neuron Fuzzy Inference Systems (ANFIS), GA-fuzzy, and NN-fuzzy. There is an obvious need for a proactive approach towards developing more advanced and smart protection systems and integrated technology that allows ease of DER penetration and control for improved reliability and resilience of the grid.

## **2.4 Summary of Present and Future Challenges with Suggested Combinatorial Solutions and Future Direction**

With the present PV penetration level, many challenges with PV penetration are incipient as mentioned earlier. With the drive toward achieving a higher levels of PV penetration, many of these challenges with the future scenarios earlier mentioned would become more aggravated. Table 2.3-2.5 highlight these problems and the combination of solutions that could address these challenges based on the solutions highlighted in Section 2.3.

Table 2.3: PV penetration problems and suggested future solutions.

Challenges	Existing (with Present Penetration Levels)	Future (with Smart Cities, PHEVs, Solar Eclipse, Transactive Energy, Big Data, Cybersecurity etc.)	Suggested Future Solutions
Reverse Power flow	incipient problem depending on the point of interconnection with the feeder.	Increase expected. Reduced the choice of point of interconnection.	Minimum load ensured on feeders. MIR, RPF. $SI_{LC}$ .SI+D-SCADA,AMI
Voltage instability issues	OLTC and DVRs has been effective.	Increase expected.	STs. DCESS,OLTC. STATCOMs. DVRs, SI+D-SCADA with FRT. GS with PV fleet management.
Complexity in protection coordination	No major issues with Coordination in relays, sectionalizers, fuses, reclosers.	Increased bidirectional flow of current and fault current levels, line to ground voltage increase due to more single phase prosumers, possible desensitization the substation relays, unwanted blowing of fuses, maloperation of reclosers and sectionalizers.	Advance short circuit analysis with high PV penetration. SI with fault current monitoring and control capabilities. ARPC
Power factor problems	No major concerns.	Increase expected.	Use of SI with dynamic reactive power control for both utilities and prosumers. SI+D-SCADA, OER.
Harmonics	No major concerns.	Increase expected.	All SI compliance with UL 1741. SI+DLHC capabilities. Use of STATCOMs
Frequency Instability	No major concerns. Germany's '50.2 Hz' problem .	Increase expected.	GS with PV aggregation for utility-scale PV systems.DESS. SI+FRT, OER

Table 2.4: PV penetration problems and suggested future solutions.

<b>Challenges</b>	<b>Existing (with Present Penetration Levels)</b>	<b>Future (with Smart Cities, PHEVs, Solar Eclipse, Transactive Energy, Big Data, Cybersecurity etc.)</b>	<b>Suggested Future Solutions</b>
Feeder losses	Slight increase depending on POI	Possible future increase.	Robust optimal PV placement algorithms, OER on the distribution feeders.
Thermal limits of the grid	No significant effects	Increase expected.	UL 1741 compliance for all SI. Optimal placement of utility-scale and small scale aggregated PV system, OER
Security of supply	No major issue.	Threatened.	Accurate estimation methods of prediction (of security of supply) should include future market analysis consideration of the intermittent nature of PV system as well as the development of other dispatchable energy sources.
Communication within Distributed Energy Resources (DER) and substation, Cybersecurity	No communication and control link. IEEE 2030 standard has not been fully developed.	Reliable and well defined communication and control protocols needed. Interoperability of DERs in a TE environment.	IEDs .Robust IEEE 2030 standards and adoption by all PV systems. Fast computing and communication architecture.
Dynamic modeling of the high penetration PV	GIS-based Distribution Management Systems (DMS) models PV systems as a negative load.	System modeling with PHEVs, and proliferation of prosumers would be required. Energy routing modeling for IoT enabled TE would be required. More detailed studies solar eclipse impacts would be needed.	Dynamic models PV systems should be developed for GIS-based DMS and GIS-based Energy Management Systems (EMS) for remote monitoring and control.

Table 2.5: PV penetration problems and suggested future solutions.

<b>Challenges</b>	<b>Existing (with Present Penetration Levels)</b>	<b>Future (with Smart Cities, PHEVs, Solar Eclipse, Transactive Energy, Big Data, Cybersecurity etc.)</b>	<b>Suggested Future Solutions</b>
Forecasting	Forecasting always have some level of uncertainty. The level of accuracy is still low	Accuracy will be key to adequate planning, unit commitment and dispatch.	Hybrid-forecasting (nowcast-forecasting+forecasting). More accurate prediction models using multiple forecasting methods.
Dispatch and Scheduling problem	No major issues reported	Increase on PV penetration in transactive environment will require the implementation of optimal power flow and optimal dispatch with high PV penetration mandatory	Optimal Smart Inverter Dispatch (OSID). Optimal set point for storage systems. Mitigation techniques for forecast and communication errors in (OSID)

## 2.5 Summary

This chapter presented the various challenges with PV penetrated network and classified them based on their areas of impact. With the inevitable future increase in PV penetration, this chapter also took an extensive look at different future scenarios and their impacts with higher levels PV penetration in the network. The present technical solutions with the existing penetration was also presented. Many of these existing solutions need further development with some future research direction indicated in this chapter. This review showed that the technical, operational and environmental challenges with PV integrated network are still incipient and would become more prominent with increased level of penetration, especially within the context of the future scenarios earlier discussed. The dy-

namics of the smart grid is expected to change with these future scenarios. More advanced and adaptive techniques have to be developed to mitigate the challenges that would arise in these scenarios

CHAPTER 3  
AGGREGATION OF PHOTOVOLTAIC SYSTEMS FOR  
INTERMITTENCY REDUCTION

### 3.1 Introduction

This chapter presents an overview of various studies that has been done on analysing and quantifying the variability of aggregated PVs and also presents a case study based on real data from four existing PV sites in Florida using three proposed techniques for improved analysis of aggregated PV variability. The ramps in the PV systems power output have always been the major challenge with increasing level of PV penetration [163]. Several works have been historically reported on the effect on geographic smoothing by PV aggregation. Jewell and Kern [166] calculated the reduction in variability of aggregated PV sites due to wide geographical differences by developing cloud models. References [164, 165] considered a very wide geographic area while [166] considered a much smaller geographical area.

A study of PV sites covering an area approximately  $450,000 \text{ km}^2$  ( $600\text{km} \times 750\text{km}$ ) in Germany by [167] showed a significant reduction in variation in PV power output. A 5-min variation from a single PV power output at a given site from the study was seen to exceed  $\pm 50\%$ . When the output power from 100 PV sites spread across the country were aggregated, the variation in the aggregated PV power output was seen not to exceed  $\pm 5\%$ . A study in Arizona by Curtright [168] showed that there could be as much as a 60% change in PV capacity with a 10-min step from a single PV site. An aggregation of three PV sites in the study [168] showed a reduction in the ramp in the output of the aggregated PV sites. Otani [169] showed the reduction in ramp rates of irradiance can be reduced due to geographical diversity by considering a 4km by 4 km area.

The work done in [170] was similar to [169]. They, in [170] used a  $4\text{km} \times 4\text{km}$  area with a network of sensors for irradiance in the area. Their findings showed



that geographic smoothing was more effective when the variability in irradiance is very steep. This usually occurs during the partly cloudy days.

A method for calculating the variability of aggregated plants over a wide area was developed by authors of [14] and validated. Their validation showed that the variability of these aggregated PV plants strongly depends on the correlation in the variability of each individual plants in the study. Their studies [14] also showed that the correlation of individual plant depends on the time scale used as well as the separation between individual plants. From their studies, plants that are widely separated in distance have a lower value of correlation coefficient and also with a shorter time scales, their correlation is reduced. Their studies further showed that there is no correlation in 1-min and 5-min variations irrespective of the distance between the PV sites.

A simplified model to estimate the variability of aggregated fleet of PV plants relative to the variability of each plant in was developed by Hoff and Perez [15]. They defined a parameter they called dispersion factor which is dependent on the way the PV systems are laid out, the time scale used for the analysis and the movement of the cloud over the entire PV fleet. Their results showed that the relative variability in output as defined earlier, reduced in a quasi-exponentially with the PV fleet dispersion factor. They [15] made some important conclusions that the relative fluctuation in the output of the aggregated PV site reduces with increase in distance between the individual PV sites, the reduction in variability with increase in distance is weakened when the time interval considered is increased, the reduction in variability also weakens when the speed of the movement of the cloud across the PV fleet increases. They also showed that the output variability of PV fleet in uncorrelated locations is equal to the variability of a single location multiplied by the inverse of the square root the number ( $M$ ) of various locations of the individual PV sites as expressed in 3.1.

$$\alpha_{\Delta t}^F = \frac{\alpha_{\Delta t}^1}{\sqrt{M}} \quad (3.1)$$

where  $\alpha_{\Delta t}^1$  equals the standard deviation of the variability in output of the PV system concentrated in a particular location,  $\alpha_{\Delta t}^F$  is the standard deviation of the variability of an aggregated PV sites in different locations and M is the number of locations under consideration that are not correlated.

Also the maximum variability in output of these aggregated fleet of PV sites was found to be given as equation (3)

$$\alpha_{\Delta t, max}^F = \frac{\alpha_{\Delta t}^1}{\sqrt{2M}} \quad (3.2)$$

The same authors in [15] went further in reference [171] to develop a more general variability model that takes into consideration correlated PV sites.

$$\alpha_{\Delta t}^F = \sqrt{Var \left[ \sum_{m=1}^M \Delta P_{\Delta t}^m \right]} = \sqrt{\sum_{i=1}^M \sum_{j=1}^M COV_{ar}(\Delta P_{\Delta t}^i, \Delta P_{\Delta t}^j)} \quad (3.3)$$

$$COV_{ar}(\Delta P_{\Delta t}^i, \Delta P_{\Delta t}^j) = \alpha_{\Delta t}^i \alpha_{\Delta t}^j \alpha_{\Delta t}^{i,j} \quad (3.4)$$

$$\alpha_{\Delta t}^F = \sqrt{\sum_{i=1}^M \sum_{j=1}^M \alpha_{\Delta t}^i \alpha_{\Delta t}^j \alpha_{\Delta t}^{i,j}} \quad (3.5)$$

where,  $P_{\Delta t}^i$  is the change in PV power output at location  $i$  and  $COV_{ar}$  is the covariance of different combinations of all the PV sites possible.

Lave Mathew in [16], demonstrated geographical smoothing of aggregated PV plants by analyzing the variability in the solar irradiance and the output of PV power plants. Due to the almost linear proportionality between the global horizontal irradiance (GHI) and the power output of PV systems and the dearth in availability in actual power output data of PV sites from PV proprietors, the GHI values was used for his simulation.

Lave et al [17–21] developed a variability model for analysis of the variability of the power output of PV plants (Wavelet Variability Model) using wavelet analysis as expressed in 3.6-3.8. The wavelet variability model has the following as inputs. These include, the footprint of the PV array, the density of the PV fleet (capacity

per  $m^2$ ), the time series of the measurement sensor for the irradiance measurement, a coefficient called the correlation scaling factor. The output of his proposed model gives the average irradiance of the PV fleet. The average irradiance of the fleet can therefore be used to estimate the output power of the PV plant.

$$w_{t^-}(t) = \int_{t_{start}}^{t_{end}} GHI_{norm}(t') \frac{1}{\sqrt{t}} \psi\left(\frac{t' - t}{t^-}\right) dt \quad (3.6)$$

$$\sum_{j=1}^{12} w_{t^- = 2^j}(t) = GHI_{norm}(t) \quad (3.7)$$

$$GHI_{norm}(t) = \frac{GHI(t)}{GHI_{clr}(t)} \quad (3.8)$$

where  $GHI_{norm}(t)$  is the normalized GHI,  $GHI_{clr}$  is the clear-sky model GHI  $t^-$  is the time scales of the wavelet,  $t_{start}$  and  $t_{end}$  is the beginning and the end of the GHI timeseries respectively.

His model was validated with 2.13 MW aggregated rooftop PV located in Ota city in Japan and 48 MW PV plant in Copper Mountain. The WVM was able to represent accurately the variability by time scales on these two aggregated plants. The WVM was compared to three other methods. These methods are

1. Linear scaling the irradiance measured by a sensor by multiplying it by a constant factor. This method assumes a that the variability of a single point is similar to that of a whole PV plant.
2. Finding the average of the GHI timeseries measured from the fleet of sensors placed in an equal area on the PV fleet. The accuracy of this method is dependent on the number of sensors used. The higher the number of sensors, the more accurate the prediction of the variability of the entire fleet. the sensors are also arranged to match the profile of the PV fleet for an accurate estimate of the overall variability of the PV fleet.
3. The use of moving average for the irradiation timeseries. This method can only be used for a single time scale. It cannot be used to estimate the

smoothing effect of aggregated PV plant using GHI timeseries for multiple time scales.

The results from the WVM model shows more accurate maximum ramp rate estimation for the Copper Mountain PV fleet. The advantage of the WVM is the use of lesser number of inputs by the WVM compared to other methods. These other methods require much denser network of sensors and cloud velocities for higher accuracy of the variability estimate. The WVM was used to characterized the variability of rooftop PV systems in 553 homes in Ota city Japan [172]. Several conclusions were made form the studies. These include

1. Increasing in the rooftops PV leads to a higher decrease in the maximum ramp rates.
2. The reduction in the maximum ramp rates decreased exponentially as more rooftop PVs are already installed.
3. From 1 to 500 rooftop PV systems, there is a lager decrease in maximum ramp rates with short timescales.

### **3.2 A Case Study and analysis of Four PV Sites located in Florida**

Figure 3.2 shows the locations and distances (in miles) between four PV sites located in Florida with their name-plate capacities. One of the PV fleet is located on Florida International University Engineering Center campus [51]. Figure 3.3 shows the power output of the PV sites with 1-minute resolution on June 1-10, 2017. This power output profile of these four sites shows some difference in the variability profiles of these four PV sites.

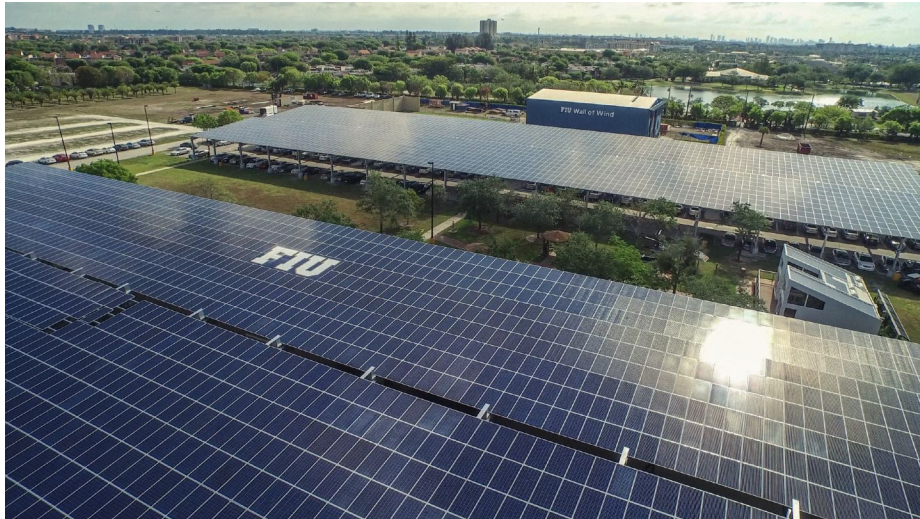


Figure 3.1: FEC 1.4 MW PV Located on FIU Engineering Campus

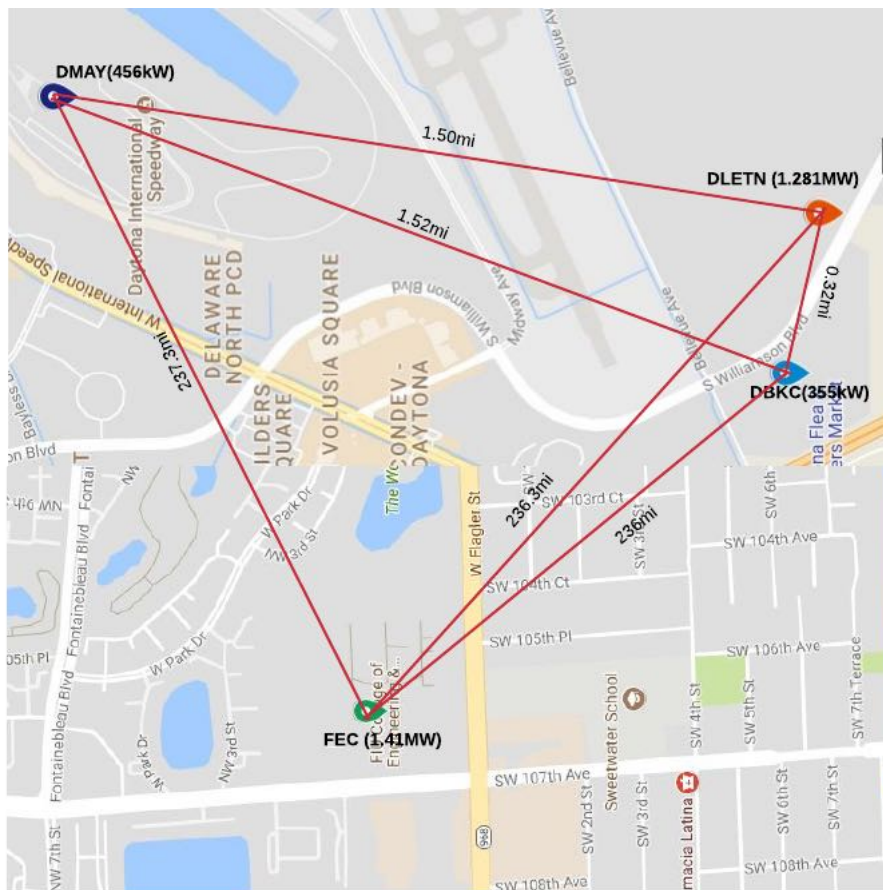


Figure 3.2: PV fleet locations on Google map

### 3.2.1 Aggregation Analysis

The use of Pearson correlation technique was adopted to calculate the correlation in the time series power output of these four sites. Obviously, the lesser (smaller) the correlation coefficient for any pair of sites, the more the effect of geographical smoothing will be expected. Also when the correlation coefficient between any two sites is -1, this means that we can expect the best of smoothing effect from the aggregation of these two sites.

Table 3.1: Pearson Correlation Coefficients between the four sites

Sites	FEC	DMAY	DLETN	DBKC
<b>FEC</b>	-	0.6225	0.7178	0.7115
<b>DMAY</b>	0.6225	-	0.7320	0.7425
<b>DLETN</b>	0.7178	0.7320	-	0.9400
<b>DBKC</b>	0.7115	0.7425	0.9400	-

The correlation coefficients as shown in table 3.1 shows a very strong correlation (0.94) in the power output of DLETN and DBKC which is expected due to the proximity (0.32 mi) between these two sites. They are actually connected to the same distribution feeder. The weakest correlation (0.6225) between pairs of these sites exists between FEC and DMAY. This can easily be explained by the long geographical distance (237.3 mi) between the two sites. There is a slight reverse characteristics in correlation between FEC-DLETN and FEC-DBKC. Despite the lesser distance between FEC-DBKC, the correlation was smaller compared to FEC-DLETN with slightly longer distance. The same applies to DMAY-DLETN (1.5 mi) and DMAY-DBKC (1.52 mi).

Also, table 3.2 shows the various ramp rate ( $|\text{RR}|$ ) for the four sites in June 2017. An new aggregate PV plant was defined as PVAGE. PVAGE is the aggregation of these four PV plant considered in this study. Its capacity is therefore estimated as 3.502 MW. Of the four individual sites (DMAY, DLETN, DBKC, and FEC), FEC had the highest maximum and mean ramp rate which is however

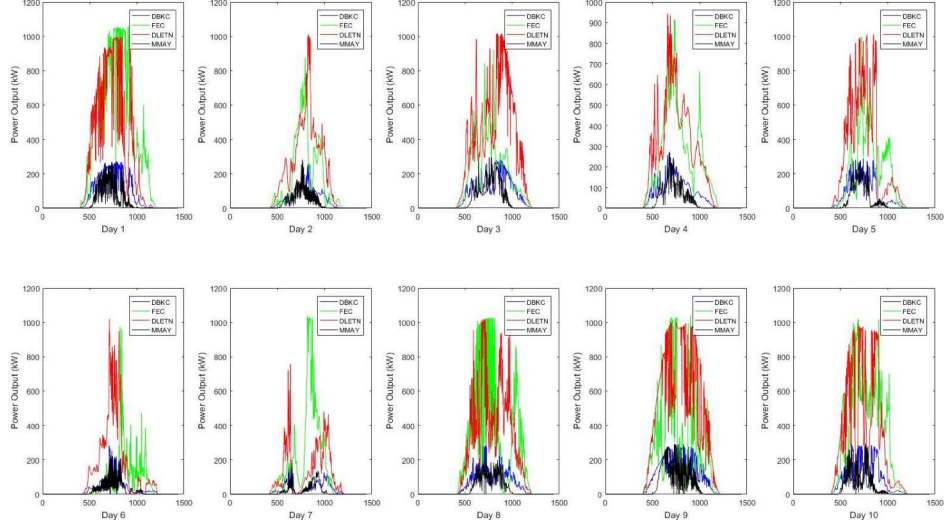


Figure 3.3: A 10-Day PV Power Output of the four PV plants

expected due to its large installed capacity. Two new parameters ( $Max_{norm}$ ) and ( $Mean_{norm}$ ) were defined as the ratio of the maximum and Mean ramp rate per unit installed capacity respectively, where  $PV_{NPC}$  is the PV name-plate capacity. This is to normalize the ramp rates for fair comparison between these four sites with different installed capacities. This also allows the effect of the reduction in ramp rate per unit installed capacity be easily observed. The ( $Max_{norm}$ ) and ( $Mean_{norm}$ ) values in table 3.1 shows that the aggregated PV sites (PVAGE) has the least normalized maximum and mean ramp rates.

$$Max(norm)(|RR|) = \frac{Max(|RR|)}{PV_{NPC}} \quad (3.9)$$

$$Mean(norm)(|RR|) = \frac{Mean(|RR|)}{PV_{NPC}} \quad (3.10)$$

Using Perez et al [173] formulated variability measurements metrics for power measurements as expressed as (3.11) and (3.12).

$$FPV = \sqrt{Var \left[ \sum_{n=1}^N \Delta P_{\Delta t}^n \right]} \quad (3.11)$$

Table 3.2: One minute ramp rate for June 2017

Site	Max ( RR ) $kWmin^{-1}$	Max (norm) ( RR ) $min^{-1}$	Mean ( RR ) $kWmin^{-1}$	Mean (norm) ( RR ) $min^{-1}$
<b>FEC</b>	829.2	0.5881	16.5134	0.0117
<b>DMAY</b>	233.9	0.5129	9.7080	0.0213
<b>DLETN</b>	800.7	0.6251	14.0541	0.0110
<b>DBKC</b>	221.2	0.6232	3.9456	0.0111
<b>PVAGE</b>	1249.5	0.3568	34.2487	0.0098

$$FRV = \frac{\sqrt{Var \left[ \sum_{n=1}^N \Delta P_{\Delta t}^n \right]}}{PV_{ANPC}} \quad (3.12)$$

Where FRV is the fleet relative variability, FPV is the fleet power variability, and  $PV_{ANPC}$  is the aggregated PV fleet name-plate capacity. The fleet relative variability is a statistical metric that allows the smoothing effect of aggregated spatial located PV systems to be easily compared.

Figures 3.4 and 3.5 show the fleet relative variabilities for the different combinations of any two PV plants. The AGRE is the aggregation of any of the two PV sites. As formulated by Perez et al, the variability of the combined fleet reduced in all the possible combination of the fleet. The largest reduction in variability was observed with the FEC and DETLN aggregation. This is due to the close size of this two PV fleets and the relatively low correlation between them due to the large distance between these sites.

The results of the aggregation of pairs of sites also shows that the aggregated variability reduced significantly compared to that of the smaller sized PV fleet. In other words, when two PV fleets with different PV capacities are aggregated, the variability of an aggregated fleet of PV systems is usually close to the variability of



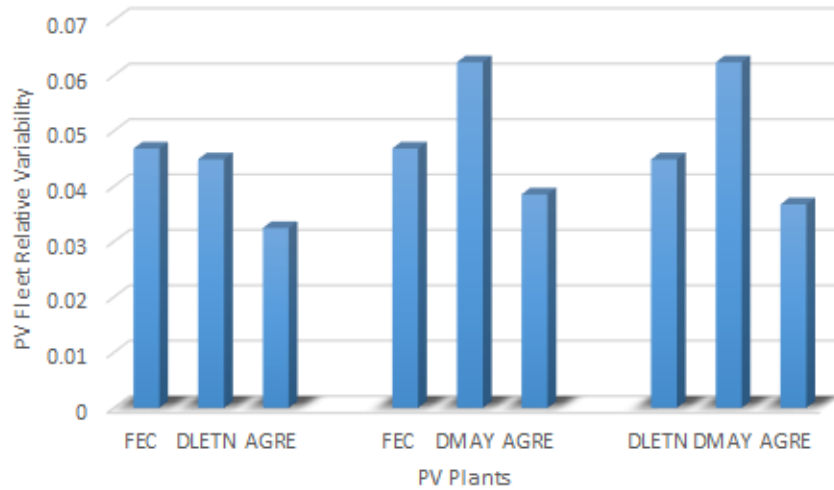


Figure 3.4: Fleet relative variability of each PV sites and aggregation.

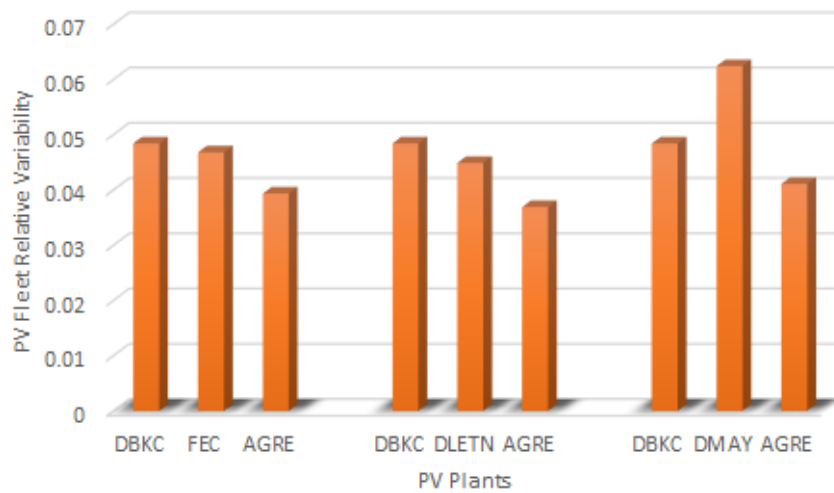


Figure 3.5: Fleet relative variability of each PV site and aggregation.

the larger PV fleet. Figure 3.6 shows the relative variabilities of the PV fleet and the aggregation of the entire four fleets. The summary of the various reduction in variability of each PV site compared to the aggregated PV system is presented in table 3.3. The table showed a significant reduction of about 40.5% from that of DELTN and 57.2% from DMAY in the variability of the PV output of the aggregated fleet of the four PV plants. The results further show that the larger the size of the aggregated PV fleet results in a higher reduction in variability of the aggregated fleet.

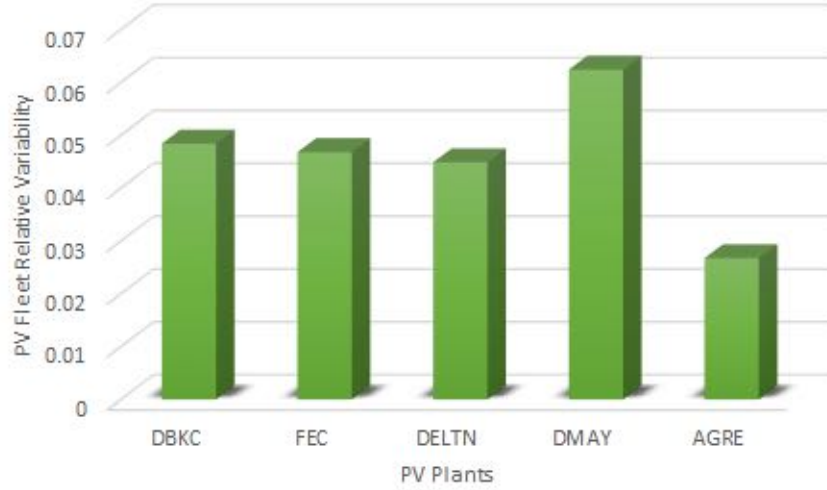


Figure 3.6: Fleet relative variability of each PV site and aggregation.

Table 3.3: % Reduction in variability of each PV fleet compared to the aggregated fleet.

Fleet	AGRE	Fleet	AGRE
DBKC	18.75	FEC	30.62
FEC	15.97	DLETN	27.64
DBKC	23.80	FEC	17.64
DLETN	17.82	DMAY	38.24
DBKC	15.12	DLETN	18.15
DMAY	34.17	DMAY	41.15

Fleet	AGRE
DBKC	44.79
FEC	42.90
DBKC	40.45
DLETN	57.19

### 3.2.2 Power Spectral Density Analysis

The power spectral densities of this four sites (DMAY, DLETN, FEC and DBKC) was plotted as shown in Figure 3.7. The actual power output in (kW) for a period of 1 month (June 2017) of the grid-tie inverters was used to plot the PSDs for these four PV fleets. Figure 3.8 is the PSD plot of the aggregation of the four sites. The PSD allows ease of visualizing the variability in the power output of the plants at different frequencies. A large PSD indicates a large variation in the power output of the plants. Each of the PSD shows a peak power output at a cycle of 24 hours another peak at 12 hours. This corresponds to a frequency of  $4.16 \times 10^{-2} Hz$  and  $8.3 \times 10^{-2} Hz$  respectively on the PSD plots. The PSD of the aggregated PV (figure 3.8) shows a steeper slope compared to the individuals

PSDs. This is an indication of a reduction in aggregated variability [16].

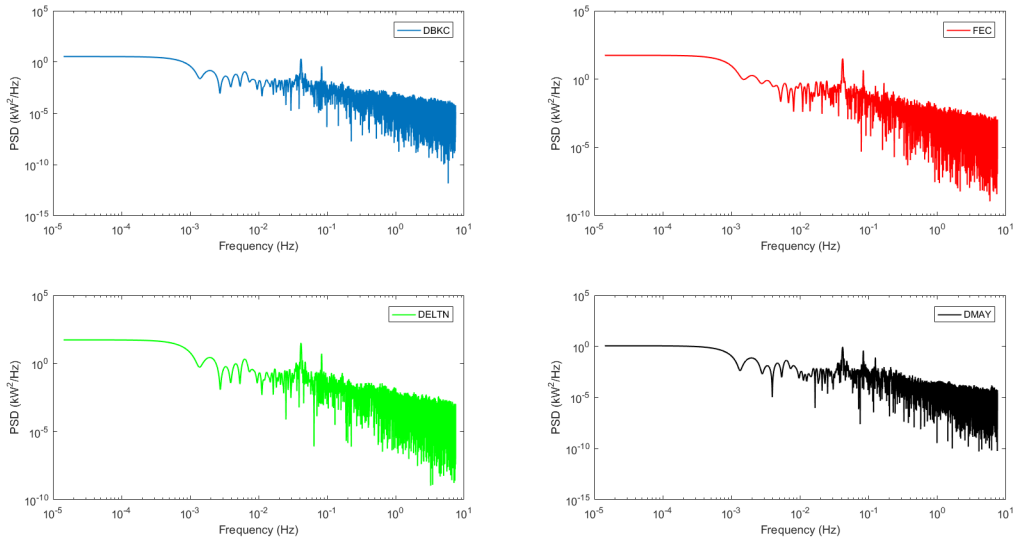


Figure 3.7: PSD Plots for the four PV Fleet.

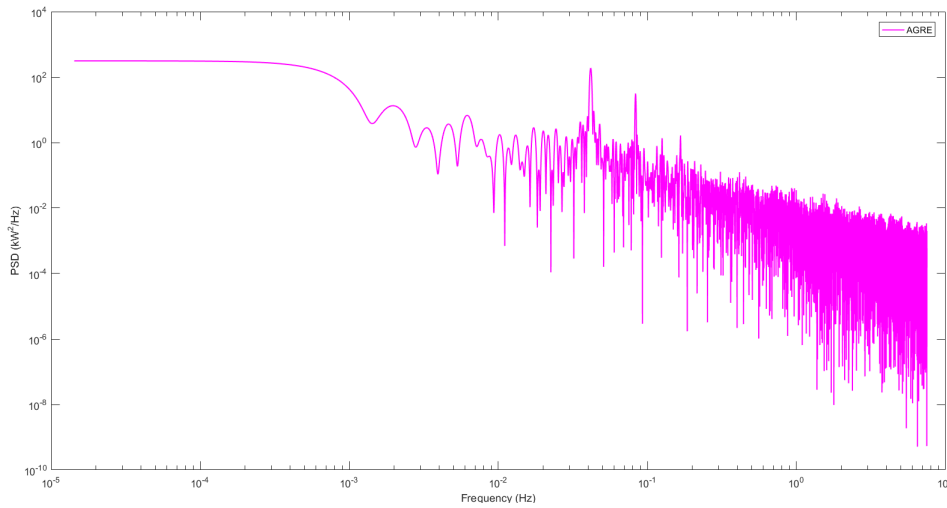


Figure 3.8: PSD for the aggregated fleet.

### 3.2.3 Discrete Wavelet Application

The choice of wavelets is typically based on the area of application. As a rule of thumb, a wavelet that is similar to the shape of the original signal is usually selected. A wavelet was designed using the polynomial approximation method with the a polynomial of degree three. A standard discrete approximation of Meyer

wavelet is used for this analysis due to its similarity to the designed wavelet, (as shown in figure 3.9) as well as the original PV power generation. In the frequency domain, the mayer wavelets  $\Lambda(t)$  and scaling function  $\lambda(t)$  is expressed as 3.13-3.15

$$\Lambda_{meyer}(w) = \begin{cases} \frac{1}{\sqrt{2\pi}} & \text{for } w \leq \frac{2\pi}{3} \\ \frac{1}{\sqrt{2\pi}} \cos(\frac{\pi}{2} f(\frac{3w}{2\pi} - 1)) & \text{for } \frac{2\pi}{3} \leq w \leq \frac{4\pi}{3} \\ 0 & \text{otherwise} \end{cases} \quad (3.13)$$

$$f(a) = \begin{cases} 0 & \text{for } a < 0 \\ a & \text{for } 0 \leq a \leq 1 \\ 1 & \text{for } a > 1 \end{cases} \quad (3.14)$$

$$\lambda_{meyer}(w) = \begin{cases} \frac{1}{\sqrt{2\pi}} \sin(\frac{\pi}{2} f(\frac{3|w|}{2\pi} - 1)) \exp \frac{jw}{2} & \text{for } \frac{2\pi}{3} \leq w \leq \frac{4\pi}{3} \\ \frac{1}{\sqrt{2\pi}} \sin(\frac{\pi}{2} f(\frac{3|w|}{4\pi} - 1)) \exp \frac{jw}{2} & \text{for } \frac{4\pi}{3} \leq w \leq \frac{8\pi}{3} \\ 0 & \text{otherwise} \end{cases} \quad (3.15)$$

The normalized PV power generation  $P_{gnorm}(t)$  can be decomposed into its approximation and its detailed coefficient using in (3.16) and (3.17) .

$$P_{gnorm}(t) = \frac{P_g(t)}{P_{\text{name plate capacity}}} \quad (3.16)$$

$$P_{gnorm}(t) = A_{\infty} \lambda(t) + \sum_{j=0}^{n-1} \sum_{k=0}^{n-1} A_{j,k} \Lambda_{j,k}(t) \quad (3.17)$$

Where  $A_{j,k}$  are the wavelet coefficients.

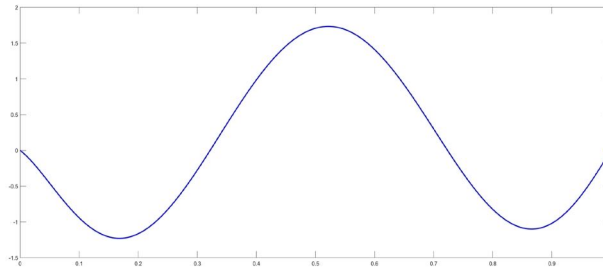


Figure 3.9: Wavelet design based on a single day PV generation

A level 2 Meyer wavelet decomposition was done on the individual fleet, aggregated pairs of PV output and the aggregation of the entire four PV fleet. Top level details (Coefficients 1) captures the high frequency components of the signal while lower level details (Coefficients 2) capture the lower frequencies of the signal. From the decomposed plot of the aggregated PV, it can be seen that, the various aggregation depending on their sizes and correlation coefficient produces different reduction in aggregated variability. Analyzing the high frequency components of the individual PV and the aggregated ones, the results show that for each of the pairs of aggregated PV, there is a reduction in variability based on the amplitude of the high frequency coefficient (coefficients 1). The coefficients of the aggregation of the entire fleet show more reduction in variability based on the amplitude of the high frequency coefficients. For easy visualisation of the relative reduction in the variability of the aggregated sites, a plot of the variance of coefficients 1 and 2 are also plotted as shown in 3.10a - 3.11b.

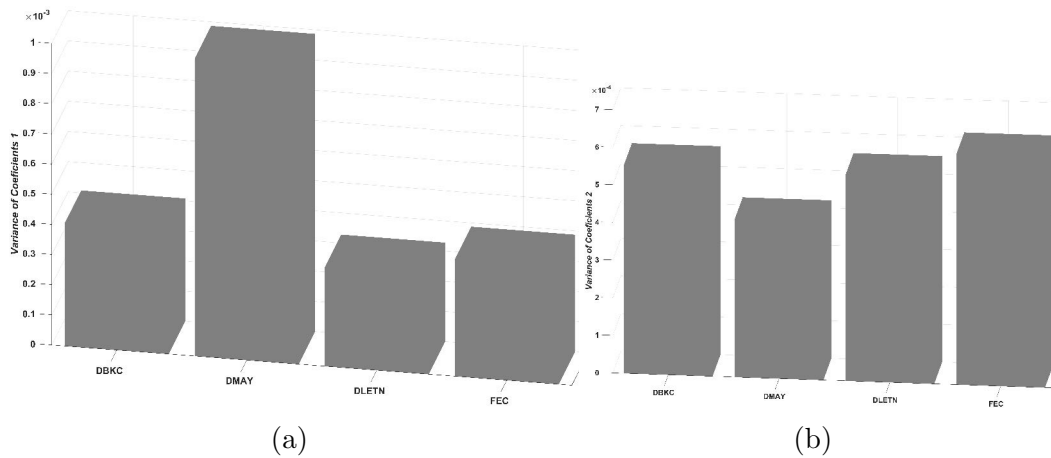


Figure 3.10: Variance estimation of the details discrete wavelet coefficients (a) Coefficients 1 of individual PV sites (b) Coefficients 2 of individual PV sites

Before aggregation, sites DMAY had the highest variance in high frequency components with DLETN having the least. The aggregation results showed that the aggregation of FEC and DLETN produced the most reduction in variability. This can be explained by the closeness in sizes of these two PV fleet. The results

also showed that the aggregation of PV with wide difference in their name plate capacities will produce a variability which is similar to that of the larger PV system. Also, sites with smaller correlation in their GHI profile (or output power) will produce more reduction in variability. The aggregation of the entire four PV fleets PV produced the most reduction in variability. This can be seen from figures 3.11a and 3.11b.

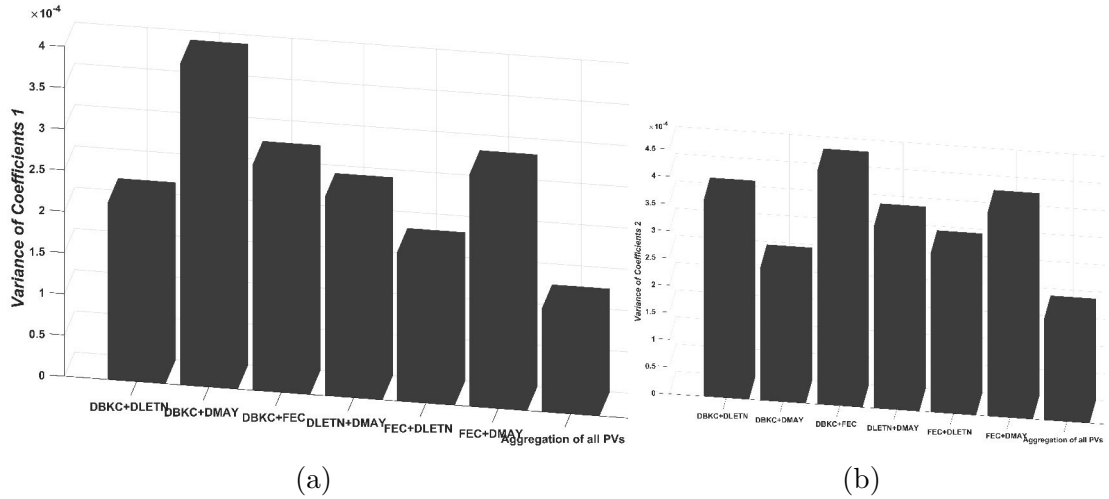


Figure 3.11: Variance estimation of the details discrete wavelet coefficients (a) Coefficients 1 of aggregated PV sites (b) Coefficients 2 of aggregated PV sites

### 3.3 Summary

A comprehensive review of different methods and techniques of PV aggregation highlighting their various strength and weaknesses has been presented in this chapter. By using some real data from the power generation of four PV sites in Florida, an analysis of the various impacts of PV aggregation is also presented. The study of how the correlation in the power output and irradiance data affects various PV aggregation is also shown in this chapter. The effect of PV density on the variability of the aggregated PV fleets, how distance between PV sites also affects the aggregated PV systems are also presented. An analysis of the aggregation of

four PV fleets was done with different combinations of the PV fleets using statistical models and discrete meyer wavelet to study the reduction in variabilities with different combinations of the PV fleets. The result showed that the relative sizes of the PV fleets have significant impacts on the reduction in variabilities of the aggregated system. The correlation between these sites also shows significant influence in the reduction in variability of the aggregated PV systems. Also the larger the aggregated system, the more the reduction in variability.

## CHAPTER 4

### OPTIMIZATION ALGORITHMS FOR SMART INVERTER AND VOLTAGE CONTROL LEGACY DEVICES

Traditionally, LTCs with Voltage Regulators (VRs) and later capacitors were used by utility companies for voltage regulation. The LTCs basically switch the tapping of the transformers either up or down to effect the voltage of the feeders within the ANSI C84.1 standard range. The capacitors are used for reactive power injection which consequently leads to voltage control. Several studies have been done on the coordination of these two devices for optimal use for voltage regulation [174, 175]. Prior to the amendment made to the IEEE 1547a standard in 2014, Distributed Energy Resources (DERs) smart inverters were not permitted to participate in the distribution feeder voltage regulation. With the improvement of the smart inverter technologies, the amendment now allows the use of DERs such as PV systems to participate in the voltage regulation with other legacy devices such as On Load Tap Changing (OLTC) and capacitors [176].

Volt-VAR Optimization (VVO) control can be done at two levels in the distribution network. The first level is being the centralized VVO (or network-based VVO). This level of VVO is done at a centralized location that is integrated in the Distribution Management System (DMS). The main challenge of this system is the ability to process large data and provide VVO solutions in real or quasi-real time.

The decentralized level allows VVO to be done on the devices located on the feeders. The optimal control of these three devices is very important for smooth and economic operation of the whole system. Since these three devices have the capacity of adjusting the voltage profile of the feeders differently, therefore there is a need for optimal coordination within these three devices. With increasing deployment of inverter-based resources in distribution grids, the use of smart inverters (SIs) for voltage and reactive power (Volt-VAR) control becomes highly imperative



[177]. In the conventional control schemes, legacy grid devices such as on-load tap changers (OLTC) and capacitor banks (Caps) are used to for Volt-VAR control. However, due to the mechanical switching and the limits on number of operations per day, these legacy devices may not be adequate to mitigate fast voltage fluctuations caused by photovoltaics (PVs) [178]. On the other hand, inverter-based PVs have the capability to provide fast, flexible, and controlled active/reactive power support and could participate in voltage control [179]. Therefore, as effective and fast-responding active/reactive power resources, inverter-based PVs can be coordinated with the legacy grid devices to regulate voltage and reactive power in different timescale of operations.

In regards to coordinated control of SIs and legacy grid devices for Volt-VAR control for distribution optimal power flow (DOPF), several studies and algorithms are proposed in the literature. A bi-level Volt-VAR optimization (VVO) algorithm is proposed in [180]. The first level of optimization controls the legacy devices and SIs. Second level of optimization adjusts the control settings of the SI in order to achieve a feasible optimal power flow OPF solution. Both linear and non linear approximation for the power flow models are developed for levels 1 and 2 of the VVO respectively. Authors of [181] propose a two-time scale approach for Volt-VAR control on distribution feeders. The slow timescale control is applied to Caps and voltage regulators while the fast time scale control is applied to the SI. A hierarchically-coordinated volt-VAR control is proposed by [182]. The required reactive power setpoint to minimize the system power loss is dispatched by the central hierarchy while the local hierarchy uses the volt-VAR droop control to address the voltage deviation. Similar to [181], authors of [183] propose a combination of data-driven and physics-based optimization using two-timescale approach. The physics-based OPF determines the optimal set-points of the SIs while a deep reinforcement learning algorithm is used to optimal determine the optimal Caps status. Reference [184] propose two voltage optimization algorithms

that coordinates the operation of Caps and LTCs with aggregated reactive power and autonomous volt-VAR control of SIs. The objective of these algorithms (in [184] ) is to implement conservative voltage reduction. Similar to [185], authors of [186] optimized the OLTC tap position and Caps status in its stage one OPF (based on mixed-integer second order cone programming (MISOCP)) and uses a multi-agent deep deterministic policy gradient method to dispatch the required P-Q to mitigate fast voltage variation. The P-Q dispatch in this work is determined without using the SI droop settings.

## 4.1 Optimal Power Flow Methods

Several methods of solving optimal power flow problems have been developed in literature over past decades. Conventional methods (mathematical modeling-based approaches) include, linear programming, non-linear programming, quadratic programming, newton's method, and interior point method. Heuristic based approaches include swarm and bio-inspired optimization techniques, human inspired optimization techniques, evolutionary inspired optimization, physics inspired optimization, hybrid optimization and AI-based (artificial neural networks, deep learning and fuzzy logic based) approaches [187]. Since power flow problems are NP-hard, the main objective of these methods is to guarantee a global optimal solution. This thesis present two approaches to solving optimal power flow problem. The first approach uses the mathematical modeling approach by solving the non-linear programming problem while the second approach uses the Heuristic based approach based on genetic algorithm. OPF algorithms based on these two approaches are proposed and presented in 4.2 and 4.3

## 4.2 Mathematical modeling based Optimal Droop Setting of Smart Inverters in Coordination with Legacy Grid Devices

This section presents a multi-mode and multi-droop setting of smart inverter for two-stage optimal power flow (2S-OPF). In order to give the highest control priority to the smart inverters (SI), a modified hierarchical-control 2S-HOPF is also proposed. The first-stage OPF (formulated as a mixed integer non-linear programming (MINLP) problem) determines the status, mode and settings of voltage control devices, while the second stage OPF (formulated as a non-linear programming (NLP) problem) dispatches the active-reactive power of the SIs. The proposed approach is validated using the IEEE-123, unbalanced three-phase test feeder.

### 4.2.1 Modelling of SI Modes and Settings

The response of the SI to time-varying grid voltage depends on the modes and droop settings. The mathematical modelling of SI modes used in this paper and their droop controls are presented in this section.

#### **Volt-Watt (VW) mode**

In VW mode, the SI adjusts its active power injection in response to the voltage at the point of interconnection (POI). This mode of operation is used to curtail the active power at high POI voltages. If the  $X/R$  at the POI of the SI is significantly high, the feeder voltage might be less sensitive to active power control. The rate of change in active power injection due to change in the POI voltage is determined by the slope of the VW curve as shown in Fig. 4.1. The SI droop control in the VW mode is as expressed in (7.4).

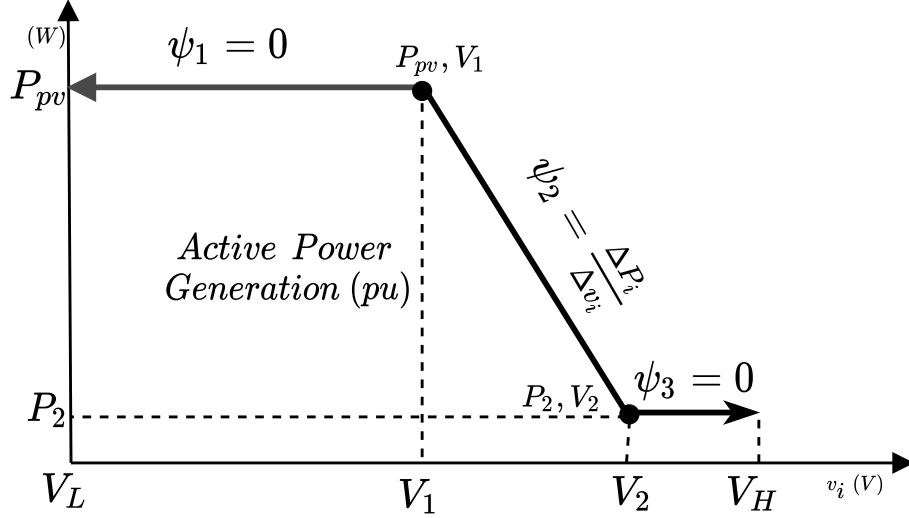


Figure 4.1: Volt-Watt curve.

$$\frac{\Delta v_i}{\Delta P_i} = \begin{cases} \text{Volt-Watt Control } \forall i \in \mathcal{N}_{pv} \\ 0 & V_L \leq v_i \leq V_1 \\ \frac{1}{\psi_2} & V_1 \leq v_i \leq V_2 \\ 0 & V_2 \leq v_i \leq V_H \end{cases} \quad (4.1)$$

where  $\psi = \frac{\Delta P_i}{\Delta v_i}$  is the slope of the VW curve within a given voltage range/band. Using the Heaviside step function, the VW control mode can be modelled as expressed in (4.2),

$$P_i^G = P_{pv} \left[ [H(v_i - V_L) - H(v_i - V_1)] + \frac{(V_2 - v_i) \times \psi_2}{P_2 - P_{pv}} [H(v_i - V_1) - H(v_i - V_2)] + \frac{P_2}{P_i^G} [H(v_i - V_2) - H(v_i - V_H)] \right] \forall i \in \mathcal{N}_{pv}. \quad (4.2)$$

where the discrete Heaviside function  $H : \mathbb{Z} \rightarrow \mathbb{R}$ , can be expressed as (4.3).

$$H(a) = \begin{cases} 0, & a < 0 \\ 1, & a \geq 0 \end{cases} \quad (4.3)$$

The reactive power constraint is expressed as (4.4).

$$\begin{aligned}
Q_i^G &\leq \sqrt{S_{SI} - P_i^G} \\
-Q_{pv} &\leq Q_i^G \leq Q_{pv}, \quad \forall i \in \mathcal{N}_{pv}
\end{aligned} \tag{4.4}$$

### Volt-VAR (VV) Mode

The VV mode is the commonly used and discussed SI mode in literature. This is due to the effectiveness of controlling the feeder voltage by reactive power injection or absorption especially with feeders with high  $X/R$ . The rate of reactive power injection and absorption using the VV mode is determined by the slopes of the VV curve as shown in Fig. 4.2. A dead-band is often added to the VV curve, enabling the SI to provide no reactive power within a particular voltage range. This helps to relax some aggressive need for constant voltage control with slight changes in voltage at POI around the nominal or reference voltage. In this mode reactive power dispatch is dispatch is made to follow a defined Volt-Watt droop settings. The SI droop control in the VV mode is as expressed in (7.5).

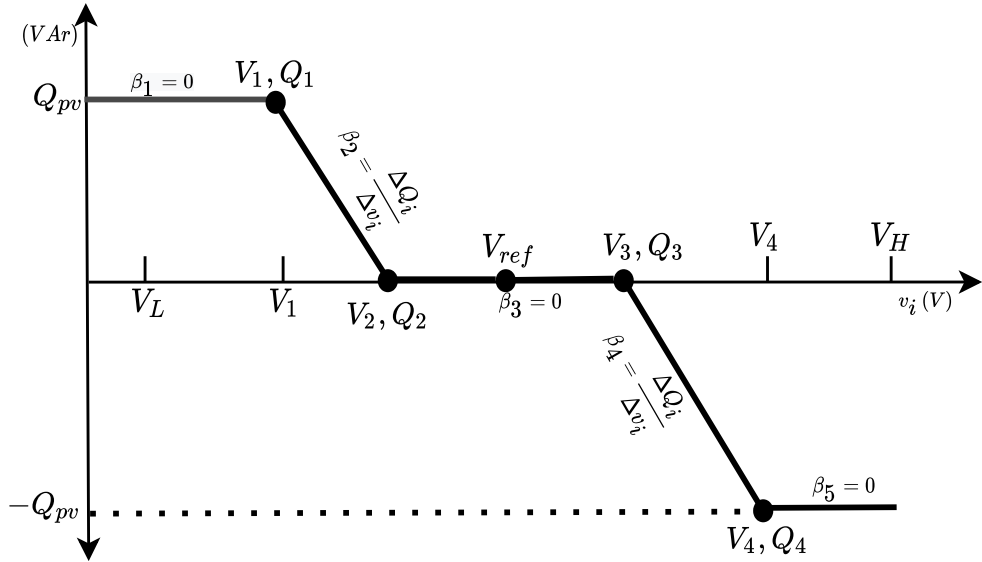


Figure 4.2: Volt-VAR curve.

$$\frac{\Delta v_i}{\Delta Q_i} = \begin{cases} \text{Volt-VAR Control } \forall i \in \mathcal{N}_{pv} \\ 0 & V_L \leq v_i \leq V_1 \\ \frac{1}{\beta_2} & V_1 \leq v_i \leq V_2 \\ 0 & V_2 \leq v_i \leq V_3 \\ \frac{1}{\beta_4} & V_3 \leq v_i \leq V_4 \\ 0 & V_4 \leq v_i \leq V_H \end{cases} \quad (4.5)$$

where  $\beta = \frac{\Delta Q_i}{\Delta v_i}$  is the slope of the VV curve within a given voltage range/band. Using the Heavside step function, the VV mode can be modelled as expressed in (4.6).

$$\begin{aligned} Q_i^G = Q_{pv} & \left[ [H(v_i - V_L) - H(v_i - V_1)] - \right. \\ & \frac{(V_2 - v_i) \times \beta_2}{Q_{pv}} [H(v_i - V_1) - H(v_i - V_2)] + \\ & [H(v_i - V_2) - H(V_3 - v_i)] - \\ & \frac{(V_3 - v_i) \times \beta_4}{Q_{pv}} [H(v_i - V_3) - H(v_i - V_4)] + \\ & \left. [H(v_i - V_H) - H(v_i - V_4)] \right] \forall i \in \mathcal{N}_{pv} \end{aligned} \quad (4.6)$$

The active power constraint is expressed as (4.7).

$$\begin{aligned} P_i^G & \leq \sqrt{S_{SI} - Q_i^G} \\ P_2 & \leq P_i^G \leq P_{pv}, \quad \forall i \in \mathcal{N}_{pv} \end{aligned} \quad (4.7)$$

The VV mode can be operated as either in VAR-priority mode (Q-priority) or Watt-priority (P-priority) as shown in Fig. 4.3a.

### **Volt-VAr with reactive power priority (Q-Priority)**

In the VV (Q-priority) mode, the reactive power generation/absorption by the SI is prioritized over active power generation. This will enable the SI to curtail some

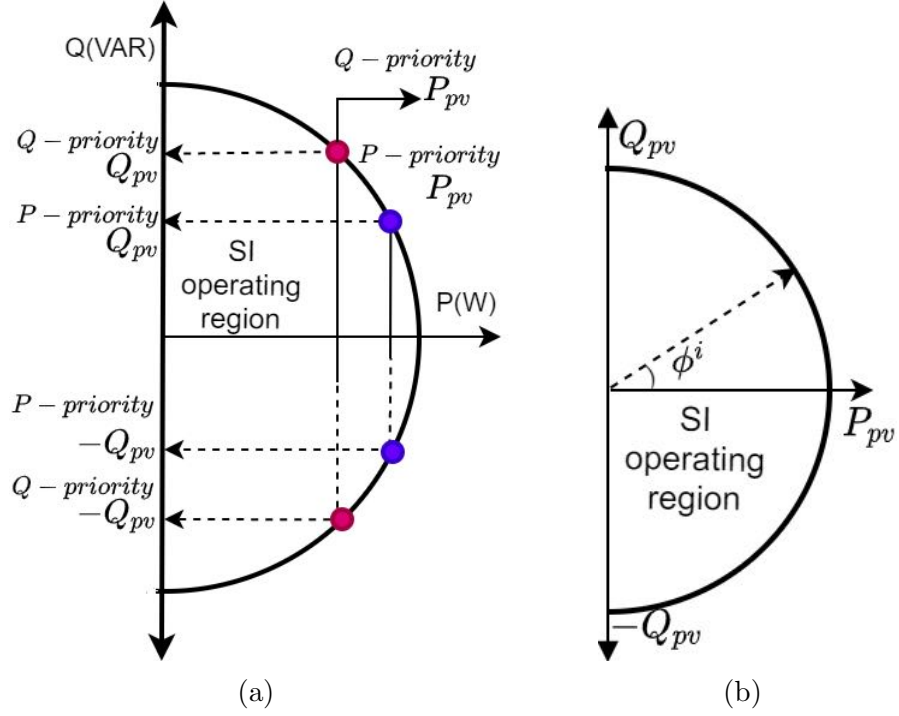


Figure 4.3: (a) SI operating region in Volt-VAR (P/Q priority) mode [3] (b) CPF operating quadrants for active and reactive power dispatch.

active power whenever there isn't enough headroom or capacity to provide the required amount of reactive power to regulate the voltage at the POI based on the SI's droop settings. The active power dispatched in this mode is as expressed in (4.8).

$$P_i^G \leq \sqrt{(S_{SI})^2 - (Q_i^G)^2}, \quad \forall i \in \mathcal{N}_{pv} \quad (4.8)$$

where  $Q_{pv} \leq S_{SI}$ ;  $P_2 \leq P_i^G \leq P_{pv}$  and  $P_i^{curt} = P_{pv} - P_i^G$

### Volt-VAr with active power priority (P-priority)

In VV P-priority mode, the entire active power based on the prevailing irradiance is available for dispatch. Depending on the SI apparent power capacity, the reactive power is dispatched based on the nodal voltage at the POI of the SI. The available reactive power dispatch in this mode is as expressed in (4.9).

$$Q_i^G \leq \sqrt{(S_{SI})^2 - (P_{pv})^2}, \quad \forall i \in \mathcal{N}_{pv}. \quad (4.9)$$

### Constant power factor (CPF) mode

The CPF mode allows the SI to inject or absorb a fixed amount of reactive/active power in order to regulate the feeder voltage. This setting is commonly used for small scale (also rooftop) PV systems. Assuming the SI can operate in two quadrants of active and reactive power dispatch, the CPF mode is as shown in Fig. 4.3b.

$$Q_i^G = P_{pv} \tan \phi_i, \quad \forall i \in \mathcal{N}_{pv} \quad (4.10)$$

where

$$\phi_i^{min} \leq \phi_i \leq \phi_i^{max} \quad (4.11)$$

### 4.2.2 Feeder voltage sensitivity analysis and modelling

The effectiveness of voltage control devices in regulating the voltage of the feeder at the POI is dependent on the sensitivity of the feeder voltage to various control actions by SIs, OLTC and CAPS. The effective voltage deviation and control achieved across the entire feeder is a combination of the effects of the control actions taken by these voltage control devices. Fig. 4.4 shows several grid-connected PV systems with  $R_i^{eq}$  and  $X_i^{eq}$  as seen from the POI with OLTC/VR, and CAPS. The value of  $R_i^{eq}$  and  $X_i^{eq}$   $\forall i \in \mathcal{N}$  can be obtained from real and imaginary components of the  $B_i$  value of the  $ABCD$  matrix parameters as seen from the POI relative to the substation node.



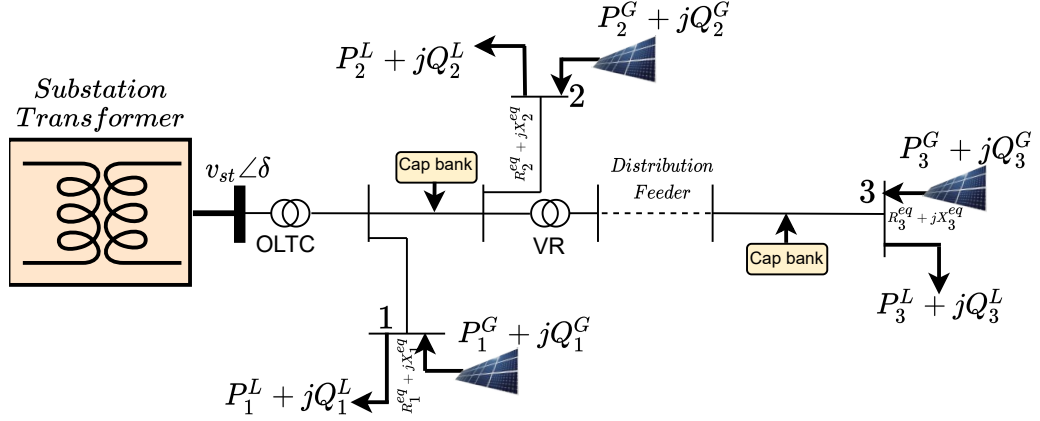


Figure 4.4: A distribution grid-connected PV systems with CAPS and OLTC/VR.

### Feeder's voltage sensitivity to Power Injection

Based on the different SI modes, the voltage sensitivity of the feeder at the POI due to the injection of active and reactive power injection can be derived as follows. Taking  $\Delta P_i = P_i^G - P_i^L$ ,  $\Delta Q_i^G = Q_i^G - Q_i^L \forall i \in \mathcal{N}$  where  $P_i^G = 0$  and  $Q_i^G = 0 \forall i \in \mathcal{N} \setminus \mathcal{N}_{pv}$

$$v_i = v_{st} - \left\{ \frac{\Delta P_i^G - \mathbf{j}\Delta Q_i^G}{v_i \angle \delta_i} \right\} (R_i^{eq} + \mathbf{j}X_i^{eq}), \quad \forall i \in \mathcal{N} \quad (4.12)$$

$$v_i = v_{st} - \left[ \frac{\Delta P_i^G (R_i^{eq} \cos \delta_i - X_i^{eq} \sin \delta_i)}{v_i} + \frac{\Delta Q_i^G (X_i^{eq} \cos \delta_i + R_i^{eq} \sin \delta_i)}{v_i} \right] \quad \forall i \in \mathcal{N} \quad (4.13)$$

In order to simplify (4.13), since the value of  $\delta_i$  is usually very small, the value of  $\cos \delta_i \approx 1$  and  $\sin \delta_i \approx 0$  [188]; therefore the change in voltage across all the feeder nodes with respect to active and reactive power injection by the PVs ( $\Delta v_{pv}$ ) can be approximately expressed as (4.14) [189].

$$\Delta v_i^{pv} \approx \frac{R_i^{eq} \Delta P_i^G + X_i^{eq} \Delta Q_i^G}{v_i} \quad (4.14)$$

The approximation in (4.14) is accurate enough [190, 191] to determine the feeder voltage deviation as a result of  $P_i^G$  and  $Q_i^G$  based on the SI droops and modes presented in section 4.2.1.

### Feeder's voltage sensitivity to OLTC/VR tap change

Tap changing the OLTC/VR can be used to adjust the nodal voltages of the feeder. Typical voltage regulators have 32 discrete steps with  $1 \pm 10\%$ pu voltage regulation range. Each discrete tap step ( $tp$ ) produces a voltage deviation of 0.00625 pu. The ratio of the secondary to primary voltage (tap ratio  $\alpha$ ) is as expressed in (4.15) [192].

$$\alpha_i = 1 + \frac{tp_i}{tp_{\max}} (\alpha_{\max} - 1) \quad \forall i \in \mathcal{N}_{tp} \quad (4.15)$$

Each tap change modifies the value of  $\alpha_i$  which in turn changes the impedance matrix by  $\Delta Z(tp_i)$  of the feeder as expressed in (4.16).

$$\Delta Z(tp_i) = -Y_0^{-1} \cdot \Delta Y(tp_i) \cdot Y_0^{-1}; \quad \forall i \in \mathcal{N}_{tp} \quad (4.16)$$

The voltage deviation across all the nodes  $i \in \mathcal{N}$  in the feeder as a result of the change in tap position (4.17)

$$\Delta v_i^{tp} = \Delta Z(tp_k) \cdot I_0 + Z_0 \cdot \Delta I(tp_k); \quad \forall k \in \mathcal{N}_{tp}, \forall i \in \mathcal{N} \quad (4.17)$$

### Feeder voltage sensitivity to shunt cap bank status

The cap bank injects reactive power based on its VAR rating and status (On/Off). The reactive power injection  $Q_i^c$  at node  $i \in \mathcal{N}_C$  can be expressed as (4.18).

$$Q_i^c = q_i^c \times tc_i; \quad tc_i \in [0, 1]; \quad \forall i \in \mathcal{N}_C \quad (4.18)$$

Assuming  $\mathcal{N}_C \cap \mathcal{N}_{pv} = \emptyset$ ;  $\Delta Q_i^c = Q_i^c - Q_i^L$ ,  $\forall i \in \mathcal{N}$  where  $Q_i^c = 0$ ;  $\forall i \in \mathcal{N} \setminus \mathcal{N}_C$ .

The voltage deviation across all nodes  $i \in \mathcal{N}$  due to the reactive power injection by the Caps can be expressed as;  $\Delta v_i^c = \frac{1}{v_i} \cdot X_i^{eq} \cdot \Delta Q_i^c$ .

### 4.2.3 Optimal Power Flow Formulation

The total voltage deviation as a result of the voltage control action of the SIs, CAPS and OLTC/VR is set as the objective function as expressed in (4.19),

$$\text{Min} \sum_{i \in \mathcal{N}} \left| \frac{R_i^{eq} \Delta P_i^G + X_i^{eq} \Delta Q_i^G}{v_i} + \frac{1}{v_i} X_i^{eq} \Delta Q_i^c + \sum_{k \in \mathcal{N}_{tp}} \Delta Z(tp_k) \cdot I_0 + Z_0 \cdot \Delta I(tp_k) \right| \quad (4.19)$$

The distribution grid is modelled and set as part of the optimization constraints using the power flow equations in (4.20)- (4.24) [193].

$$P_i^L - \sum_{k \in \mathcal{N}_{pv}} P_k^G - P_0^{st} = -\mathcal{G}_i |v_i|^2 - \sum_{j:i \rightarrow j} P_{ij} + \sum_{k:k \rightarrow i} (P_{ki} - r_{ki} |I_{ki}|^2); \quad \forall i \in \mathcal{N} \quad (4.20)$$

$$Q_i^L - \sum_{k \in \mathcal{N}_{pv}} Q_k^G - Q_0^{st} - \sum_{m \in \mathcal{N}_C} Q_m^c = -\mathcal{B}_i |v_i|^2 - \sum_{j:i \rightarrow j} Q_{ij} + \sum_{k:k \rightarrow i} (Q_{ki} - r_{ki} |I_{ki}|^2); \quad \forall i \in \mathcal{N} \quad (4.21)$$

$$v_i = v_k - (r_{ki} + \mathbf{j}x_{ki}) I_{ki}; \quad \forall (k, i) \in \mathcal{L} \quad (4.22)$$

$$I_{ki} = \left( \frac{P_{ki} + \mathbf{j}Q_{ki}}{v_i} \right)^*; \quad \forall (k, i) \in \mathcal{L} \quad (4.23)$$

The nodal voltage constraint in the network is as expressed in (4.24),

$$v_i^{min} \leq v_i \leq v_i^{max}, \quad \forall i \in \mathcal{N}. \quad (4.24)$$

The control of the legacy devices makes this formulation a Mixed Integer Non-linear Programming (MINLP) problem for the first stage of the OPF which requires solving (4.19) subject to (4.25). Since the second stage does not include

dispatching the integer and binary variables of the legacy devices, it can be formulated as a Non-Linear Program (NLP) which requires solving (4.19) subject to (4.26).

$$\text{Stage-1} \left\{ \begin{array}{l} SIM_i \in [m_1 \dots m_5], \quad \forall i \in \mathcal{N}_{pv} \\ SIS_i \in [V_L \dots V_H, \phi_i], \quad \forall i \in \mathcal{N}_{pv} \\ tp_i \in [-16, \dots, +16], \quad \forall i \in \mathcal{N}_{tp} \\ Q_i^c = q_i^c tc_i, \quad \forall i \in \mathcal{N}_c \quad \text{where } tc_i \in [0, 1] \\ (4.4), (4.7), (4.11), (4.20) - (4.24) \end{array} \right. \quad (4.25)$$

$$\text{Stage-2} \left\{ \begin{array}{l} SIM_i = SIM_i^{opt} \quad \forall i \in \mathcal{N}_{pv} \\ SIS_i = [V_L \dots V_H, \phi_{pv}]^{opt} \quad \forall i \in \mathcal{N}_{pv} \\ tp_i = tp_i^{opt} \quad \forall i \in \mathcal{N}_{tp} \\ Q_i^c = q_i^c tc_i^{opt} \quad \forall i \in \mathcal{N}_c \\ P_2 \leq P_i^G \leq P_{pv}, \quad \forall i \in \mathcal{N}_{pv} \\ -Q_{pv} \leq Q_i^G \leq Q_{pv}, \quad \forall i \in \mathcal{N}_{pv} \\ (4.20) - (4.24) \end{array} \right. \quad (4.26)$$

#### 4.2.4 Proposed Hierarchical Coordination

This paper proposes a 2-stage OPF for voltage optimization which uses five SI modes, namely: Volt-Watt, Volt-Var (P-priority), Volt-Var (Q-priority) and CPF (leading and lagging). The flow charts of the proposed 2S-OPF and 2S-HOPF algorithms is as shown in Figs 4.5 and 4.6 respectively.

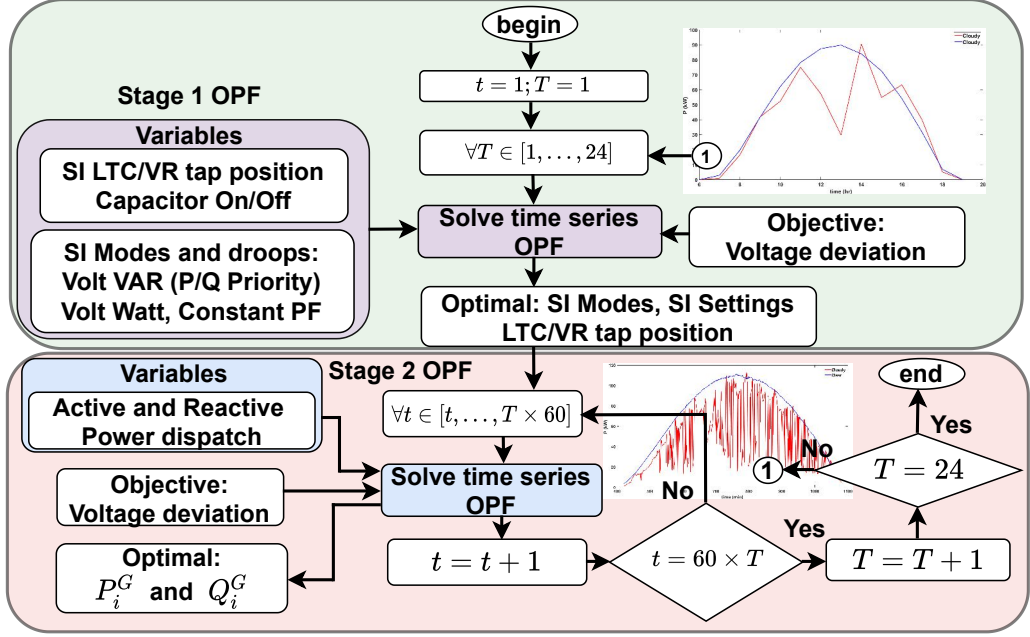


Figure 4.5: Flow chart of the proposed 2S-OPF algorithm.

#### 4.2.5 2S-OPF

In 2S-OPF the control variables of the first stage OPF are the five modes of the SIs, the breakpoints of the SI droop based on the modes, the PF values (for SI CPF mode), the OLTC/VR settings and the CAPS status. The control variables for the second stage OPF are the active and reactive power dispatch of the SIs. The algorithm starts by solving a 1-hour resolution OPF using the defined first-stage control variables with the objective function defined as expressed in (4.19). The results of the first-stage ( $SIM_i^{opt}$ ,  $SIS_i^{opt}$ ,  $tc_i^{opt}$  and  $tp_i^{opt}$ ) are passed to the second stage OPF. The second stage OPF is solved using the values of  $SIM_i^{opt}$ ,  $SIS_i^{opt}$ ,  $tc_i^{opt}$  and  $tp_i^{opt}$  with the active power and reactive power as the optimization control variables at a 1-minute resolution. Using the hourly optimal values for the first-stage OPF, the second stage is solved 60 times after which the first-stage OPF is solved again. The Pseudo-code for the proposed 2S-OPF is as presented in algorithm 1.

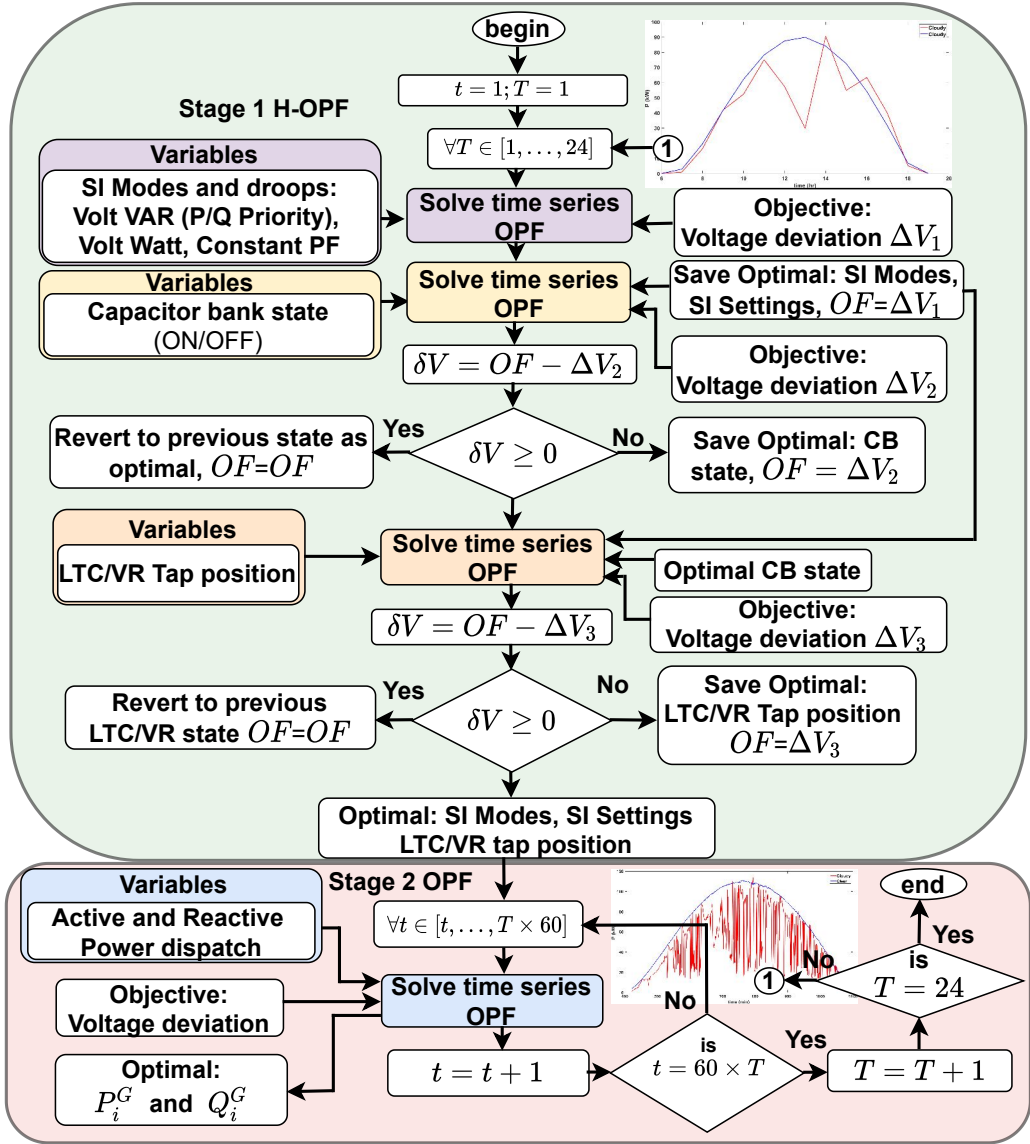


Figure 4.6: Flow chart of the proposed 2S-HOPF algorithm.

#### 4.2.6 2S-HOPF

In order to reduce the numbers of OPF control variables solved at one go (to improve computational efficiency and allow SI carry more voltage regulation) in the first stage OPF, the OPF control variables were solved sequentially in the 2S-HOPF. In the hierarchical approach (as shown in Fig. 4.6), the optimal modes and settings of the SI is of the highest priority. Within the stage-1 OPF, a first sub-stage-1 OPF is solved which determines  $SIM_i^{opt}$  and  $SIS_i^{opt}$ . This is done to

---

**Algorithm 1** Two-Stage OPF without Hierarchical control.

---

```

1: procedure  $SIM_i^{opt}, SIS_i^{opt}, tp_i^{opt}, tc_i^{opt}, Q_{i,t}^G, P_{i,t}^G \forall i \in \mathcal{N}_{pv}$ 
2:   Begin time  $T=1$ 
3:   Begin time  $t=1$ 
4:   while  $T \leq 24$  do
5:     Solve (21) s.t. (25)
6:     while  $t \leq 60 \times T$  do
7:       Solve (21) s.t. (26)
8:       if  $t = T \times 60$  then
9:          $T=T+1$ 
10:        Execute step 4
11:       else
12:          $t=t+1$ 
13:        Execute step 6
14:       end if
15:     end while
16:   end while
17: end procedure

```

allow the SI to actively carryout the voltage regulation to its maximum capacity. Afterwards, the values of  $SIM_i^{opt}$  and  $SIS_i^{opt}$  are passed to second sub-stage-1 OPF. In the second sub-stage-1 OPF, the CAPS status  $tc_i$  is set as the optimization control variable. The value of the voltage deviation objective is computed and compared to the voltage deviation objective obtained the first sub-stage-1 OPF. If the later is lesser, the new optimal values of  $tc_i^{opt}$  is saved and if otherwise, the status of  $tc_i^{opt}$  is reverted to its previous state. The updated objective function is set as the lower value. The values of  $SIM_i^{opt}$ ,  $SIS_i^{opt}$ , and  $tc_i^{opt}$  are passed to the third sub-stage-1 OPF while the tap position  $tp^i$  is set as the control variable. The value of the newest voltage deviation objective is computed and compared to the voltage deviation objective obtained the updated second sub-stage-1 OPF. If the later is lesser, the new optimal values of  $tp_i^{opt}$  is saved and if otherwise, the tap position  $tp_i^{opt}$  is reverted to its previous tap position. The updated objective function is set as the lower value. The updated values of  $SIM_i^{opt}$ ,  $SIS_i^{opt}$ ,  $tc_i^{opt}$  and  $tp_i^{opt}$  are passed to the stage-2 OPF. As described in the previous 2S-OPF algorithm, a high resolution OPF (1-minute) is solved to optimally dispatch the

---

**Algorithm 2** Two-Stage OPF with Hierarchical Control
 

---

```

1: procedure  $SIM_i^{opt}, SIS_i^{opt}, tp_i^{opt}, tc_i^{opt}, Q_{i,t}^G, P_{i,t}^G \forall i \in \mathcal{N}_{pv}$ 
2:   Begin time  $T=1$ 
3:   Begin time  $t=1$ 
4:   while  $T \leq 24$  do ▷ Solve 1-hr HOPF
5:     Solve (21) s.t. (25) ▷  $\Delta v_1, SIM_{i,T}^{opt}, SIS_{i,T}^{opt}$ 
6:      $OF = \Delta v_1$ 
7:     Solve (21) s.t. (25) ▷  $\Delta v_2, tc_{i,T}^{opt}$ 
8:      $\delta V = OF - \Delta v_2$ 
9:     if  $\delta V > 0$  then
10:       $tc_{i,T}^{opt} = tc_{i,T}^{opt}$ 
11:       $OF = \Delta v_2$ 
12:     else
13:       $tc_{i,T}^{opt} = tc_{i,T-1}^{opt}$ 
14:       $OF = OF$ 
15:     end if
16:     Solve (21) s.t. (25) ▷  $\Delta v_3, tp_{i,T}^{opt}$ 
17:      $\delta v = OF - \Delta v_3$ 
18:     if  $\delta v > 0$  then
19:       $tp_{i,T}^{opt} = tp_{i,T}^{opt}$ 
20:       $OF = \Delta v_3$ 
21:     else
22:       $tp_i^{opt} = tp_i^{opt, T-1}$ 
23:       $OF = OF$ 
24:     end if ▷  $SIM_{i,T}^{opt}, SIS_{i,T}^{opt}, tp_{i,T}^{opt}, tc_{i,T}^{opt}$ 
25:     while  $t \leq 60 \times T$  do ▷ Solve 1-min OPF
26:       Solve (21) & (26) ▷ Solve  $Q_i^G, P_i^G$ 
27:       if  $t = T \times 60$  then
28:          $T=T+1$ 
29:         Execute step 4
30:       else
31:          $t=t+1$ 
32:         Execute step 25
33:       end if
34:     end while
35:   end while
36: end procedure

```

---



active and reactive power by the PVs. The Pseudo-code for the proposed 2S-HOPF is as presented in algorithm 2.

## 4.2.7 Simulation Results and Analysis

This section presents the simulation setup and the results of the proposed 2S-OPF and 2S-HOPF algorithms.

### Simulation Setup

In order to validate the effectiveness of the proposed DOPF models and hierarchical coordination, the IEEE 123-node system, as shown in Fig. 4.7, is considered.

The IEEE 123-node test feeder has a nominal voltage of 4.16 kV with four voltage regulators (VR<sub>1</sub>, VR<sub>2</sub>, VR<sub>3</sub> and VR<sub>4</sub>) and four CAPS (Cap<sub>1</sub>, Cap<sub>2</sub>, Cap<sub>3</sub> and Cap<sub>4</sub>). The CAPS include one 600 kVAR three-phase and three 50 kVAR single-phase. Ten units of PV systems rated 100 kW are integrated into the feeder. The PV's SIs were sized at 125% of the maximum DC capacity of the PVs. For the Volt-VAR (P-priority), the maximum  $Q_{pv} = \frac{\sqrt{1.25^2 - 1^2}}{1.25} = 0.6$  [194] while for the Volt/VAR (Q-priority), the maximum  $Q_{pv} \leq S_{SI}$  [195]. It is worthy of note that in the Volt/VAR (Q-priority) mode, the SI is allowed to curtail the active power as much as required by the setting  $Q_{pv} \leq S_{SI}$ . Each SIs is allowed to take five modes (set as variables in stage-1) which include: Volt-Watt, Volt VAR P-priority, Volt VAR Q-priority, constant power factor (CPF: leading and lagging)). The simulation is done for both cloudy and clear day PV generation. The profile of the PV generation on the sunny and cloudy day is as shown in Fig. 4.5 and 4.6. As seen in Figs. 4.5 and 4.6, the hourly PV generation profile is used to dispatch the optimal OLTC/VR tap position, CAPS status and SI modes and settings while the one-minute resolution PV generation profile is used for the dispatch of the SI's active-reactive power. The first stage MINLP OPF formulation is solved using the OPTI optimization MATLAB toolbox with the NOMAD algorithm [196]

while the second stage NLP problem is modeled in MATLAB and solved using ‘fmincon’ solver with a sequential quadratic programming (SQP) algorithm set in ‘fmincon’. The simulation is run on an Intel<sup>®</sup> Core i5-7400 @ 3.0Ghz processor with 24GB RAM computer.

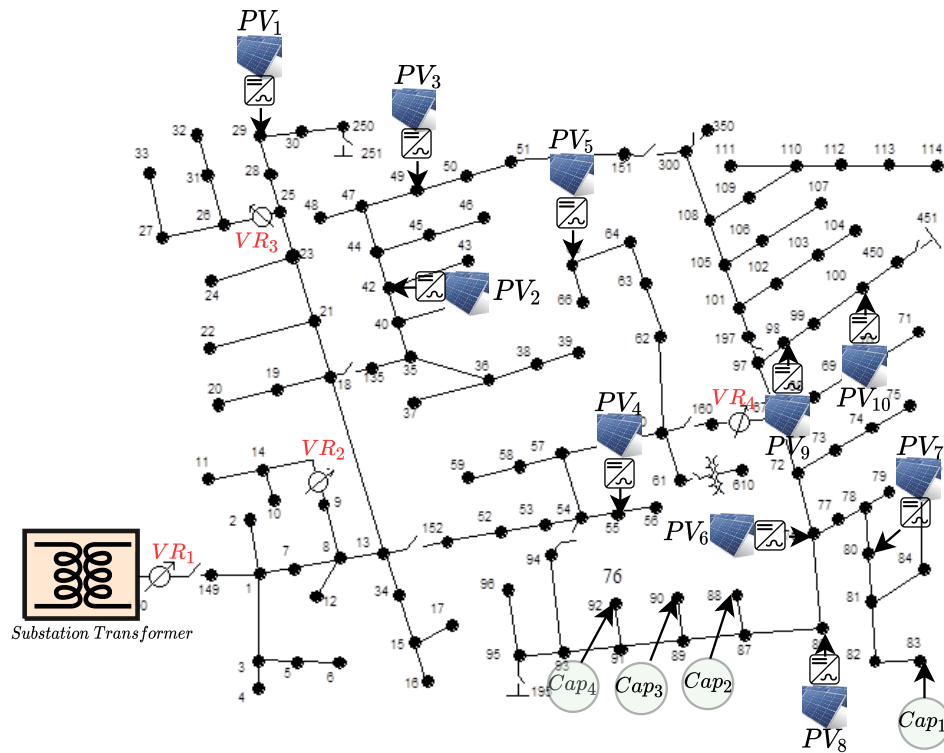
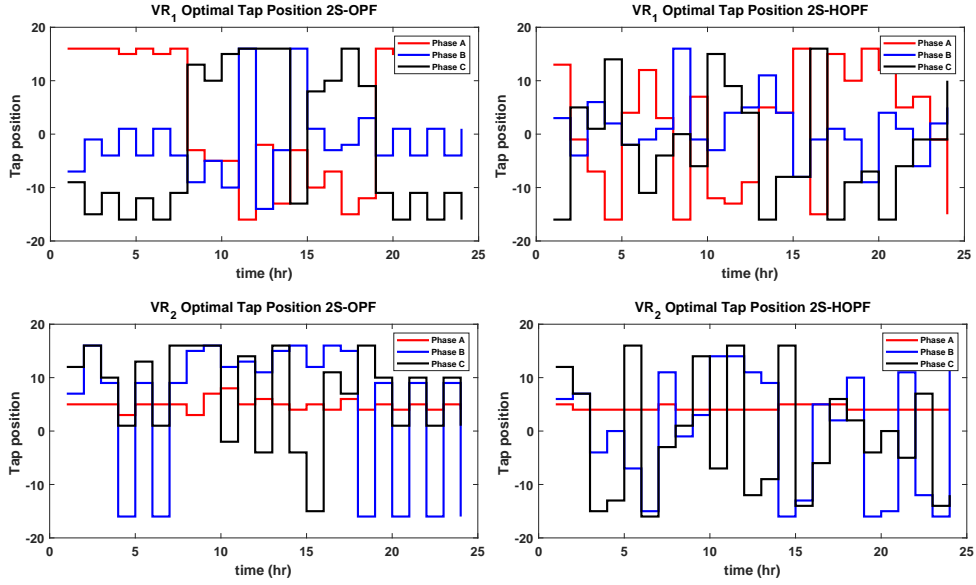


Figure 4.7: IEEE 123 test node system with ten PVs integrated.

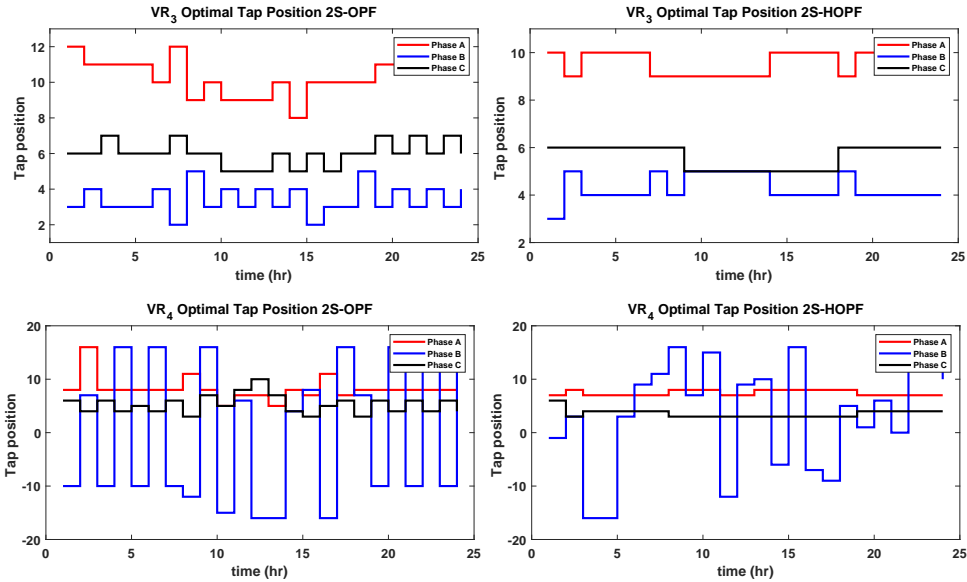
### Optimal Tap positions and CAPS status

The optimal tap positions using the proposed 2S-OPF and 2S-HOPF algorithms for VR<sub>1</sub>, VR<sub>2</sub>, VR<sub>3</sub>, and VR<sub>4</sub> on cloudy and clear days are as shown in Fig. 4.8 and 4.9 respectively.

Due to the hierarchy of operation introduced in the 2S-HOPF algorithm, the number of tap operations is reduced. The summary of the tap changes for the four voltage regulated in tabulated in Table 4.2. The total tap changes with the 2S-OPF (cloudy and clear day) is 230 while that of 2S-HOPF (cloudy and clear day) is 165 and 164 respectively. This shows  $\approx 28\%$  reduction in the tap operation



(a)



(b)

Figure 4.8: Optimal Tap positions on cloudy day for  $VR_1$ - $VR_4$  (a) 2S-OPF (b) 2S-HOPF.

with the use of 2S-HOPF compared to that of the 2S-OPF. Table 4.2 also shows an  $\approx 17\%$  increase in CAPS utilization with the use of 2S-HOPF compared to that of the 2S-OPF.

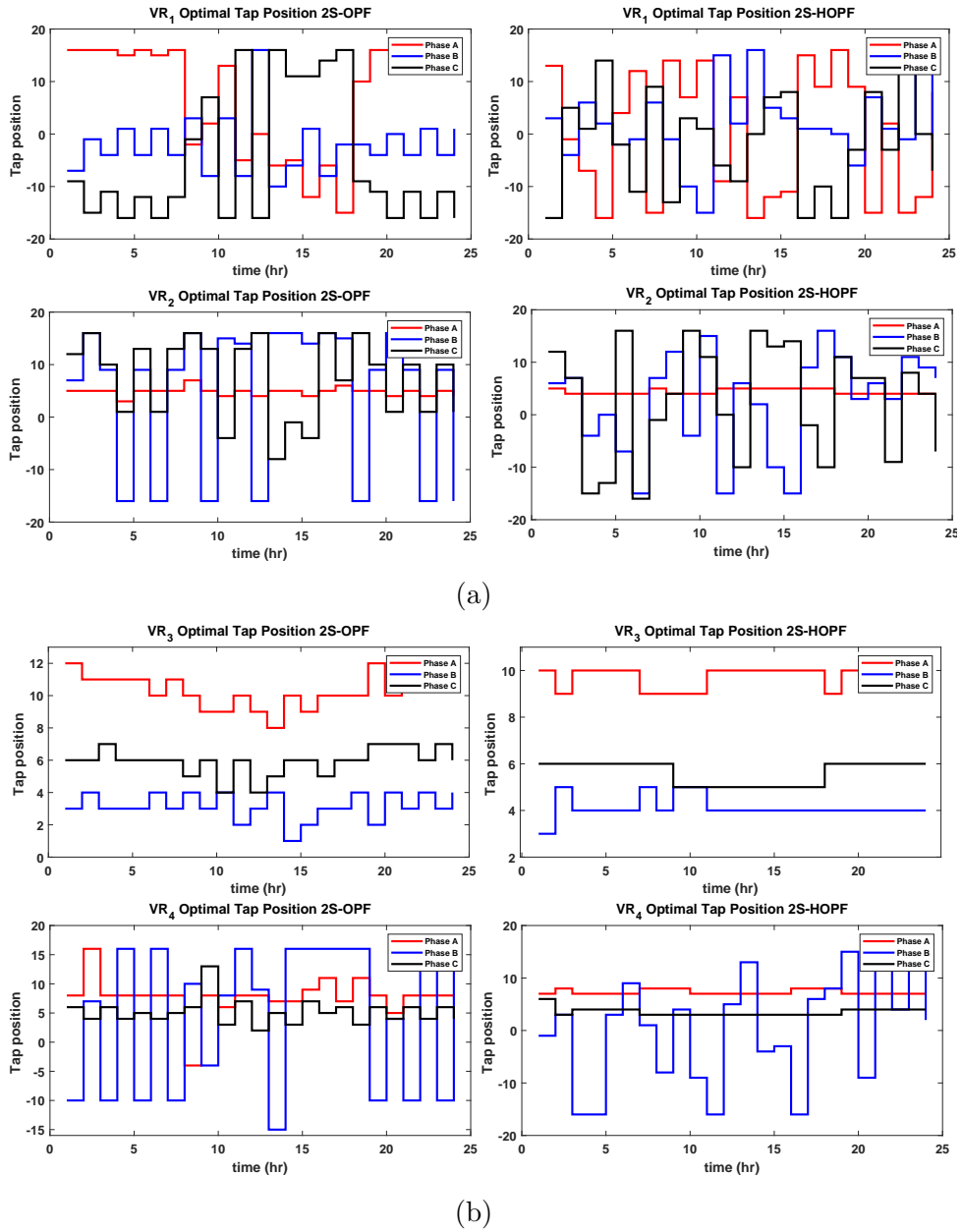


Figure 4.9: Optimal Tap positions on clear day for  $VR_1$ - $VR_4$  (a) 2S-OPF (b) 2S-HOPF.

### Optimal SI modes and settings

The optimal SI modes and settings for stage-one OPF based on both cloudy (2S-OPF and 2S-HOPF) and clear (2S-OPF and 2S-HOPF) day PV generation is as shown in figures 4.10a, 4.10b, 4.11a, and 4.11b respectively.

Table 4.1: Tap changes for 2S-OPF and 2S-HOPF

	Cloudy day						Clear day					
	2S-OPF			2S-HOPF			2S-OPF			2S-HOPF		
	Ph A	Ph B	Ph C	Ph A	Ph B	Ph C	Phase A	Ph B	Ph C	Ph A	Ph B	Ph C
VR <sub>1</sub>	20	23	21	23	23	21	19	22	22	23	22	23
VR <sub>2</sub>	19	23	21	5	22	23	17	22	23	5	23	22
VR <sub>3</sub>	10	20	16	6	8	2	14	20	15	6	6	2
VR <sub>4</sub>	12	22	23	6	22	4	14	19	23	6	22	4
Total	230			165			230			164		

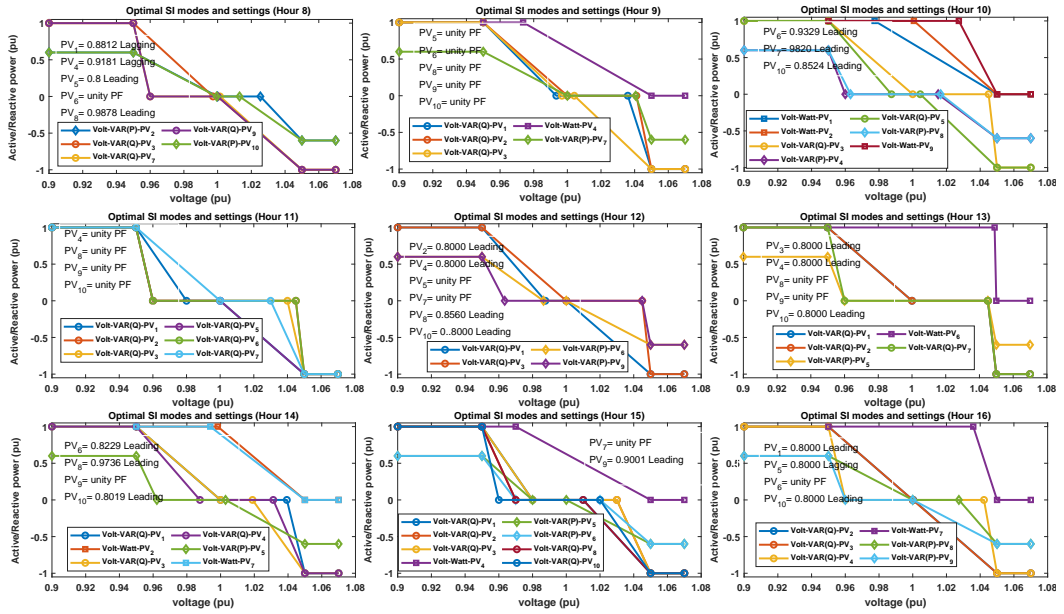
Table 4.2: CAPS status for 2S-OPF and 2S-HOPF

	Cloudy day		Clear day	
	2S-OPF	2S-HOPF	2S-OPF	2S-HOPF
	Cap <sub>1</sub> , Cap <sub>2</sub> , Cap <sub>3</sub> and Cap <sub>4</sub> , $\sum_1^{24} tc_{i,T}^{opt}$			
ON	76	92	72	89
OFF	20	4	24	7

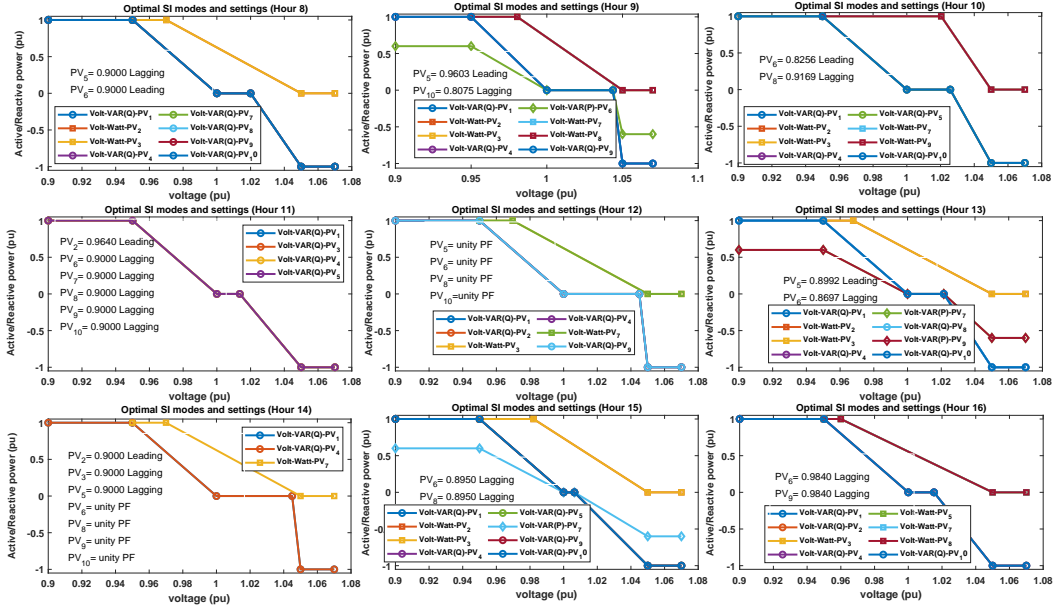
As seen in figures 4.10a, 4.10b, 4.11a, and 4.11b, the algorithm effectively selects the optimal modes of the SIs for each hour. All the possible SI modes (volt-Watt, Volt-VAR (P-priority), Volt-VAR (Q-priority), CPF (leading and lagging)) considered during the optimization are used by the SIs for effective voltage regulation. In comparison to the 2S-OPF, the 2S-HOPF's SI Volt-VAR (P-priority), Volt-VAR (Q-priority) settings have smaller dead-bands which means the SI will act more frequently to regulate the feeder voltage compared to that of 2S-OPF. The summary of the optimal SI modes deployed by both algorithms is as presented in Table 4.3.

#### 4.2.8 Active and reactive power dispatch

Using the values of  $SIM_i^{opt}$ ,  $SIS_i$ ,  $tc_i^{opt}$  and  $tp_i^{opt}$ , the second-stage OPF for one-minute resolution is solved to determine  $Q_i^G, P_i^G$ . The P-Q dispatch for cloudy and clear day is as shown in Figs. 4.12a and 4.12b respectively. The active power curtailment for both algorithms (for cloudy and clear day) is also shown in Fig. 4.12c.



(a)



(b)

Figure 4.10: Optimal SI modes and Settings (a) cloudy day 2S-OPF (b) cloudy day 2S-HOPF (c) clear day 2S-OPF (b) clear day 2S-HOPF.

It can be seen from the active power dispatch that both algorithms curtails the active power at some intervals and injected/absorbed for effective voltage regulation during cloudy and clear scenarios. Within the time period considered, the 2S-OPF curtails a total energy of 80.7 kWhr (rate of 3.26 kW/min) on the

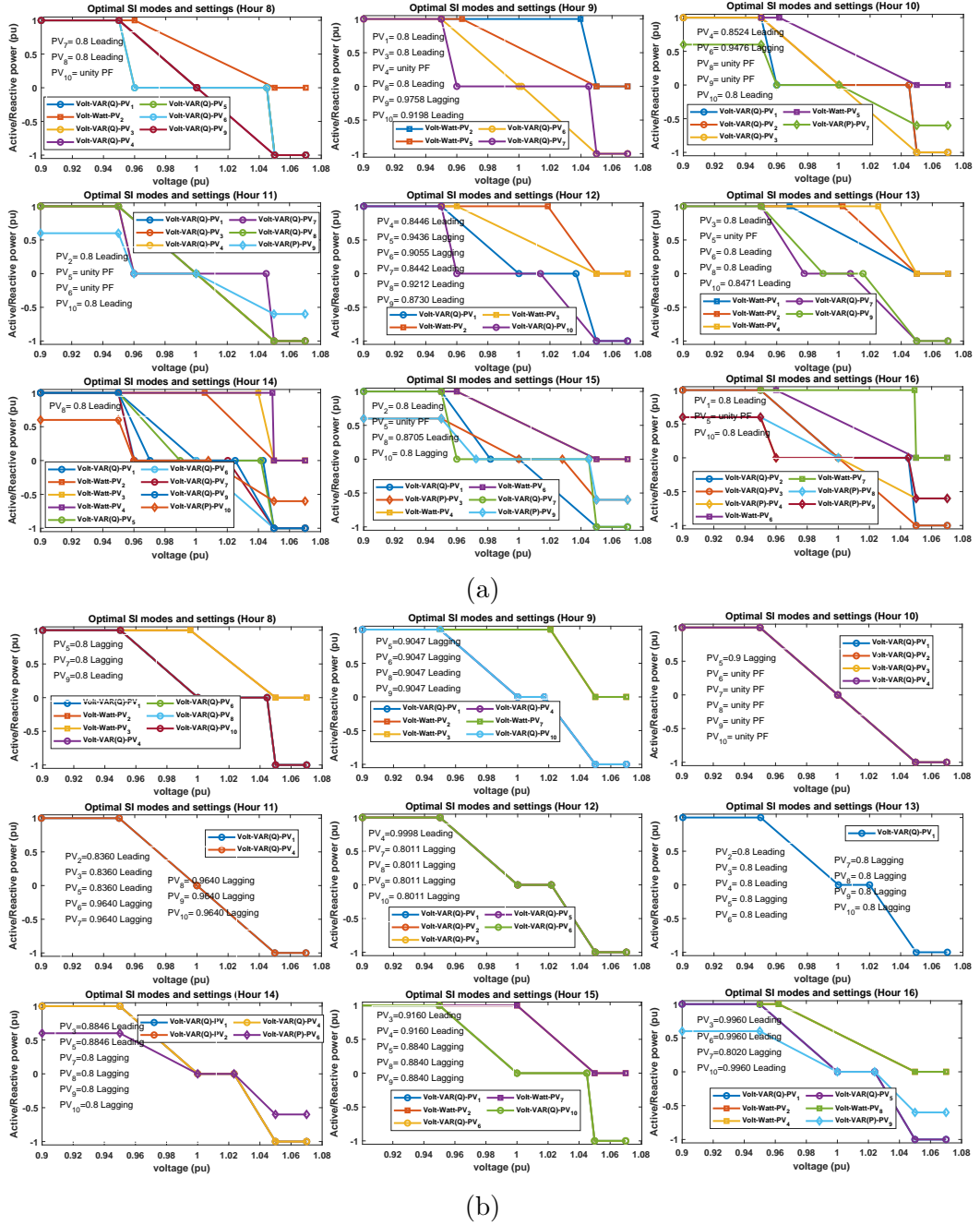


Figure 4.11: Optimal SI modes and Settings (a) cloudy day 2S-OPF (b) cloudy day 2S-HOPF (c) clear day 2S-OPF (d) clear day 2S-HOPF.

cloudy day and 254 kWhr (rate of 3.26 kW/min) on the clear day. Also, the 2S-HOPF curtails a total energy of 221.5 kWhr (rate of 9.23 kW/min) on the cloudy day and 161.6 kWhr (rate of 6.73 kW/min) on the clear day. The active power curtailment by both algorithms is determined the optimal SI modes and settings.

Table 4.3: SI modes using 2S-OPF vs 2S-HOPF (Hour 8-16)

Cloudy day		
	2S-OPF	2S-HOPF
CPF (Leading & Lagging)	38	29
Volt-Watt	9	21
Volt-VAR (P-Priority)	13	4
Volt-VAR (Q-Priority)	30	36
Clear day		
CPF (Leading & Lagging)	37	50
Volt-Watt	16	10
Volt-VAR (P-Priority)	8	2
Volt-VAR (Q-Priority)	29	28

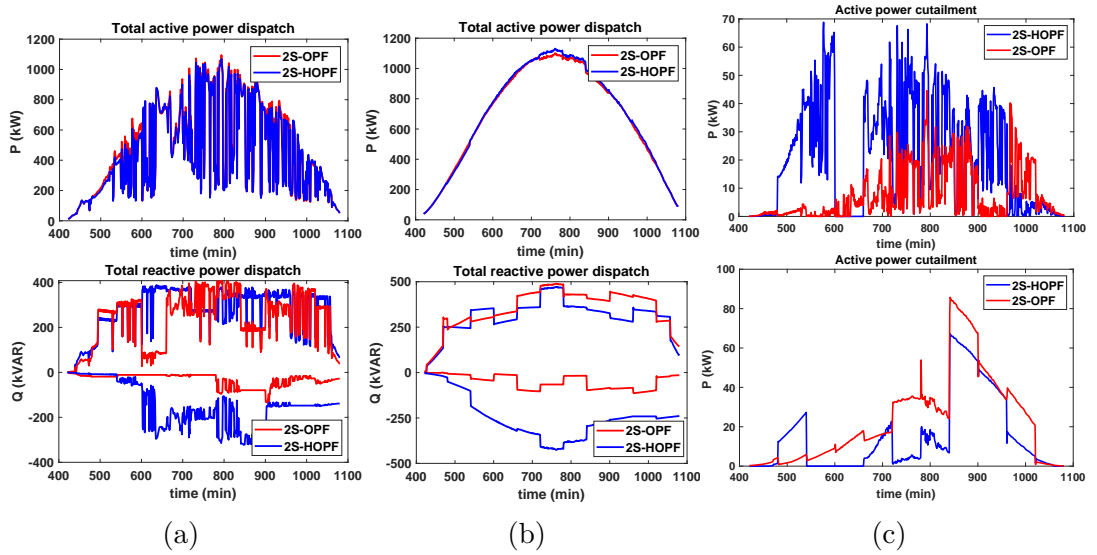


Figure 4.12: (a) P-Q dispatch cloudy day (b) P-Q dispatch clear day (c) P-curtailment (cloudy and clear day)

The use of the Volt-VAR (P-priority) by both algorithms allows the SIs to curtail the active power generation for effective voltage regulation. Also, both algorithms inject/absorb their optimal reactive power based on the SI modes and setting on the cloudy and clear days. From the reactive power dispatch plot (Figs. 4.12a and 4.12b), the 2S-OPF dispatches on the average 104.12 kVAR/min on the cloudy day and 136.77 kVAR/min on the clear day while the 2S-HOPF dispatches on the average 140.14 kVAR/min on the cloudy day and 206.51 kVAR/min on the clear



day. Since the 2S-HOPF places the highest hierarchy of operation on the SI, more reactive power is either absorbed/injected to control the feeder voltage compared to that of 2S-OPF.

### Voltage profile analysis

The voltage profile of two of the ten integrated PVs ( $PV_1$  and  $PV_2$ ) with both proposed algorithms on a cloudy and clear day is as shown in Fig. 4.13 and 4.14 respectively.

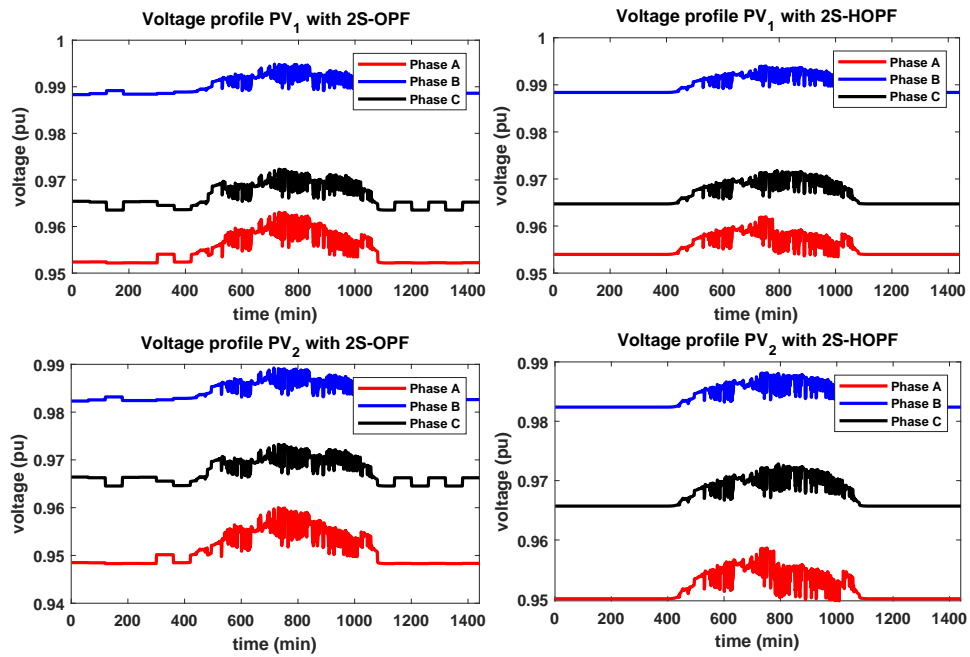


Figure 4.13: Voltage Profiles of  $PV_1$  and  $PV_2$  on a cloudy day.

The voltage profiles across the PVs shows that both algorithms are able to regulate the nodal voltage at the POI within the standard 0.95 -1.05 pu. As seen from the figure, the 2S-HOPF algorithm provides a better regulated voltage profile compared to that of the 2S-OPF. The hourly sum of the voltage deviation (objective function) for both algorithms on cloudy and clear day is as shown in Fig. 4.15 and 4.15b respectively.

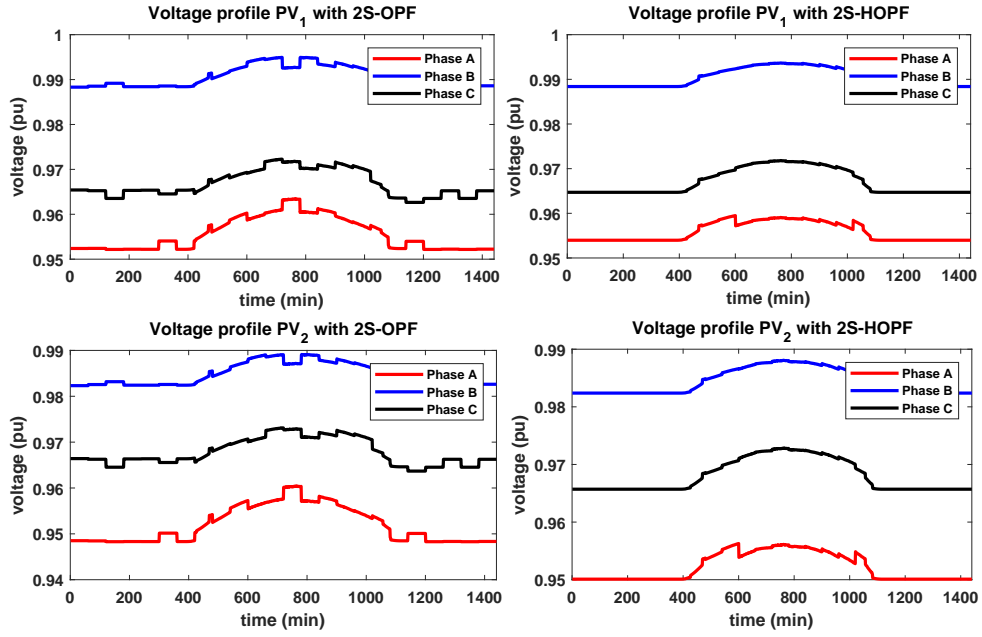


Figure 4.14: Voltage Profiles of  $PV_1$  and  $PV_2$  on a clear day day.

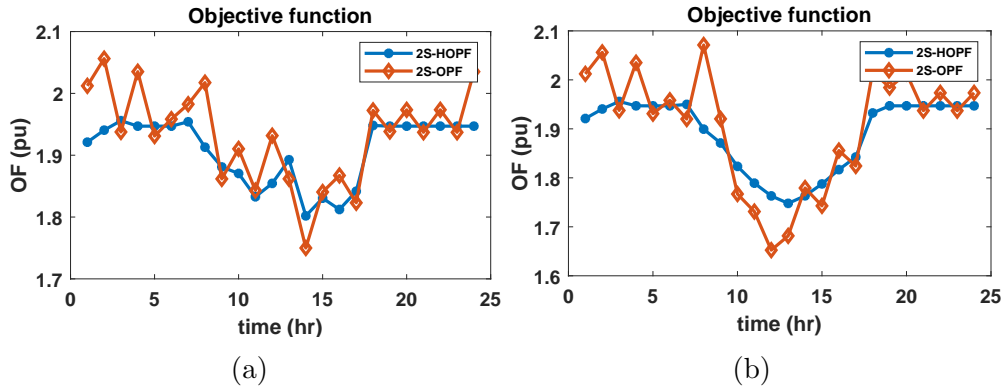


Figure 4.15: Total voltage deviation (a) Cloudy day (b) Clear day.

### 4.3 Heuristic-Based Optimization Algorithm

The proposed algorithm optimizes the bus voltage profile to the 0.95 pu boundary to take some advantage of CVR, minimize the overall system losses as well as uses the least amount of reactive power from the capacitor banks. The losses considered in this here are purely technical losses such as feeder losses, transformer load and no-load losses and capacitor bank losses. Some non-technical losses could include data theft (in case of smart grid network) and power theft, loses due to breakdown

of malfunction of devices in the distribution network. The proposed algorithm is as shown in Fig. 4.16. The algorithm begins by setting the initial OPF time series hour  $T = 1$ . An initial population of the

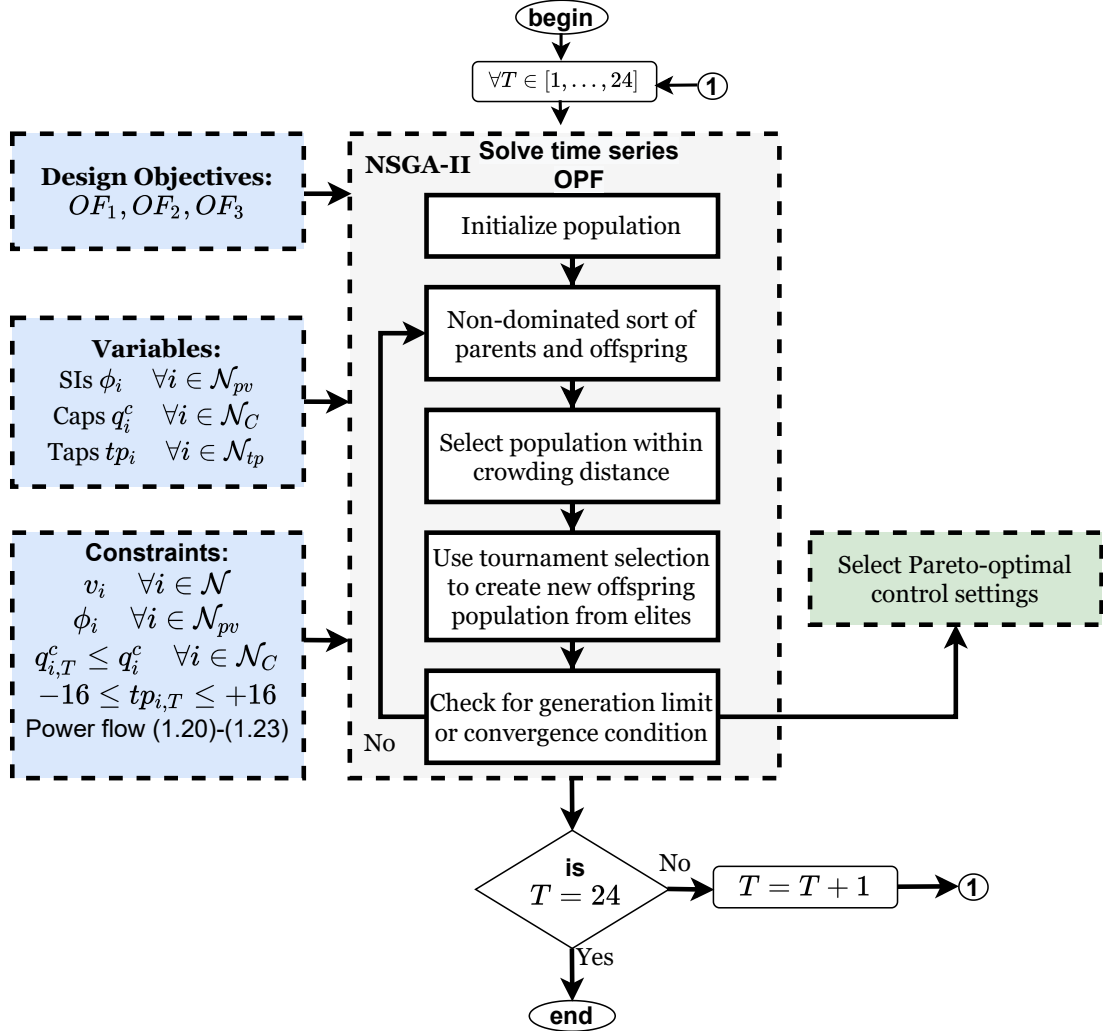


Figure 4.16: Proposed Heuristic-based optimization algorithm

### 4.3.1 Multi-Objective Optimization Formulation

#### Objective Function 1

The first objective of this work is to flatten the voltage profile of each feeder as much as possible close to the lower 0.95 pu threshold. This allows for the least

amount of power consumption in the network which is basically the concept of CVR. Many load types has their power consumption reduced with a reduction in their terminal voltages. This Objective Function (OF) was formulated as equation 4.27 similar to the expression derived by [197]

$$OF_1 = \min \sum_{i=1}^{\mathcal{N}} \left| \left( (v_i^{min} - v_{i,T}) + |\gamma v_{i,T} - v_i^{max}| \right) \right| \quad (4.27)$$

$\gamma$  is the CVR weighting factor that was chosen to make  $v_{j,t}$  close to  $v_j^{min}$  as much as possible.

### Objective Function 2

The second objective of the proposed method is to minimize the losses on each feeder within the time of 24 hour period of simulation. The load flow is solved on hourly load curve basis with a one-hour resolution PV data with the objective of minimizing the total system losses within these intervals.

$$S_{loss} = \sqrt{P_{loss}^2 + Q_{loss}^2} \quad (4.28)$$

$$OF_2 = \min (S_{loss})$$

### Objective Function 3

The third objective of this work is to minimize the total amount of reactive power injected by the two capacitor banks connected to buses 844 and 848.

$$OF_3 = \min \sum_{i=1}^{\mathcal{N}_C} q_i^c \quad (4.29)$$

## 4.3.2 Constraints Formulation

Bus voltage constrains should be within the ANSI C84.1.

$$v_i^{max} \geq v_{i,T} \geq v_i^{min} \quad (4.30)$$

$$1.05pu \geq v_{i,T} \geq 0.95pu$$

Capacitor bank VAR and switching constrains is given as equation 4.31. The maximum reactive power injection by these capacitors are 300 kVAR and 450 kVAR according to the values in the feeder parameters.

$$|q_{i,T}^c| \leq |q_i^c|; \quad \forall i \in \mathcal{N}_C \quad (4.31)$$

Considering a voltage regulator with 32 tap steps, the constraints for the tap setting is given as

$$-16 \leq tp_{i,T} \leq +16; \quad \forall i \in \mathcal{N}_{tp} \quad (4.32)$$

The power factors of the six PV systems where set as variable in the optimization algorithm to get the optimal values of the PV power factors.

$$0.8 \leq \phi_{i,T} \leq 1; \quad \forall i \in \mathcal{N}_{pv} \quad (4.33)$$

The distribution grid is modelled and set as part of the optimization constraints using the power flow equations in (4.20)-(4.23) [193].

### 4.3.3 Test Feeder and Simulation

The test feeder is a IEEE 34 node test feeder with a nominal voltage of 24.9 kV as shown in figure 4.17. The feeder has two units of 3-phase voltage regulators places between line segments 814-850 and 852-832. The system has a 2.5MVA, 69 / 24.9 kV,  $\Delta - Y$  substation transformer and 0.5MVA, 24.9 / 4.16 kV, Y-Y transformer connected. There are two 3-phase shunt capacitors of 300 kVAR and 450 kVAR connected to nodes 844 and 848 respectively. 6 units of 300 kW solar PV panels were connected to nodes 822, 840, 846, 848, 864 and 890.

Table 4.4 shows the specifications of the PVs located on the network. The default PF used for the non-optimized solution was 0.8. This is to enable the inverter inject some fixed reactive power into the system. The total kVA rating of the the load in the system is 2058 kVA. With a total PV active power rating of 1800 kW, this constitute a PV penetration level of 87 % approximately using the

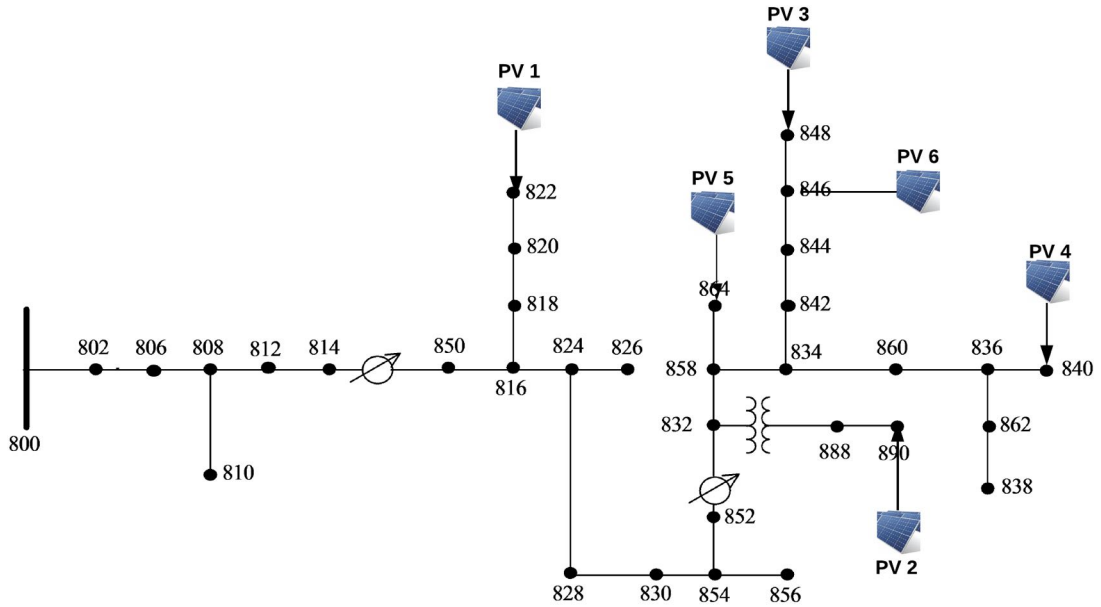


Figure 4.17: IEEE 34 node test feeder with PV locations

traditional method of PV penetration estimation which give the amount of PV penetration as the ratio of the PV generation to the maximum load on the feeder.

Table 4.4: PV Specifications

PVs	Maximum Power (kW)	Inverter (kVA)	Phases	Default PF
PV1 and PV5	300	400	1	0.8
PV2, PV3, PV4 and PV6	300	400	3	0.8

#### 4.3.4 Simulation and Results

The simulation of the test feeder was done with OpenDSS software with the optimization done with MATLAB software. The time series analysis was done with a 24-hour duration. The PV irradiance was of 1-hour resolution with peak generation at 13<sup>th</sup> hour of the day. The nodes of interest were the ones where the PVs were connected. The optimization was done on a hourly bases. Figures 4.18a-

4.18b show the single phase voltage profile of buses 822 and 864 while figures 4.19-4.22 show the 3-phase voltage on buses 840, 846, 848 and 890.

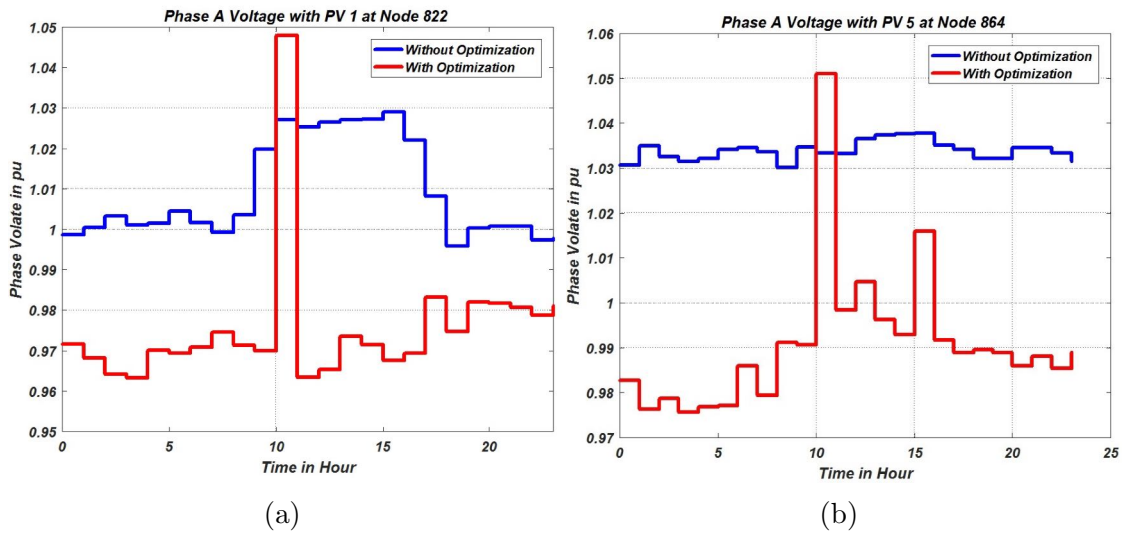


Figure 4.18: (a) Voltage Profile of (a) Node 822 (b) Node 864

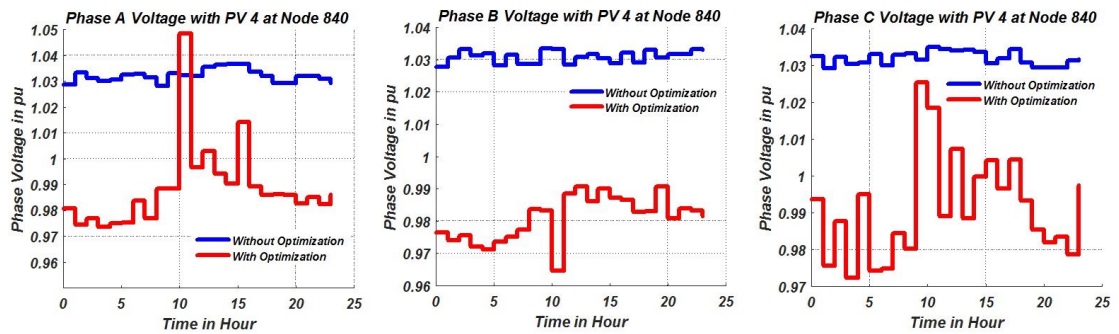


Figure 4.19: Voltage Profile of Node 840

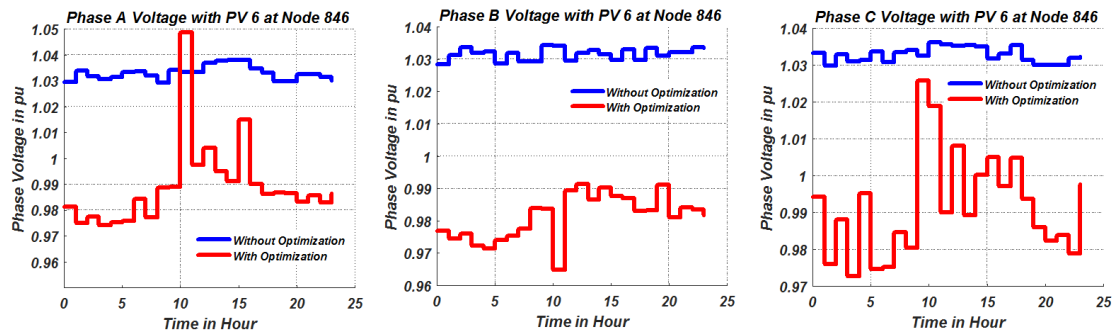


Figure 4.20: Voltage Profile of Node 846

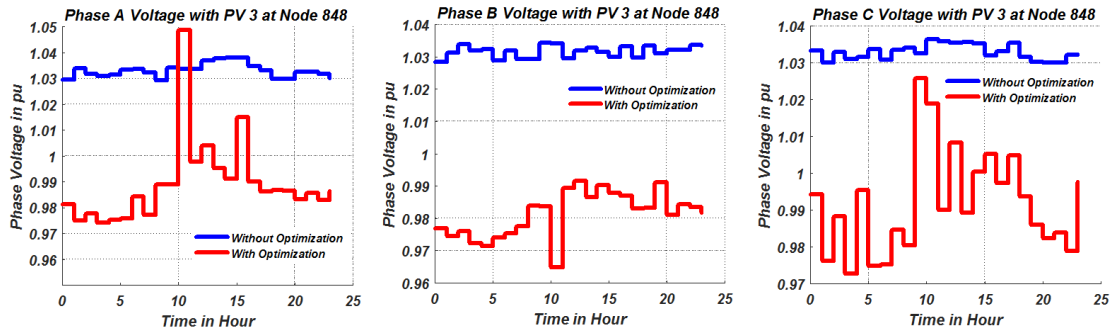


Figure 4.21: Voltage Profile of Node 848

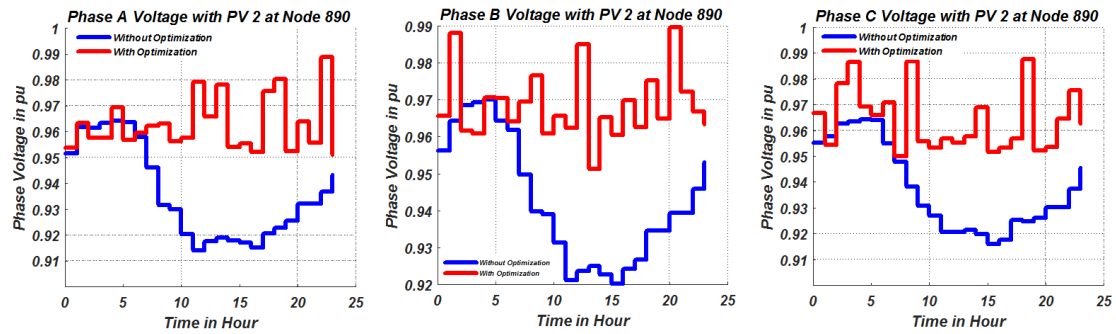


Figure 4.22: Voltage Profile of Node 890

The voltage profiles on these nodes showed significant reduction in the values in the terminal voltages without any violations. The voltage on node 890 was below the ANSI C84.1 voltage threshold of 0.95 without optimization. After optimization, the voltage was increased beyond the 0.95 pu threshold. The bar charts in figure 4.23 shows the reactive power injection on nodes 844 and 848 by the capacitor banks. The optimized values of the kVAR injection showed a significant reduction compared to the simulation without optimization. The plots of the losses in each hour of simulation is as shown in figure 4.24.

The plots showed a consistent reduction in the system apparent losses. The active power losses was reduced in all the hours except the 14<sup>th</sup>, 17<sup>th</sup> and the 23<sup>rd</sup> hours. This obviously was due to need to keep the voltage within the required threshold. The values shown in table 4.6 are the voltages (both the optimal and the non-optimized ) when there is maximum generation from the PV system at the 13<sup>th</sup> hour of simulation. Table 4.5 contains the optimal values of the power factor



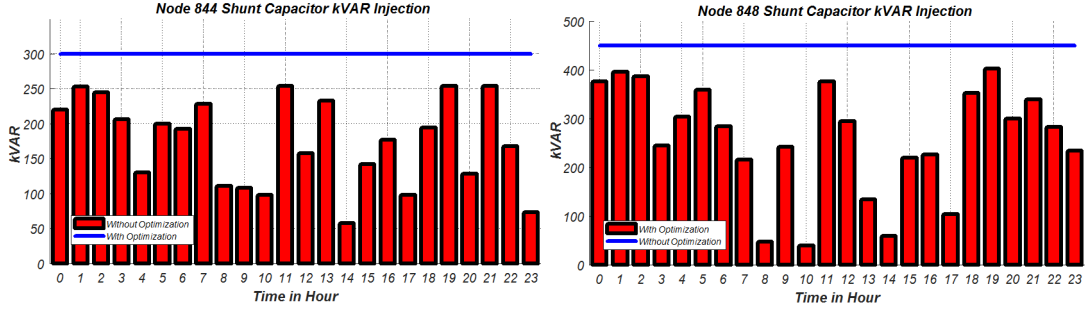


Figure 4.23: kVAR injection on nodes 844 and 848 by shunt capacitors

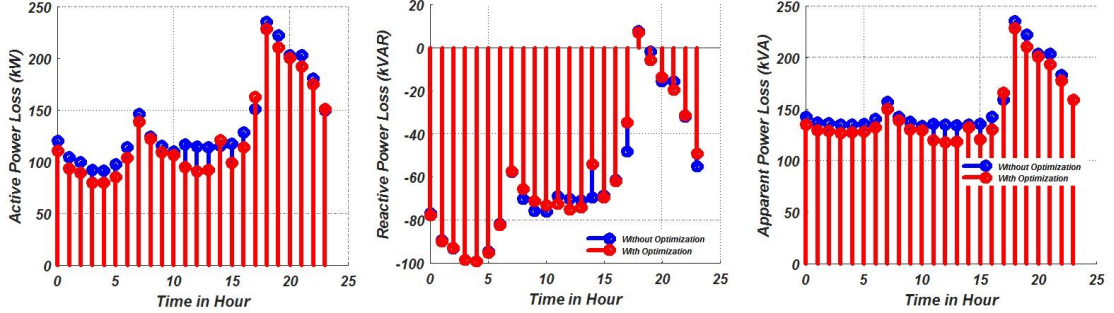


Figure 4.24: Hourly losses in the system

of the PV systems at the 13<sup>th</sup> of simulation. These values show some deviations from the 0.8 PF value set for the non-optimized solution. PV1 and PV6 had nearly unity PF which indicated almost no reactive power injection by these PVs while PV2 had the least PF, consequently with the maximum value of reactive power injection.

Table 4.5: PV Power Factors Optimized

	PV1	PV2	PV3	PV4	PV5	PV6
PF	1	0.82	0.917	0.97	0.947	0.99

#### 4.4 Summary

This chapter explored two approaches to solving optimal power flow problem in a distribution feeder using mathematical modelling and heuristic algorithm based approach. Using the mathematical modelling approach, we presented a new effort to explore a multi-mode and multi-droop settings of SIs (Volt-Watt, Volt VAR

Table 4.6: Node Voltages for the for all the nodes in the 13<sup>th</sup> hour of simulation

Bus	Distance (km)	Va (Normal)	Va (Optimal)	Vb (Normal)	Vb (Optimal)	Vc (Normal)	Vc (Optimal)
sourcebus	0	1.0500	1.0500	1.0500	1.0500	1.0500	1.0500
800	0	1.0500	1.0500	1.0500	1.0500	1.0500	1.0500
802	0.79	1.0503	1.0500	1.0486	1.0484	1.0496	1.0494
806	1.05	1.0505	1.0500	1.0478	1.0473	1.0493	1.0490
808	1.31	1.0543	1.0495	1.0326	1.0286	1.0453	1.0424
810	11.14	0	0	1.0324	1.0284	0	0
812	12.02	1.0584	1.0487	1.0159	1.0077	1.0404	1.0343
814	12.91	1.0615	1.0480	1.0028	0.9910	1.0367	1.0278
814r	22.57	1.0217	0.9563	1.0153	0.9973	1.0302	0.9828
850	31.63	1.0217	0.9563	1.0153	0.9973	1.0302	0.9828
816	31.63	1.0217	0.9563	1.0151	0.9970	1.0301	0.9827
818	31.63	1.0216	0.9563	0	0	0	0
824	31.73	1.0231	0.9557	1.0086	0.9894	1.0267	0.9785
820	32.25	1.0226	0.9605	0	0	0	0
822	33.28	1.0265	0.9654	0	0	0	0
826	34.84	0	0	1.0084	0.9893	0	0
828	39.59	1.0232	0.9557	1.0081	0.9889	1.0265	0.9781
830	46.92	1.0262	0.9548	0.9970	0.9756	1.0196	0.9694
854	49.02	1.0263	0.9548	0.9968	0.9753	1.0195	0.9692
832	51.11	1.0331	1.0023	1.0325	0.9937	1.0337	1.0082
858	35.30	1.0355	1.0037	1.0314	0.9921	1.0337	1.0078
834	35.76	1.0353	1.0029	1.0310	0.9909	1.0338	1.0071
842	34.97	1.0354	1.0029	1.0310	0.9909	1.0338	1.0071
836	35.09	1.0354	1.0028	1.0308	0.9907	1.0339	1.0072
840	38.21	1.0355	1.0029	1.0309	0.9908	1.0340	1.0073
844	41.32	1.0355	1.0029	1.0310	0.9908	1.0339	1.0071
846	41.48	1.0368	1.0040	1.0319	0.9915	1.0353	1.0082
848	52.71	1.0369	1.0040	1.0320	0.9915	1.0354	1.0083
856	53.46	0	0	0.9967	0.9752	0	0
852	54.21	1.0331	0.9546	0.9775	0.9520	1.0085	0.9546
852r	55.09	1.0331	1.0023	1.0325	0.9937	1.0338	1.0082
888	55.98	0.9975	0.9662	0.9971	0.9584	0.9997	0.9742
864	56.07	1.0366	1.0046	0	0	0	0
860	57.42	1.0352	1.0027	1.0308	0.9907	1.0337	1.0070
862	57.55	1.0354	1.0028	1.0308	0.9907	1.0339	1.0072
838	57.68	0	0	1.0306	0.9905	0	0
890	56.27	0.9175	0.8858	0.9237	0.8850	0.9207	0.8953

P-priority, Volt VAR Q-priority, constant power factor (leading and lagging) as part of a single OPF formulation, on the same feeder for effective voltage control and optimization. We also proposed a two-stage OPF and two-stage HOPF which allow the SI mode, SI settings, OLTC/VR tap position and Caps status to be optimally determined on hourly basis while the optimal active and reactive power is dispatched on one-minute basis. The 2S-HOPF gives the highest priority of voltage control to the SI. The proposed formulation and algorithms are tested on the

standard IEEE 123 test feeder. The results show the effectiveness and feasibility of proposed algorithms. The chapter also presented a multi-objective optimization technique for volt-var control with high PV penetration on the distribution feeder using genetic algorithm. This optimization was solved to minimize the distribution system losses while keeping the voltage of the nodes close to the lower threshold of the ANSI C84.1 standard. This was done to take the benefit of CVR into effect. The results show the effectiveness of the technique in the use of CVR and also in minimizing the system losses. The algorithm also was able to effectively minimize the amount of reactive power dispatched by the capacitor banks.

CHAPTER 5

**MULTIPHYSICS AND MULTIOBJECTIVE DESIGN  
OPTIMIZATION OF MEDIUM AND HIGH FREQUENCY  
TRANSFORMER FOR SOLID-STATE TRANSFORMER  
APPLICATIONS**

This chapter introduces several existing H/MFT optimization frameworks and presents a novel multiphysics-based design optimization algorithm for SSTs-H/MFT. According to the DOE Energy Conservation Standards (ECS) [198], for dry-type distribution transformers (with input voltage  $\leq 34.5kV$ , output voltage  $\leq 600V$ , power rating of  $15kVA$  -  $2500kVA$ , and frequency of  $60Hz$ ), the efficiency of three-phase liquid-Immersed distribution transformers, should be between 98.65% for  $15kVA$  to 99.53% for  $1000kVA$ . Though the traditional low frequency ( $50/60Hz$ ) transformers are very reliable, efficient, rugged, provides good galvanic isolation, and cost effective, they are relatively large in size, and have some control limitations. With the use of HFT for galvanic isolation, the size of SSTs can be considerably reduced. Compared to the traditional low frequency transformers, SSTs are capable of active and reactive power flow control and compensation, bi-directional power flow, availability of DC link that allows interconnection with photovoltaic systems and energy storage, harmonic mitigation and cancellation, and voltage sag/swell mitigation. However, some of the major concerns with large deployments of SSTs include their relatively lower efficiency (due to high switching loss from power electronic converters as well as power loss of the HFT) compared to the traditional low frequency transformers, ruggedness, reliability, and cost. In order to achieve a compact, highly efficient and cost effective SST, an optimized design of its HFT becomes very imperative. HFTs usually constitutes bulk of the weight of the SSTs as well as determines its overall power transfer efficiency. The cost of the core (usually Amorphous, Nanocrystalline or Ferrites), and winding

(usually litz wire to reduce skin effect) of the HFT makes its cost optimization also of importance.

As an emerging technology, several optimization approaches and iterative design techniques have been proposed for HFTs. The authors of [199] present a HFT design technique for dual active bridge (DAB) converters that addresses the isolation requirements and the desired leakage inductance. The variables of the proposed optimization algorithm are the geometrical and electrical parameters (which include the number of stacked cores, current density, number of layers and turns of the winding, primary and secondary foil thickness). The proposed algorithm only considers the power density as its objective with the leakage inductance, efficiency, isolation and thermal limits set as its design requirements. The proposed technique is not robust enough to determine the best power density since the core dimensions are not set as variables, also the cost factor of the HFT is not considered in the optimization.

An analytical procedure that optimally selects the flux density of the HFT in order to minimize the power loss, selects the least core volume and the winding optimal current density, in order to maximize the transformer's power density is presented in [200]. Mogorovic et al in [201] presents an analytical method for estimating HFT's leakage inductance. The proposed method takes into consideration the effects of the geometry of the HFT and frequency variation in order to achieve a target leakage inductance. The proposed analytical method, though was quite accurate compared to the Dowell's model, but it still falls short of the accuracy of an FEA-based model. The same authors in [202] present a HFT optimization algorithm called the "brute force HFT design optimization algorithm". The proposed algorithm involves two stages. First, all possible values of the variables are set freely in order to see all the mathematically possible designs. The next stage of the optimization algorithm involves analyzing the filtered designs against practical core sizes and wires, and selecting the optimized based on practical values of

materials available off-the-shelf. The major drawbacks of this approach include: its computational complexity and the absence of flexibility in core size in the second stage of the algorithm. Optimal area product ( $A_p$ ) selection is commonly used as a basis for the design optimization of HFTs [12, 13, 203, 204]. References [12, 13, 203] present an  $A_p$  estimation method based on the desired leakage inductance, maximum flux density of the selected core type and the allowed short circuit current. The core dimensions and winding parameters are analytically determined afterwards. In summary, after a careful review of existing literature, some of the major drawbacks in proposed optimization approaches include: the use of analytical equations to determine the electromagnetic, thermal performance of HFTs which is less accurate, absence of multiphysics performance analysis of the optimized HFT and neglect of its cost as part of the optimization objectives.

In order to address these gaps (as an extension of the authors work in [205]), this chapter proposes a multi-objective and multiphysics-based design optimization of HFTs. The core dimensions and optimal number of turns are set as design variables in order to minimize the power loss, maximize its power density and minimize its cost. To make the proposed optimization algorithm practically implementable for validation purposes, the relationship between off-the-shelf standard core dimension and sizes are developed and set as constraints. This also allows the optimization to be computationally efficient. The multiphysics analysis (based on time-harmonic electromagnetic, thermal and fluid models of the HFT) of each sub-optimal solution is used to accurately capture its performance based on FEA. This technique allows for accurate physics parameters measurement of the HFT and ensures a more accurate and effective design compared to existing methods in literature which uses analytical methods without any coupling within these physics models. The FEA results are fed back to the optimization engine to determine the fitness of the variables based on the set objectives. The optimization results and the hardware implementation clearly shows the effectiveness of this approach.

## 5.1 Proposed Multi-Objective Optimization Algorithm and Theoretical Formulation

Design optimization of HFTs involves different trade-offs depending on the desired objectives and its area of application. At high frequencies, the core loss in HFTs and the switching loss in the power electronic converters becomes significant. Therefore minimizing the total power loss of the HFT becomes a crucial design objective. The design optimization objectives, variables and constraints are as formulated in sections 5.1.1 and 5.1.2 respectively.

### 5.1.1 Design Optimization Objectives Formulation

The three objectives considered for the proposed optimization are the power density ( $P_d$ ), cost ( $C_t$ ) and the total transformer power loss ( $P_t$ ). These objectives are formulated as expressed in (5.1), (5.2) and (5.16) respectively . (with  $d_c$  = core width)

$$P_d = \frac{P_o}{V_c + V_w + V_{Al}} \quad (5.1)$$

The volume of the core  $V_c = l_m A_c$  for a single set of C-cores and  $V_c = h_c l_c t_c - 2(W_h W_w t_c)$  for a double set of C-core (shell type HFT). The winding volume  $V_w = MLT \times A_w$ . Where  $l_m$ ,  $A_c$ ,  $h_c$ ,  $l_c$ ,  $d_c$ ,  $t_c$ ,  $W_h$ ,  $W_w$ ,  $A_w$  are the core mean length, area, height, length, width, thickness, window height, width and cross-sectional area respectively. MLT is the mean length per turn.  $V_{Al}$  is the volume of aluminium used to bind the cores together. The cost ( $C_t$ ) can be estimated as expressed in (5.2)

$$C_t = MLT \times (N_p + N_s)C_w + V_c C_c + C_{Al} V_{Al} \quad (5.2)$$

where  $N_p$ ,  $N_s$  are the primary and secondary number of windings,  $C_w$ ,  $C_c$ ,  $C_{Al}$  are the cost coefficients of the Litz wire, amorphous core and aluminium bars.

The core losses becomes significant at high frequencies depending on the type and volume of core material used. The improved generalized Steinmetz equation (iGSE) can be used to estimate the core loss in the HFT as expressed in (5.3) [205].

$$P_{loss}^{core} = \frac{1}{T} \int_0^T k_i \left| \frac{dB(t)}{dt} \right|^\alpha (\Delta B)^{\beta-\alpha} dt \quad (5.3)$$

where  $k_i = \frac{K}{(2\pi)^{\alpha-1} \int_0^{2\pi} |\cos\theta|^\alpha 2^{\beta-\alpha} d\theta}$ ,  $B$  is the flux density,  $T$  is the period, and  $\alpha, K, \beta$  are core parameters for loss calculations depending on the type of core used. Since the core power loss depends on the flux density and the operating frequency, the optimal flux density required to achieve a minimized power loss in the HFT can be obtained as expressed in (5.4) [200, 206].

$$B_{op} = \frac{(H_c k_a \Delta T_a)^{2/3}}{2^{2/3} [\rho_{cu} k_w k_u]^{1/12} [k_c K_c f_s^\alpha]^{7/12}} \left[ \frac{K_v f k_f k_u}{\sum VA} \right]^{1/16} \quad (5.4)$$

$$A_p = \left[ \frac{\sqrt{2} \sum VA}{K_v f_s B_{op} K_f K_t \sqrt{k_u \Delta T_a}} \right]^{8/7} \quad (5.5)$$

where  $K_t = \sqrt{\frac{H_c k_a}{\rho_{cu} k_w}}$ ,  $\sum VA = P_{out} (1 + \frac{1}{\eta})$ ,  $H_c$ , is the heat transfer coefficient,  $k_a$ ,  $k_c$ ,  $k_w$  are coefficients that depends on the core material used,  $\Delta T_a$  is the temperature change,  $k_f$ ,  $k_u$  are the core stacking and window utilization factors,  $K_v$  depends on the type of the voltage waveform applied to the HFT,  $\eta$  is the desired efficiency,  $\rho_{cu}$  is the resistivity of copper and  $\sum VA$  is the total  $VA$  rating.

The power loss in the winding of the HFT depends on its winding resistance and the rms value of current flowing through it. Considering the high frequency effects on the winding resistance, the value of the winding AC resistance can be computed using equation (5.12) [207, 208]:



$$\Gamma = -2.4128d_{cu}^2 + 1.5113d_{cu} + 0.3535 \quad (5.6)$$

$$d_{cu}^o = \sqrt{\frac{-b_1 + \sqrt{b_1^2 + 12\delta_s^4}}{2}} \quad (5.7)$$

$$b_1 = \frac{\pi^2\Gamma^2}{24} \left[ 16l^2 - 1 + \frac{24}{\pi^2} \right] d_{cu}^2 \quad (5.8)$$

$$\xi = 4 \times \sqrt[4]{\frac{3}{1 + \frac{\pi^2 n_s \Gamma}{24} (16l^2 - 1 + \frac{24}{\pi^2})}} \quad (5.9)$$

$$\Lambda_1(\xi) = 2\sqrt{2} \left\{ \frac{1}{\xi} + \frac{\xi^3}{3 \times 2^8} - \frac{\xi^5}{3 \times 2^{14}} \right\} \quad (5.10)$$

$$\Lambda_2(\xi) = \frac{1}{\sqrt{2}} \left\{ -\frac{\xi^3}{2^5} + \frac{\xi^7}{2^{12}} \right\} \quad (5.11)$$

$$R_{cuac} = \frac{\sqrt{2}\rho_{cu}N}{\pi\delta_s n_s d_{cu}^o} \left[ \Lambda_1(\xi) - \frac{\pi^2 n_s \Gamma}{24} (16l^2 - 1 + \frac{24}{\pi^2} \Lambda_2(\xi)) \right] \quad (5.12)$$

where  $d_{cu}^o$ ,  $l$ ,  $n_s$ ,  $\xi$ ,  $d_{cu}$ ,  $N$  are the optimal Litz wire strand diameter, number of layers of winding, packing factor, strands in the each Litz wire conductor, diameter of the copper conductor, and  $N = N_s$  or  $N_p$ .

In order to minimize the proximity and winding loss, the ratio of the ac/dc resistance of the winding should be around 2 according to [206, 208, 209]. This ratio can be estimated using (5.13)

$$\frac{R_{cuac}}{R_{cudc}} = \left\{ 1 + \frac{[r_o/\delta_s]^4}{48 + 0.8[r_o/\delta_s]^4} \right\} \quad (5.13)$$

where  $r_o$ , is the round conductor radius in mm and the skin effect  $\delta_s$  at frequency  $f_s$  can be expressed as (5.14)

$$\delta_s(\text{for copper conductor}) = \frac{6.62}{\sqrt{f_s}} \quad (5.14)$$

The power loss in the primary and secondary winding can be estimated using equation (5.15).

$$P_{loss}^{cu} = i_{rms,p}^2 \times R_{cuac}^p + i_{rms,s}^2 \times R_{cuac}^s \quad (5.15)$$

where  $i_{rms,p}$  and  $i_{rms,s}$  are the primary and secondary rms currents, while  $R_{cuac}^p$  and  $R_{cuac}^s$  are primary and secondary winding ac resistance respectively

The total transformer power loss  $P_t$  can be expressed as (5.16)

$$P_t = P_{winding} + P_{loss}^{core} \quad (5.16)$$

In order to achieve adequate isolation between the primary and the secondary winding, the minimum isolation distance  $d_{i,min}$  can be expressed as (5.17) [199]

$$d_{i,min} = \frac{V_{iso}}{k_{iso}E_{ins}} \quad (5.17)$$

where  $V_{iso}$ ,  $E_{ins}$ ,  $k_{iso}$  (for air as dielectric), are the isolation voltage ( $3kV$ ), dielectric strength of material for insulation ( $3kV/mm$ ) and the margin for safety factor respectively (0.4).

The multi-objective optimization problem can be expressed as (5.18)

$$(l_c, h_c, t_c, d_c, N_p, N_s) = \min(P_t, C_t, -P_d) \quad (5.18)$$

### 5.1.2 Design Optimization Variables and Constraints formulation

The search space for the optimal values for the transformer core parameters and winding are constrained based on the maximum feasible sizes of the cores and the limitations of the power electronic converter used.

## Optimization constraints formulation

Based on the core size, the optimization is carried out to achieve a minimum number of transformer turns  $N_{s,p}$ , which will ensure a reasonable value of leakage inductance without any severe impact on the transformer's efficiency. The maximum allowable temperature rise and the saturation flux density of the cores are used to set the thermal and electromagnetic constraints during the optimization. Also, in order to achieve realistic values for practical implementation of the core sizes based on the data sheet of the AMCC cores available off-the-shelf [210], the core sizes/dimensions ( $h_c, l_c, t_c, d_c$ ) are approximately constrained (as expressed in (5.19)).

$$\begin{cases} h_c \geq \frac{5}{2}d_c, h_c \leq \frac{d_c}{2} + t_c + \frac{l_c}{2}, l_c \geq h_c \\ l_c \geq 3d_c, \frac{l_c}{2} \leq 2t_c, h_c \geq 2 * t_c \\ h_c \leq h_{max}, l_c \leq l_{max}, t_c \leq t_{max}, d_c \leq d_{max} \\ N_{min} \leq N_{s,p} \leq N_{max}, B_{op} \leq B_{sat}, T \leq T_{max} \end{cases} \quad (5.19)$$

## Power Electronic Converter Constraints

The dual active bridge (DAB) (as shown in Fig. 5.1), LLC resonant converter is popularly used for SST applications. This is due to its wide voltage regulation and ability to achieve soft switching over a wide range of loading. Figure 5.2 shows the equivalent circuit for a typical LLC-based DAB converter. Its transfer function (which represents its voltage gain) can be expressed as (5.20).

$$\begin{aligned} H(j\omega) &= \frac{V_o(j\omega)}{V_{in}(j\omega)} \\ &= \frac{-\omega^2 L_m R_{ac}^{eq} C_r}{j\omega \left[ 1 + \frac{-\omega^2 [L'_1 C_r (n^2 L_2 + L_m) + n^2 L_m L_2 C_r]}{n^2 L_2 + L_m} \right] \times} \\ &\quad (L_m + n^2 L_2) + R_{ac}^{eq} \left[ 1 - \omega^2 (L'_1 + L_m) \right] \end{aligned} \quad (5.20)$$

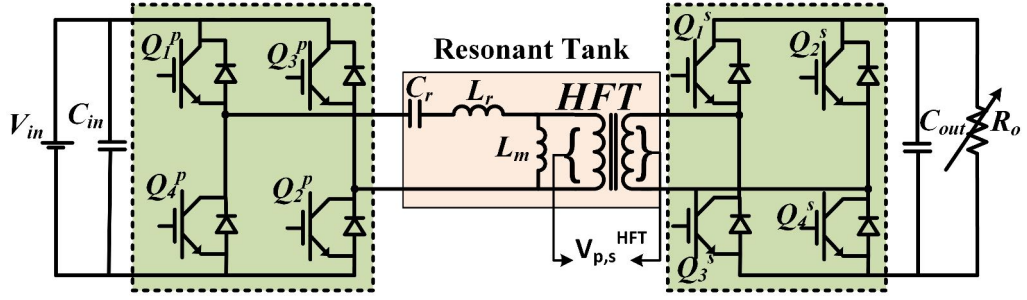


Figure 5.1: Schematic of a resonant LLC DAB Converter

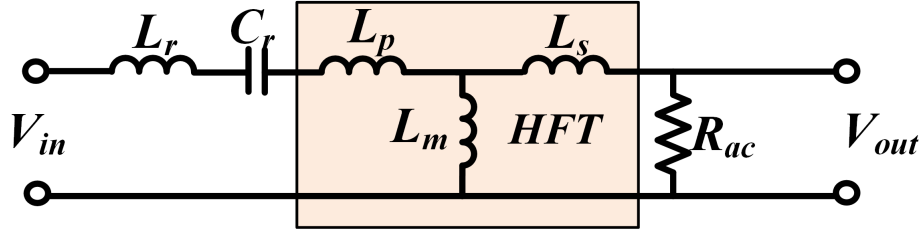


Figure 5.2: An LLC DAB converter equivalent circuit

where

$$L'_1 = L_p + L_r \quad (5.21)$$

$L_r$ , is the external inductance in series with the resonant capacitor  $C_r$ . The parameters  $L_m, L_p, L_s, L_k$  are magnetizing, primary, secondary, leakage (referred to the primary) inductances of the HFT can be estimated from the finite element analysis (FEA) solutions as expressed in (5.22)-(5.25) [211–213]. These values are crucial to achieving the zero current and voltage switching as well as the maximum power transfer capacity of the SST with DAB topology.

$$L_p = \int_{S_p} AJdS \Big|_{I_p=1A, I_s=0} \quad (5.22)$$

$$L_s = \int_{S_s} AJdS \Big|_{I_s=1A, I_p=0} \quad (5.23)$$

$$L_m = \int_{S_s+S_p} AJdS \Big|_{I_s=1A, I_p=1A} - L_p - L_s \quad (5.24)$$

$$L_k = \frac{W}{I_p^2} \quad (5.25)$$

where,

$$W = \frac{1}{2} \int_V A \cdot J dv \quad (5.26)$$

The quality factor of the HFT winding can be expressed as (5.27)

$$Q_{HFT} = \frac{2\pi f_s L_k}{R_{cuac}} \quad (5.27)$$

while the quality factor of the loaded converter can be expressed as (5.28).

$$Q_r = \frac{\sqrt{\frac{L_{res}}{C_r}}}{R_{ac}} \quad (5.28)$$

where

$$L_{res} = L'_1 + L_m // n^2 L_s \quad (5.29)$$

The plot of the converter gain against its switching frequency is as shown in Fig. 5.3 at different values of  $Q_r$ . From (5.28), the value of  $Q_r$  is small at light loads and large during heavy loading conditions [214]. To achieve soft switching (zero voltage/current switching) of the converter switches at a good value of  $H(j\omega)$ ,  $Q_r$  is typically chosen close to the maximum loading condition [215]. The value of  $Q_r$  can be constrained as expressed in (5.30).

$$0.5 \leq Q_r \leq 1 \quad (5.30)$$

The proposed HFT design optimization algorithm is as shown in Fig. 5.4. The input to the algorithm include design specifications, converter, core electrical, thermal, electromagnetic constraints, the design variables and the optimization objectives of the HFT. An initial population is generated based on the defined variables which builds the geometry of the HFT. The FEA time-harmonic electromagnetic solver is used to compute the electromagnetic parameters (including the losses in the HFT). The results of the time-harmonic electromagnetic solution and

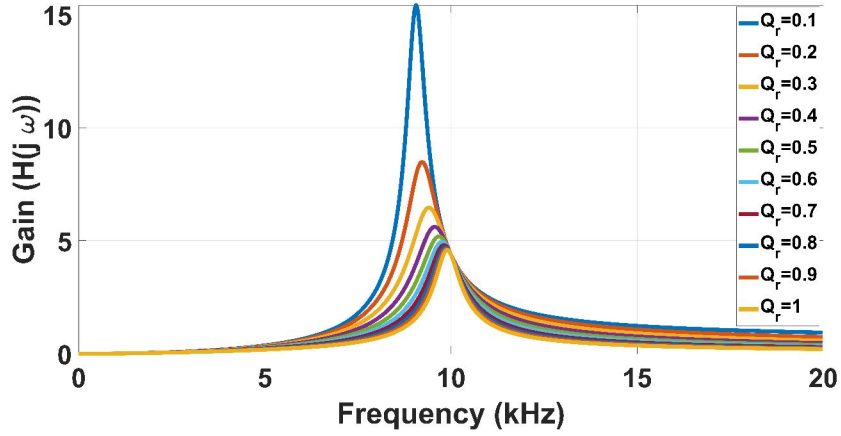


Figure 5.3: Gain curves of the resonant converter with  $L_m/L'_1 = 5$

the geometry serves as the input to the thermal and fluid models. The flux density and temperature distribution of the HFT is compared with the set maximum values. The thermal, electromagnetic and geometry parameters are used to evaluate the fitness functions based on the set objectives. New set of HFT variables are generated until the stop criteria is met. The POS are saved as valid designs for subsequent experimental validation.

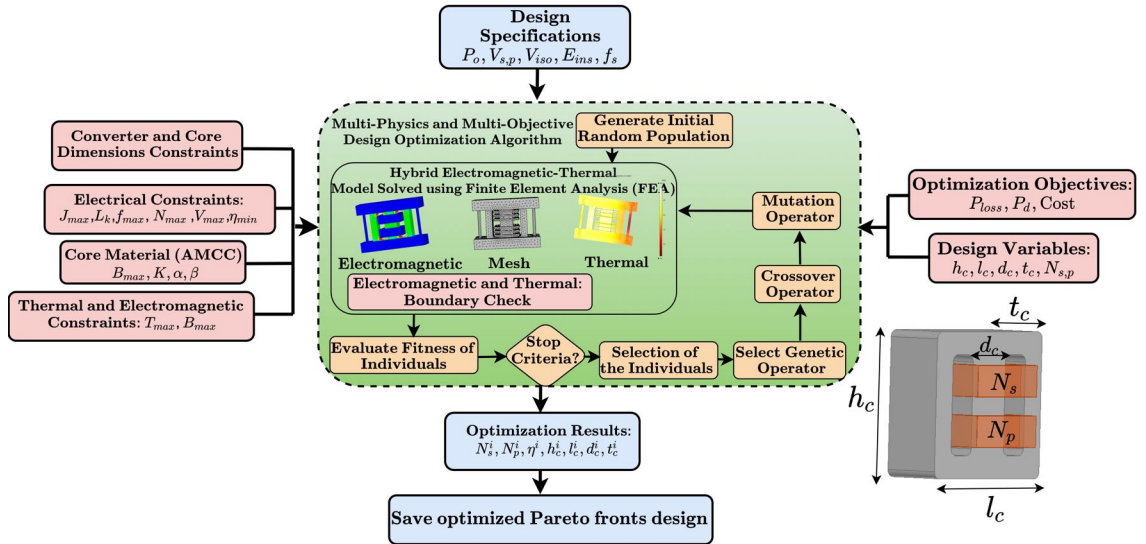


Figure 5.4: The proposed multiphysics-based, multi-objective optimization algorithm

## 5.2 Steady State Multiphysics formulation

HFTs can be modeled as a combination of three physics domains, which include the thermal, fluid and the electromagnetic models. Each physics model is as presented in the following subsections:

### 5.2.1 Electromagnetic Field Physics Model

Typically, electromagnetic field dynamics are faster than that of the fluid and thermal models [216]. This implies that the use of a model based on time-harmonic electromagnetic analysis is adequate to capture the dynamics of the electromagnetic field simulations. The time-harmonic electromagnetic model can be formulated using (5.31) [217, 218] .

$$\nabla \times (v(\nabla \times A)) = J_e - j\omega\sigma A \quad (5.31)$$

where  $A$ ,  $v$ ,  $J_e$ ,  $\sigma$ ,  $\omega$  are the magnetic vector potential, magnetic reluctivity, eddy current density, material electrical conductivity, and frequency in *rad/s* respectively.

### 5.2.2 Thermal Physics Model

The heat transfer and its interaction between the winding, aluminum coupling and the fluid environment of the HFT can be modeled as expressed in (5.32). The source of heat ( $Q$ ) in the HFT includes the heat  $i^2R$  losses in the winding and the eddy current loss in the amorphous cores [219, 220].

$$\rho_v C_p \frac{\partial T_a}{\partial t} - \nabla \cdot (k \nabla T_a) = Q \quad (5.32)$$

$\rho_v$ ,  $C_p$ ,  $k$ ,  $T_a$  are the volume density, specific heat capacity, thermal conductivity and ambient temperature respectively. Natural air cooling is assumed for the

HFT, and the multiphysics model for heat transfer in the fluid (air) is as expressed in (5.33) [219].

$$\rho_v C_p \frac{\partial T_a}{\partial t} + \rho_v C_p \mathbf{u} \cdot \nabla T_a - \nabla \cdot (k \nabla T) = Q + Q_p \quad (5.33)$$

where  $Q_p$ ,  $u$ , are the point heat source and velocity vector respectively.

### 5.2.3 Fluid Dynamics Model

In order to analyse the interaction between the fluid dynamics and the thermal physics model, a coupling between these two physics is required. This allows the flow of the air around the core and winding of the HFT and their interaction with the heat generated by the winding and the core to be properly analysed. The natural air cooling fluid dynamics model is as expressed in (5.34) and (5.35) [221].

$$\rho_f \frac{\partial \mathbf{u}_f}{\partial t} + \rho_f \mathbf{u}_f \cdot (\nabla \mathbf{u}_f) - \nabla \cdot \left[ -p \mathbf{I} + \mu (\nabla \mathbf{u}_f + (\nabla \mathbf{u}_f)^T) - \frac{2}{3} \mu (\nabla \cdot \mathbf{u}_f) \mathbf{I} \right] = \mathbf{F} \quad (5.34)$$

$$\frac{\partial \rho_f}{\partial t} = -\nabla \cdot (\rho_f \mathbf{u}_f) \quad (5.35)$$

where  $\rho_f$ ,  $\mathbf{u}_f$ ,  $\mathbf{F}$ ,  $p$ , are fluid density, velocity, volume force and pressure respectively.

## 5.3 Simulation Results and Analysis

A design optimization of a  $20kW$ ,  $10kHz$  HFT is presented as a case study. The multiphysics simulation and optimization is done using FEA software coupled with MATLAB. The detailed technical specification the HFT is as presented in Table 5.1. The AMCC cores were selected due to its high saturation flux density ( $1.56T$ ), reasonable core loss (in  $W/cm^3$ ) and relatively lower cost compared to the nano-



crystalline cores used for high frequency power converter magnetics applications. The cost factors for the cost optimization is presented in Table 5.2.

Table 5.1: HFT Design Specifications

Description	Value
$P_{out}$	20kW
$f_s$	10kHz
Core Type	Shell
$V_{p,s}$	208/208V
Rated Current	96.2A

Table 5.2: Cost coefficients used in optimization

Coefficient	Description	Value
$C_w$	Cost of Litz wire per unit length (\$/m)	2.3
$C_c$	Cost of Amorphous core per unit volume (\$/cm <sup>3</sup> )	0.73
$C_{Al}$	Cost of aluminum per unit volume (\$/cm <sup>3</sup> )	0.1

The results of the proposed optimization algorithm as shown in Fig 5.4 is as presented in Table 5.3. The simulation result gave 18 POS with different sizes of the cores, their efficiency values, power densities, total costs, and number of turns. The values of the primary, secondary and leakage inductances are also computed from the FEA solutions. The 3D plot of the POS based on the defined objective functions is as shown in Fig. 5.5.

The simulation results clearly show the different trade-offs in selecting different core sizes and optimal number of turns for the primary and secondary winding. Based on the objectives of most importance and the area of application of the HFT, the appropriate selection of the core size and number of turns can be made. The core sizes with higher power densities tend to be more efficient due to the decrease in core mass and volume but suffers from low values leakage inductance which is crucial to achieving wide ZVS/ZCS range in DAB converters. The leakage inductance in DAB converters serves as the main energy transfer element from the primary to the secondary converter which has to be carefully selected during the

Table 5.3: POS Results for a 20kW, 10kHz HFT for SST Application

POS	Design Variables (cm)			Objective Functions			Inductance			Turns		
	$h_c$	$l_c$	$t_c$	$d_c$	$C_t(\$)$	$P_d(W/cm^3)$	$P_t(W)$	$\eta(\%)$	$L_k(mH)$		$L_{p,s}(mH)$	$L_m(mH)$
1	12.90	13.58	3.44	3.31	304.60	7.62	99.17	99.51	0.0125	0.2579	0.2455	6
2	12.16	13.63	3.44	3.31	292.93	8.13	102.10	99.49	0.0115	0.2711	0.2596	7
3	11.39	14.11	3.54	3.30	292.65	8.00	107.69	99.46	0.0103	0.2892	0.2789	7
4	11.75	14.17	3.96	3.30	331.70	7.28	115.41	99.43	0.0110	0.3137	0.3027	7
5	13.27	13.76	4.75	3.38	428.96	6.38	128.06	99.36	0.0140	0.3548	0.3407	6
6	12.75	15.13	3.98	3.29	369.35	5.58	140.72	99.30	0.0158	0.3876	0.3719	8
7	13.14	15.71	4.55	3.31	442.80	4.71	189.54	99.06	0.0215	0.5587	0.5372	8
8	13.02	16.53	4.44	3.31	447.47	4.26	222.94	98.90	0.0257	0.6760	0.6503	9
9	13.43	16.53	4.73	3.29	482.19	4.00	230.65	98.86	0.0271	0.7010	0.6739	9
10	13.34	17.67	4.70	3.31	501.98	3.48	270.50	98.67	0.0316	0.8387	0.8071	10
11	13.38	17.61	5.02	3.30	532.28	3.41	284.66	98.60	0.0324	0.8946	0.8622	10
12	13.32	17.56	5.41	3.29	565.11	3.35	301.52	98.51	0.0329	0.9625	0.9296	10
13	13.30	17.65	5.87	3.28	608.29	3.21	321.55	98.42	0.0334	1.0388	1.0054	10
14	13.38	17.57	6.32	3.28	652.43	3.13	341.41	98.32	0.0345	1.1178	1.0832	10
15	13.45	17.94	6.70	3.43	722.05	3.01	373.19	98.17	0.0351	1.2393	1.2042	11
16	13.41	17.75	6.26	3.27	657.55	3.06	391.74	98.08	0.0415	1.3276	1.2861	11
17	13.49	17.98	6.70	3.26	705.58	2.87	411.85	97.98	0.0422	1.4001	1.3579	11
18	13.46	17.79	6.63	3.30	699.31	2.98	413.56	97.97	0.0424	1.4148	1.3724	11
Analytical	12.80	12.60	6.00	3.80	463.48	4.76	387.36	98.10	0.0317	1.2000	1.1683	6

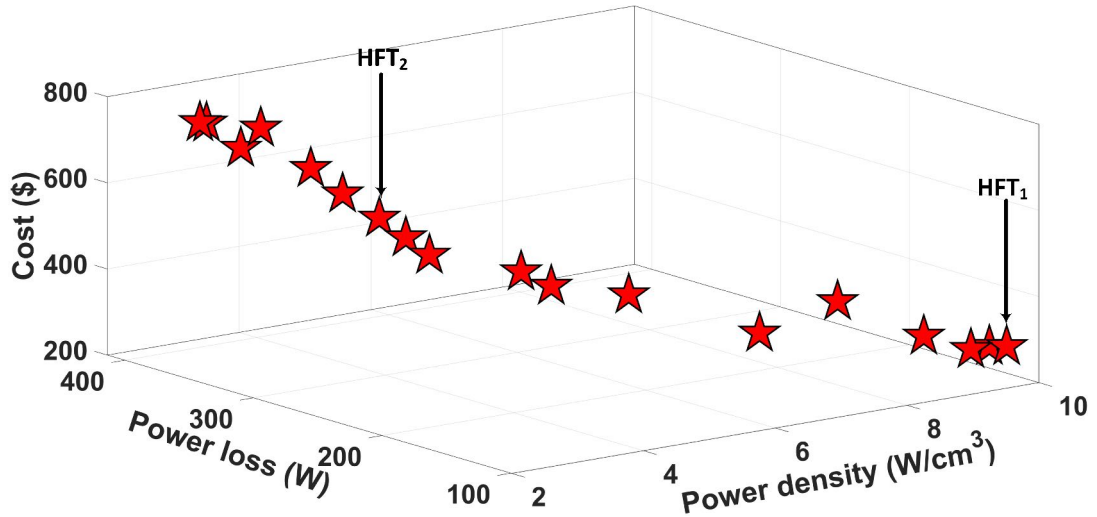


Figure 5.5: 3D plot of the POS of the proposed optimization algorithm

design process. In order to analyze the effect of variation in switching frequency and power loading on the POS efficiency of the HFT, a frequency sweep at rated power of  $20\text{kW}$  and power sweep at rated frequency of  $10\text{kHz}$  is done. The results are as shown in Figs. 5.6a and 5.6b respectively.

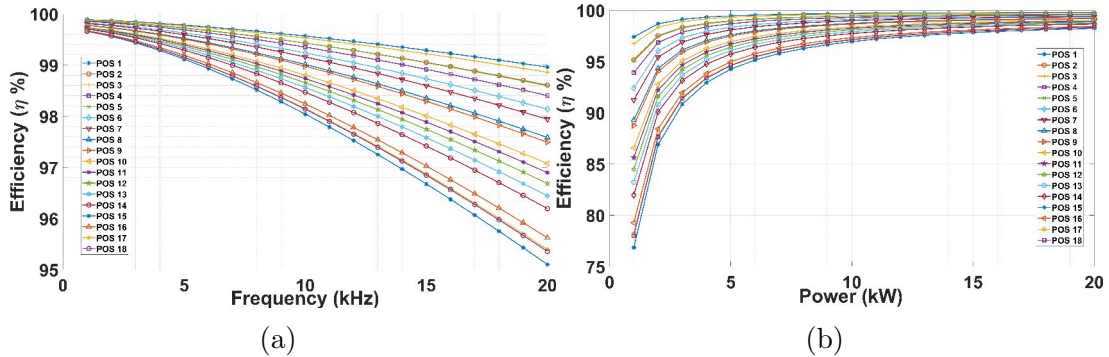


Figure 5.6: (a) Frequency sweep of POS at rated power of the HFT (b) Power sweep of POS at rated frequency of the HFT

At higher switching frequencies, each of the optimal solutions show a decrease in efficiency at rated power with minimum efficiency of  $95\%$  at maximum switching frequency of  $20\text{kHz}$  (as seen in Fig. 5.6a). Also, at low power levels (as seen in Fig. 5.6b) the efficiencies of the HFTs are lower. Both plots show that, high-power-density HFTs (with smaller core sizes and winding volume) suffers lesser

impact in efficiency due to frequency-power variation and vice versa. This is due to their relatively smaller leakage inductance.

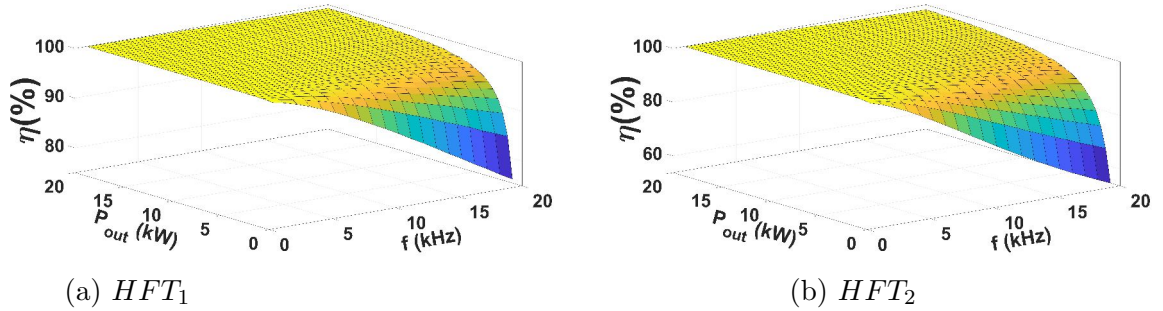


Figure 5.7: 3D Surface plots based on Power-Frequency sweep of  $HFT_1$  and  $HFT_2$

Two (one with high power density and another low power density) of the eighteen POS (resulting from the proposed algorithm) are selected for experimental implementation. As seen from Table 5.3, the gray colored rows (POS 1 and POS 9) are selected based on comparatively different core volume and number of turns. Based on available core sizes off-the-shelf, POS 1 and 9 core sizes closely match (by volume) the AMCC-100 and AMCC-250 POWERLITE C-Cores (by Hitachi metals) respectively. These two HFTs implemented using AMCC-100 and AMCC-250 cores will be subsequently referred to as  $HFT_1$  and  $HFT_2$  respectively in this chapter. A 3D surface plot of the efficiency with power-frequency sweep of  $HFT_1$  and  $HFT_2$  is as shown in Figs. 5.7a and 5.7b, respectively.

### 5.3.1 Multiphysics simulation results

The flux density distribution at rated power and frequency (based in the TE model)  $HFT_1$  and  $HFT_2$  is as shown in Figs. 5.8a and 5.8b respectively. The flux density of  $HFT_1$  is quite higher than that of  $HFT_2$  due to its relatively smaller core cross-sectional area. One of constraints set during the optimization is to ensure that the flux density is below maximum saturation flux density (1.56T) of the cores.

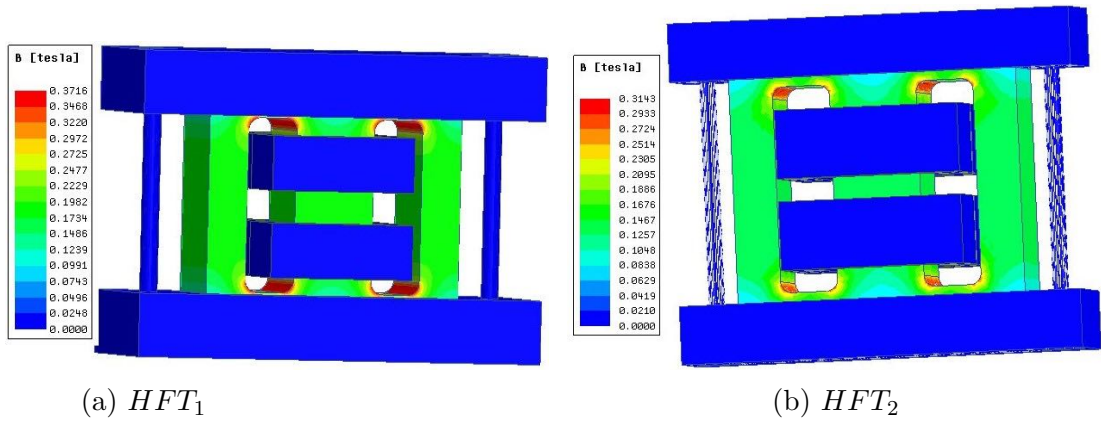


Figure 5.8: Flux density distribution of  $HFT_1$  and  $HFT_2$  at rated power and frequency

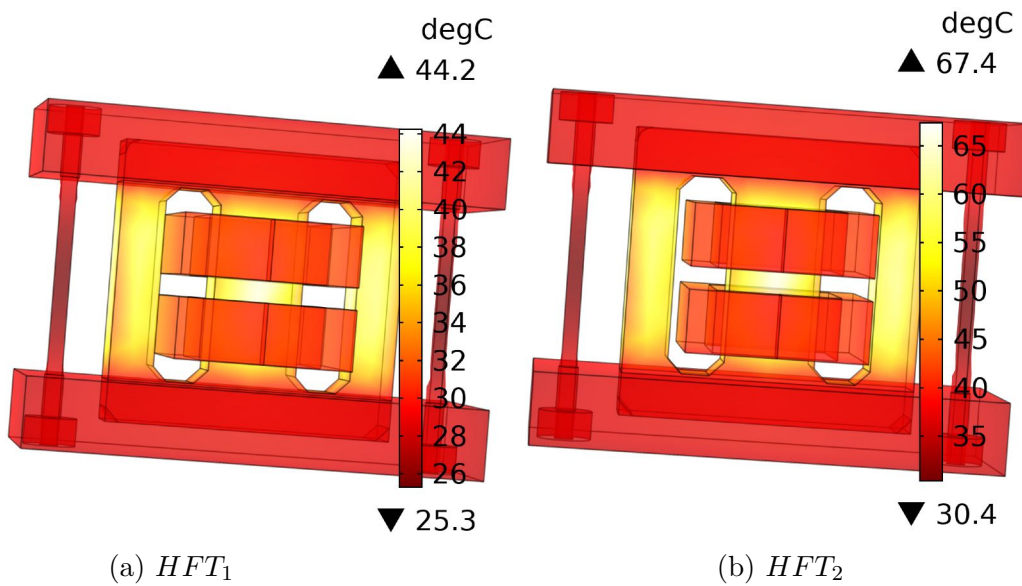


Figure 5.9: Temperature distribution of the HFTs with natural air cooling velocity of 1 m/s (a) for  $HFT_1$ (b) for  $HFT_2$

A higher flux density will increase the power loss and the power density of the HFT. The TE result for both transformers clearly show that the flux densities are well below the maximum saturation flux density of the core used and the values are optimal in order to achieve the desired minimum efficiency. The core and winding loss of the HFT from the time-harmonic electromagnetic model is coupled with the steady state thermal and fluid physics model. The temperature distribution is as shown in Figs. 5.9a and 5.9b for the  $HFT_1$  and  $HFT_2$  respectively. The temperature distribution for  $HFT_1$  shows a maximum temperature of roughly

$45^{\circ}\text{C}$  with an air velocity of  $1\text{m/s}$  while  $HFT_2$  shows a maximum temperature of roughly  $68^{\circ}\text{C}$  with the same air velocity. The higher temperature values in  $HFT_2$  is due to the higher total power loss obtained from the TE simulation. The aluminium material used to physically hold the both cores of the HFT also helps to further dissipate the heat generated by the HFTs. The temperature distribution of both HFTs is within the maximum temperature rise set during the optimization. The analytical optimization result also shows that the  $T_{max}$   $85^{\circ}\text{C}$  compared to similar design for  $HFT_2$  which has a maximum temperature of  $68^{\circ}\text{C}$  based on FEA optimization. The temperature results clearly gives a higher temperature margin compared to the overestimated value obtained using the analytical approach. This highlights one of the benefits of using the FEA-based optimization approach.

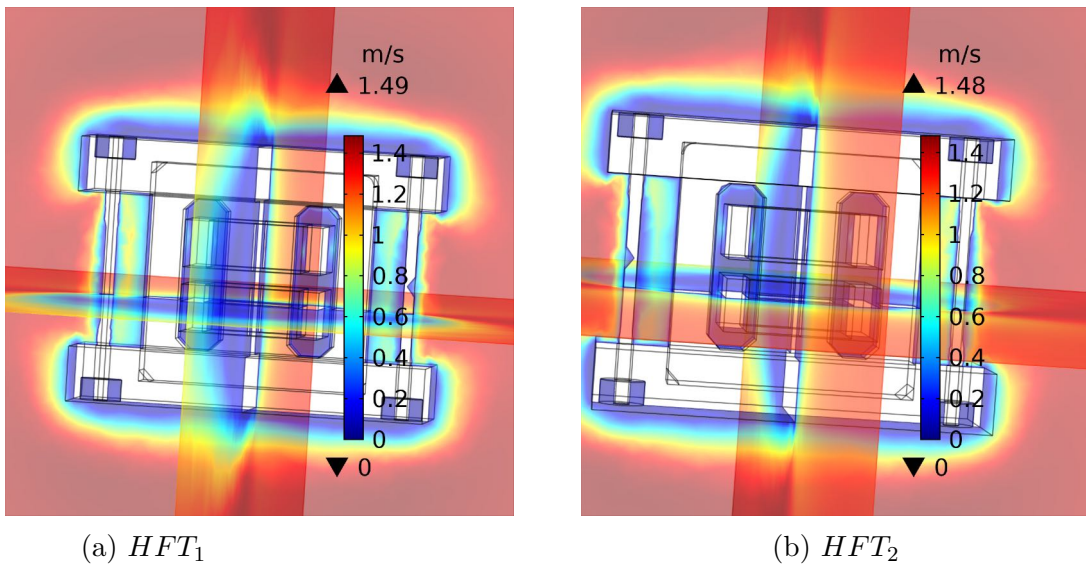


Figure 5.10: Velocity distribution of the air around the HFTs (a) for  $HFT_1$ (b) for  $HFT_2$

The air velocity distribution (based on the fluid physics model) across the  $HFT_1$  and  $HFT_2$  is as shown in Figs. 5.10a and 5.10b, respectively. The window (into/out of the page) of the model is defined as the inlet of the airflow and the velocity of the air is set as  $1\text{m/s}$ . The simulation results show the interaction between the thermal and the fluid physics model. The sides of the HFT close to the air inlet is well cooled compared to other parts of the HFT. The thermal and

fluid model shows that most of the heat generated by the HFT is concentrated around the center limb of the HFTs. The speed of air around the transformer is accelerated around regions with relatively higher temperatures.

### 5.3.2 FEA-based vs Analytical solution

To show the accuracy of the proposed FEA-based optimization algorithm, the  $20kW$ ,  $10kHz$  case study is designed using analytical equation-based optimization approach commonly used in literature. This procedure yields the result presented in the light-gray colored row in Table 5.3. In order to fairly compare the design result with the FEA-based solution, a POS with closely matched  $P_d$  value is used. It can be seen from Table 5.3 that the  $P_d$  (obtained from analytical equation-based optimization) closely matches that of  $HFT_2$  which means they have almost similar core volume. Since the number of turns obtained from the analytical equation-based optimization is lower, it is expected that its winding loss should be smaller consequently a lower temperature rise and higher value of efficiency. Fig. 5.11 shows the comparison between the FEA-based optimization and the result obtained through analytical optimization.

The results clearly show the error introduced by using the analytical-based approach. The efficiency at rated power is 98.86% and 98.10% using the FEA and analytical optimization methods respectively. Also, other electromagnetic and thermal parameters were overestimated by the analytical technique. The  $T_{max}$  obtained at rated condition is  $85^{\circ}C$  compared to  $68^{\circ}C$  obtained using the FEA-based approach as presented in section 5.3.1. The POS obtained from the FEA-based optimization clearly presents other options for selection of the optimal design based on the desired objective of higher priority.

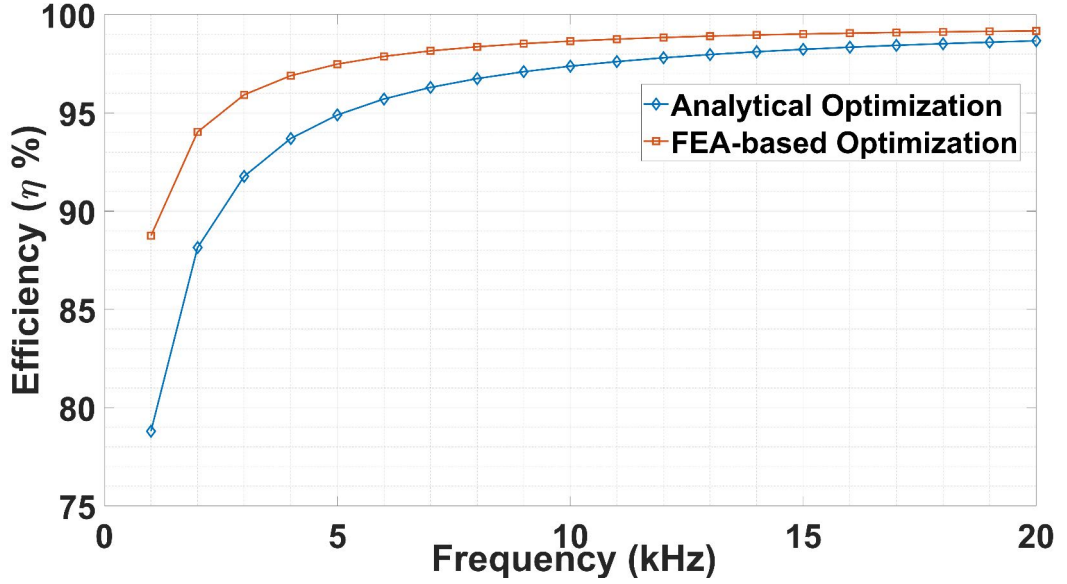


Figure 5.11: FEA-based  $HFT_2$  vs Analytical optimization result

Table 5.4: Experimental specifications

Description	Value
Compensation Capacitor	$2.5\mu F$
$f_s$ for efficiency test	10kHz
Core Material	Amorphous (AMCC-cores)
Conductor Type	1620/36 (4 gauge) Litz Wire

## 5.4 Experimental Implementation and Results

The experimental setup to investigate the performance of the proposed algorithm is as shown in Fig. 5.12. The setup consists of a self-tuned resonant current controller, a dual active converter, the designed HFTs and the load. The specification for the experimental setup is as presented in Table 5.4.

Table 5.5: 20kW Optimization Results and Experimental Results at 10kHz Frequency

		$L_p$ (mH)	$L_s$ (mH)	$L_{kp}$ (mH)	$L_m$ (mH)
$HFT_1$	Optimization Results	0.2892	0.2892	0.0103	0.2789
	Experimental Results	0.3097	0.25	0.014	0.2957
$HFT_2$	Optimization Results	0.7010	0.7010	0.0271	0.6739
	Experimental Results	0.63	0.62	0.026	0.57



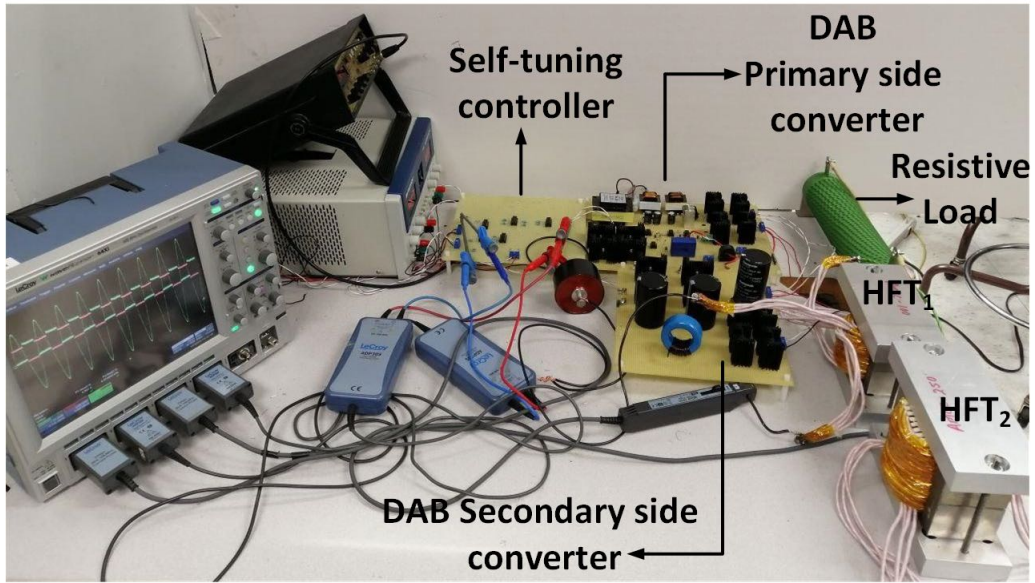


Figure 5.12: HFT implementation and experimental setup

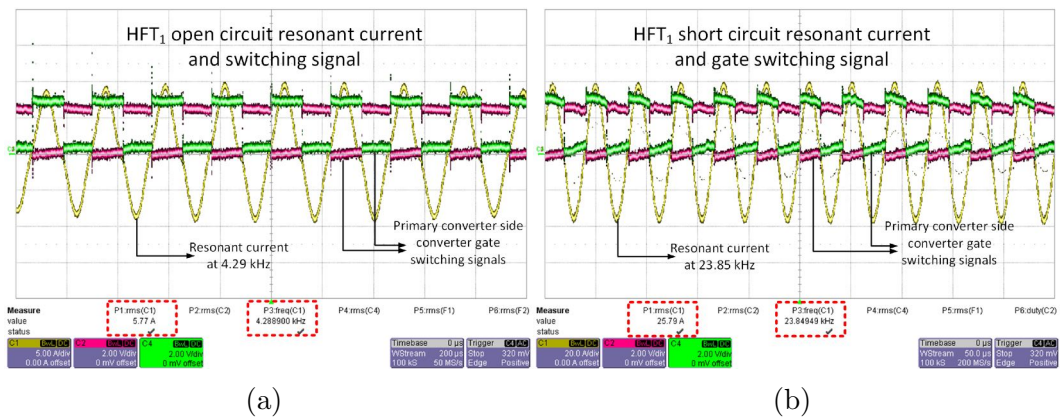


Figure 5.13:  $HFT_1$  Resonant current and primary DAB converter switching pulses (a) Open circuit resonant current and switching signals (b) Short circuit resonant current and switching signals

The self-tuned resonant current controller used in the setup automatically tunes the switching frequency of the IGBTs to the resonant frequency of the LLC tank. This allows the converter to be switched at zero resonant crossings in order to achieve a zero current switching and minimize the switching losses in the converter. Using a known capacitor value of  $2.5\mu F$ , the inductance ( $L_{s,p}$ ,  $L_m$  and  $L_{kp}$ ) values of the HFTs can be estimated by open and short circuiting

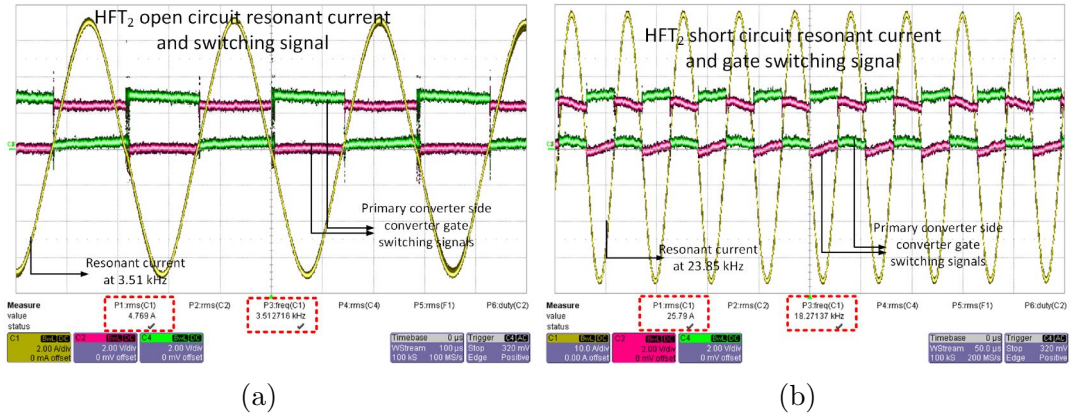


Figure 5.14:  $HFT_2$  Resonant current and primary DAB converter switching pulses (a) Open circuit resonant current and switching signals (b) Short circuit resonant current and switching signals

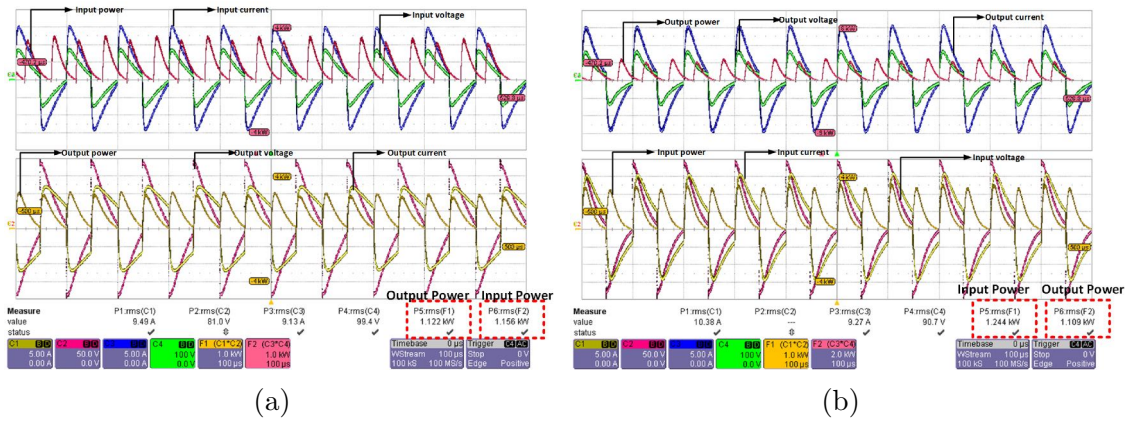


Figure 5.15: Input and Output Power at Low power level (a)  $HFT_1$  (b)  $HFT_2$

the secondary side of the HFT. The inductance measurements are also verified using an LCR meter. Figures 5.13a and 5.13b show the open and short circuit test results for  $HFT_1$  while Figs. 5.14a and 5.14b show the open and short circuit  $HFT_2$ . It can be seen from figures 5.13a, 5.13b, 5.14a and 5.14b that the resonant controller automatically tunes the switching frequency of the primary converter based frequency of the resonant current. Since the leakage inductance is small compared to the primary and secondary inductances of the HFTs (acquired from the open circuit tests, with resonant frequency of  $4.28kHz$  for  $HFT_1$  and  $3.51kHz$  for  $HFT_2$ ), the resonant frequency for the short circuit test is much

higher ( $23.85kHz$  for  $HFT_1$  and  $18.27kHz$  for  $HFT_2$ ). For both  $HFT_1$  and  $HFT_2$  the leakage inductance is calculated from short circuit test while the primary and secondary inductance are obtained from the is obtained from the open circuit tests. The inductance results is as presented in Table 5.5. The experimental results of the inductance values show a very good level of agreement with the optimization results. In order to estimate the efficiency of the HFTs, the input/output power measurement is carried out. Due to laboratory constraints, the HFTs are experimentally tested at lower power levels. The loading of the HFT is done at its rated frequency of  $10kHz$ . It is worthy of note that the rated  $10kHz$  frequency is not the resonant frequency based on  $2.5\mu F$  capacitor used in the setup and the inductances of the HFTs. Therefore the current wave forms are not purely sinusoidal. The load used in the set up is purely resistive which means the voltages and currents will be in phase. Figures 5.15a and 5.15b show the input and output power measured from  $HFT_1$  and  $HFT_2$  respectively. It can be seen from these figures that at low power level, the efficiency of  $HFT_1$  is 97% and that of  $HFT_2$  is 90% approximately.  $HFT_2$  suffers a higher drop in efficiency at low power level due to its bigger core size/volume as evident from the simulation results as shown in Fig. 5.6b. The efficiency values from the experimental results are expected to increase at rated loads which is in good agreement with the simulation results of the proposed optimization algorithm.

## 5.5 Summary

A multiphysics-based and multi-objective optimization approach for HFT design is presented in this chapter. The variables of the optimization are the core parameters and the transformer number of turns. The core parameters dimension constraints were formulated in a way to ensure the feasibility of practical implementation. The proposed algorithm results show the optimal core parameters and

winding number of turns based on the trade-offs between set objectives (efficiency, cost and power density). The core sizes were defined a way to allow practical implementation based on of-the-shelf core dimensions. From the POS, a case study of two HFTs, namely  $HFT_1$  and  $HFT_2$  were investigated and implemented. The multiphysics results presented show the benefits and importance of coupling between electromagnetic, thermal and fluid models of the HFTs. The experimental implementation of  $HFT_1$  and  $HFT_2$  shows a good agreement between the optimization results and the experimental values. At low power level, the efficiencies of the HFTs were 97% for  $HFT_1$  and 90% for  $HFT_2$  with high values of efficiencies expected when loaded at rated power.

**AC-AC MATRIX CONVERTER FOR SST****6.1 Introduction**

SST topologies proposed in literature can be simply categorized into single and multi-stage topologies. These two categories have several sub-topologies based on the circuit configuration. Each of these topologies categories and sub-topologies have various benefits and drawbacks. The single stage are usually categorized as the direct AC-AC conversion with an intermediate isolation transformer in-between. The direct AC-AC conversion has been shown to be one of most efficient topologies. This is largely due the elimination of the bulk capacitor that is needed on the DC link. Examples of SSTs with single power conversion include direct and indirect isolated MCs, single and three-phase AC-AC flyback converter, Dyna-C converter, AC-AC dual active bridge, AC-AC cycloconverter. MCs allow bidirectional flow of power with the use of anti-parallel connected IGBTs/MOSFETS [222, 223]. The drawback of this topology for SST applications, is the absence of the DC port. This prevents the possibility of connecting of renewable energy systems such as photovoltaic (PV), battery storage, and fuel cells. Also MCs have comparatively higher number of IGBTs/MOSFETS, which increases the switching losses of the whole converters. Consequently, soft-switching is of big importance when using MC-based AC-AC topology for SSTs. AC-AC SSTs can be based on direct/indirect MC topology.

Several methods of control for MC-based SSTs have been proposed in literature. Yupeng et al in [224–226] proposed a model predictive control for MC-SST. The proposed algorithm optimally selects the switching signals of the MC by predicting the state variables using the discretized model of the MC-based SST. The proposed MPC is used to control the active power flow to and from the grid. The main drawback of the of the proposed MPC scheme is its inability to achieve

soft switching which potentially increases the switching losses especially at high frequencies. Space vector and carrier based modulation strategies have been proposed for MC-based SSTs [227–231]. Central to these modulation techniques is the need for complex vector computation of the voltages and currents. Also, these modulation methods require complicated close loop control schemes to achieve bi-directional power flow between the AC sources and sinks. These complex control techniques usually make the cost of developing SSTs very high. For resonant converter based MCs, variation in the loads causes variation in the SST’s switching frequency. Therefore, to achieve soft switching at varying loads, self tuning based in the resonant frequency of the LC tank becomes highly beneficial. These problems are yet to be addressed in many resonant converter-based MCs for SST applications. The design optimization of appropriate HFTs in SSTs are usually done using existing analytical equations . This makes accurate estimation of its electromagnetic parameters during optimization almost impossible. The use of physics-based on finite element analysis during its optimization becomes highly beneficial [205].

This chapter presents a proposed simplified logic-based control, that achieves soft-switching and automatically self-tunes the converter switching based on its resonant frequency. The proposed controller is based on controlling energy injection/regeneration in the converter’s LC tank depending on the polarity of the applied AC voltage, direction of the power flow and the resonant current. This control can be simply achieved using logic gates without the need for complex programming of DSPs and FPGAs. A novel and simplified physics-based optimization is also proposed for the SST’s HFT. The algorithm optimizes the efficiency, cost and the leakage inductance of the HFT, which is crucial to the performance of resonant converters.

## 6.2 Proposed control methodology and design of switching logic

The proposed control is based in energy injection and regeneration in the resonant tank of the SST primary side. The operating modes shown in Fig. 6.1 is determined by the direction of the resonant current  $A_d$ , the polarity of the input voltage  $V_p^\pm$ , direction of power  $R_p$  and the signal to either inject/regenerate energy  $E_{i/r}$ .

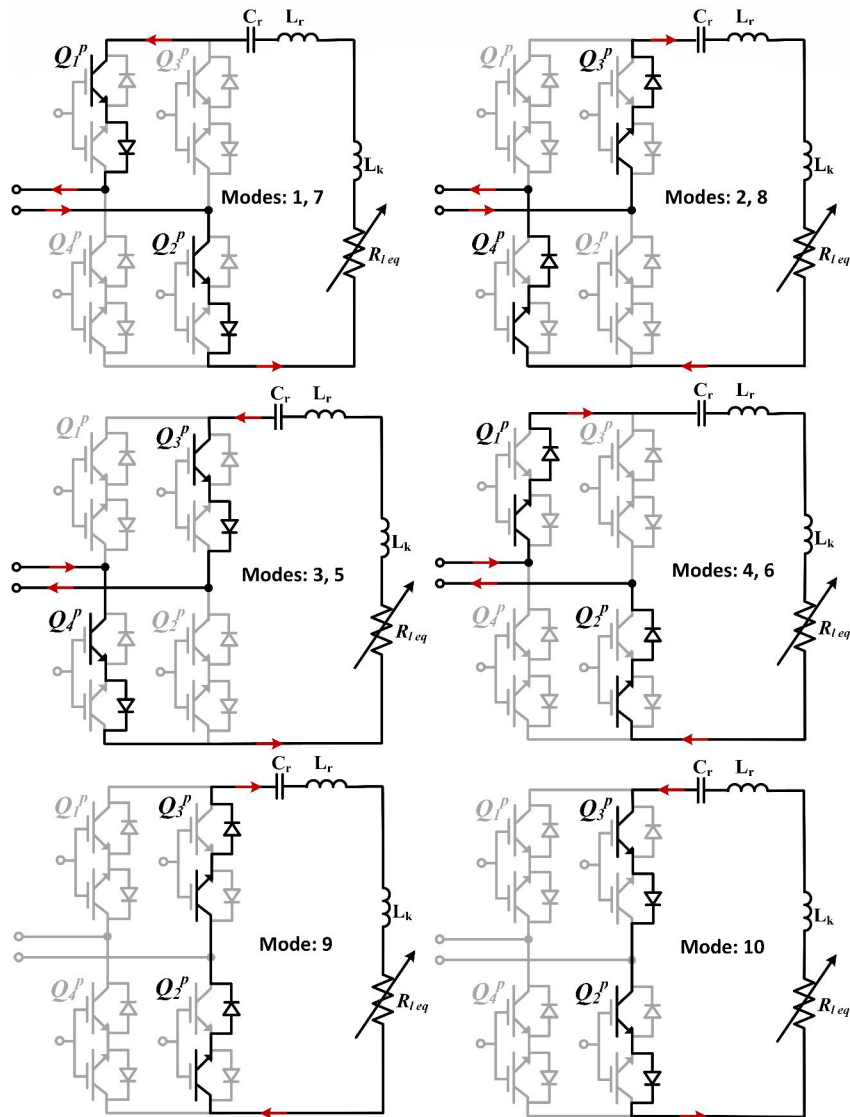


Figure 6.1: Switching modes for the proposed controller

The discrete form of the maximum resonant current in the SST resonant tank is as expressed in (6.1).

$$I_r^{max}[k] = (\Psi[k] - x_1[k]) \frac{\tau e^{-\arctan(\tau\omega)/\tau\omega}}{L_1 \sqrt{1 + (\tau\omega)^2}} \quad (6.1)$$

where

$$L_1 = L_r + L_k, \omega = \sqrt{\frac{1}{L_1 C_r} - \frac{R_{eq}^2}{4L_1^2}}, \text{ in rad/s}, \tau = \frac{2L_1}{R_{eq}} \quad (6.2)$$

$L_r$  and  $C_r$  are the resonant inductance and capacitance,  $L_k$  is the HFT's leakage inductance referred to the primary, and  $R_{eq}$  is the load resistance referred to the primary.  $\Psi[k]$  is the discrete feedback control parameter for the forward and reverse transfer mode, whose next state is as expressed in (6.3) and (6.4) respectively.

$$\Psi[k + 1] = \begin{cases} |V_p| & I_r^{max}[k] < 0 \\ -|V_p| & I_r^{max}[k] < 0 \\ 0 & I_r^{max}[k] = 0 \end{cases} \quad (6.3)$$

$$\Psi[k + 1] = \begin{cases} -|V_p| & I_r^{max}[k] < 0 \\ |V_p| & I_r^{max}[k] < 0 \\ 0 & I_r^{max}[k] = 0 \end{cases} \quad (6.4)$$

Based on the discretized control parameter  $\Psi[k + 1]$  (as expressed in (6.3) and (6.4)), the logic for switching the converter is achieved by making the output voltage of the primary side converter and  $I_r$  of the same sign during energy injection and of opposite signs during energy regeneration. During free oscillation, the output voltage of the primary side converter is kept at zero and the resonant current is allowed to circulate within the resonant LC tank (as shown in modes 9 and 10). The logic table for the modes of operation of the primary side controller is as summarized in Table 6.1.

The switching signals for the primary side of the converter can be derived from Table 6.1 as expressed in (6.5).



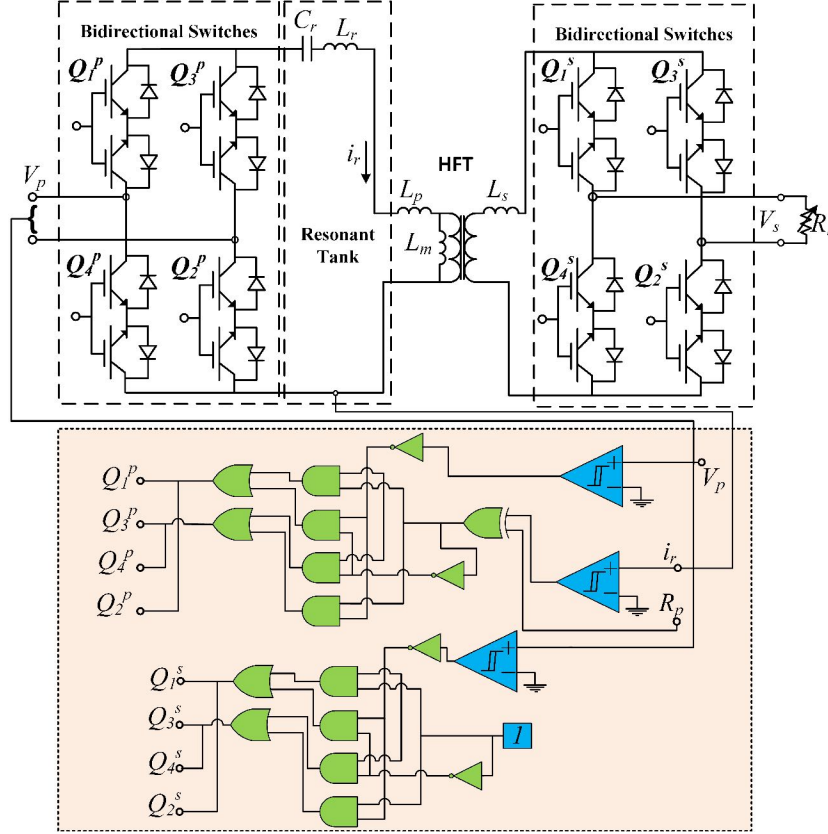


Figure 6.2: Schematic of a direct AC-AC converter with the proposed controller

Table 6.1: Logic for Converter Operating Modes

Modes	$E_{i/r}$	$R_p$	$V_p^\pm$	$A_d$	ON
1	1	0	0	0	$Q_1^p, Q_2^p$
2	1	0	0	1	$Q_4^p, Q_3^p$
3	1	0	1	0	$Q_4^p, Q_3^p$
4	1	0	1	1	$Q_1^p, Q_2^p$
5	1	1	0	0	$Q_4^p, Q_3^p$
6	1	1	0	1	$Q_1^p, Q_2^p$
7	1	1	1	0	$Q_1^p, Q_2^p$
8	1	1	1	1	$Q_4^p, Q_3^p$
9	0	-	-	-	$Q_3^s, Q_2^s$
10	0	-	-	-	$Q_3^s, Q_2^s$

$$\begin{aligned}
 Q_1, Q_2 &= \overline{V_p^\pm} \overline{(A_d \oplus R_p)} + V_p^\pm (A_d \oplus R_p) \\
 Q_3, Q_4 &= \overline{V_p^\pm} (A_d \oplus R_p) + V_p^\pm \overline{(A_d \oplus R_p)}
 \end{aligned} \tag{6.5}$$

In order to achieve zero voltage switching on the secondary side of the MC converter and to achieve a secondary voltage with the same frequency as the primary AC voltage source, the logic circuit design in Fig. 6.2 is used. It is worth

noting that the basic primary control of the proposed MC-based SSC is done on from the primary side of the converter.

### **6.3 High Frequency Transformer Design and optimization with leakage inductance management strategy**

The design of SST's HFT is crucial to the overall performance of the SST. Most of the proposed HFT design optimization algorithms in literature are usually based on analytical iteration [205]. In order to accurately determine the electromagnetic parameters of the HFT during optimization, numerical estimation based on finite element analysis (FEA) is used in this chapter. It is highly desirable to have a HFT with very high efficiency which is quite challenging at high frequencies due to the increase its core loss. For resonant converter based SST's, the HFT's leakage inductance  $L_k$  becomes a crucial design objective. The operating resonant frequency depends on the transformer's  $L_k$ . A large value of  $L_k$  will ensure a wide range of zero current/voltage switching (ZCS/ZVS) for different loading of the SST but could negatively impact the efficiency of the HFT. Therefore, a careful design value for the HFT's  $L_k$  is of huge importance. For the proposed optimization algorithm, the cost of the HFT is also set as an objective which mainly depends on the cost of the litz wire, core material and volume as well as the core binding material (which sometimes can serve as serves as its heat sink). The flow chart of the proposed multi-objective algorithm for the HFT is as shown in Fig. 6.3. The design variables are the operating switching frequency and the number of turns of the transformer which directly relates the transformer's efficiency, leakage inductance and power density.

The optimal flux density (which involves a trade-off between the core volume and the HFT's efficiency) can be calculated using (6.6) [200, 206].  $\rho_{cu}$  is copper's resistivity,  $k_u$  and  $k_f$  is the HFT's stacking and window utilization factors,  $k_a$ ,  $k_c$

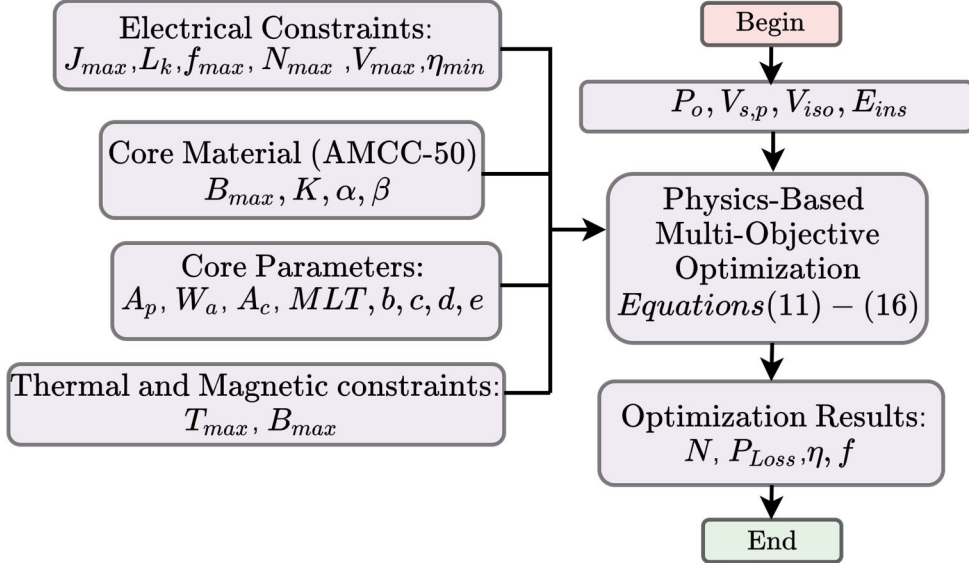


Figure 6.3: Flow chart of the proposed HFT optimization algorithm

and  $k_w$  are based on the type of core used,  $K_v$  is waveform factor, and  $\sum VA$  is HFT's VA rating.

$$B_{op} = \frac{(h_c k_a \Delta \tau)^{2/3}}{2^{2/3} [\rho_{cu} k_w k_u]^{1/12} [k_c K f \alpha]^{7/12}} \left[ \frac{K_v f k_f k_u}{\sum VA} \right]^{1/16} \quad (6.6)$$

The area product for the required core dimensions can be estimated using (6.7).

$$A_p = \left[ \frac{\sqrt{2} \sum VA}{K_v f B_o K_f K_t \sqrt{K_u \Delta \tau}} \right]^{8/7} \quad (6.7)$$

where

$$K_t = \sqrt{\frac{h_c k_a}{\rho_w k_w}}$$

and

$$\sum VA = P_{out} \left( 1 + \frac{1}{\eta} \right) \quad (6.8)$$

In order to estimate the core losses of the transformer, the improved generalized Steinmetz Equation (iGSE) can be used, as expressed in (6.9).  $K$ ,  $\alpha$ , and  $\Gamma$  can be gotten from the data sheet of the core material used.

$$P_{loss}^{core} = \frac{1}{T} \int_0^T k_i \left| \frac{dB(t)}{dt} \right|^\alpha (\Delta B)^{\Gamma - \alpha} dt \quad (6.9)$$

$$k_i = \frac{K}{(2\pi)^{\alpha-1} \int_0^{2\pi} |\cos\theta|^\alpha 2^{\Gamma-\alpha} d\theta} \quad (6.10)$$

The cost objective of the HFT is as expressed in (6.11).

$$C_t = MLT \times (N_p + N_s)C_w + V_c C_c \quad (6.11)$$

where  $C_c$ ,  $C_w$ , are the core and winding cost coefficients.  $N_p$ ,  $N_s$  are the primary and secondary number of turns respectively.

From the FEA simulation, the leakage inductance referred to the primary can be computed using (6.12)

$$L_k = \frac{W}{I_p^2} \quad (6.12)$$

where,

$$W = \frac{1}{2} \int_V A \cdot J dv$$

The loss in the HFT's copper winding and its total loss can be calculated using (6.13) and (6.14) respectively.

$$P_{loss}^{cu} = i_{rms}^2 \times R_{cuac} \quad (6.13)$$

$$P_t = P_{loss}^{cu} + P_{loss}^{core} \quad (6.14)$$

The objective functions and the variables constrains for the optimization algorithm can be expressed as (6.15) and (6.16) respectively.

$$(f, N_{p,s}) = \min(P_t, C_t), \max(L_k) \quad (6.15)$$

$$\begin{cases} f_{min} \leq f \leq f_{max} \\ N_{s,p}^{min} \leq N_{s,p} \leq N_{s,p}^{max} \end{cases} \quad (6.16)$$

## 6.4 Simulations and Results Analysis

A case study of a  $5kW$ ,  $17kHz$ ,  $208/208V$  single phase SST is simulated using the proposed HFT optimization algorithm and MC controller. A resonant capacitor  $C_r = 2\mu F$ , output filter capacitor  $C_o = 100\mu F$ , output filter inductor  $L_r = 5mH$  and HFT parameters in Table 6.2 are used. The HFT optimization is carried out using MATLAB coupled with Finite Element Analysis software. The amorphous *AMCC* – 50 core is selected with dimensions and material properties as stipulated in the manufacturer’s data sheet. These data is fed into the optimization algorithm. One of the optimization results (from the Pareto optimal values) is selected and used with proposed MC controller while the entire SST is subsequently simulated using MATLAB/Simulink.

### 6.4.1 HFT optimization results

The HFT optimization produced 43 Pareto optimal solutions. The frequencies and their corresponding number of primary and secondary turns is as shown in Fig. 6.4.

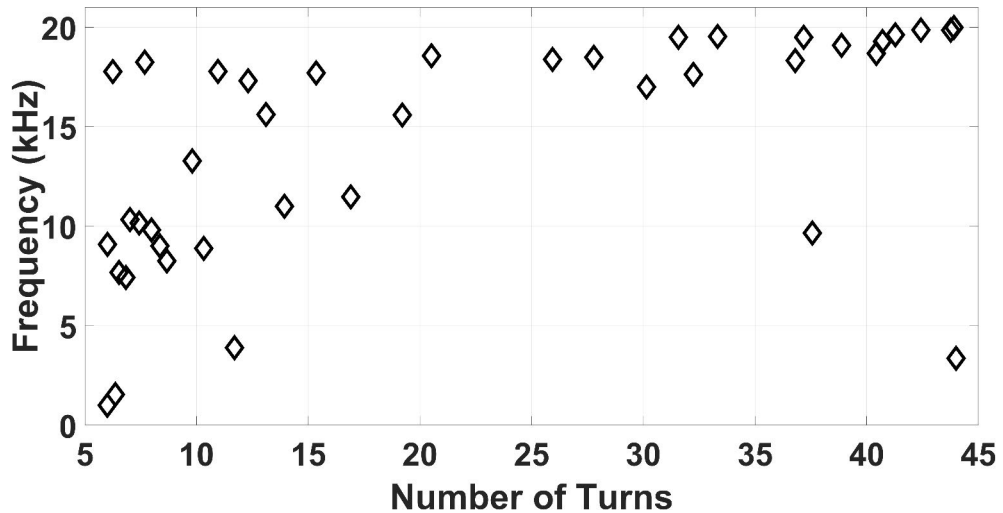


Figure 6.4: Optimal Frequencies vs Number of turns from Pareto solutions

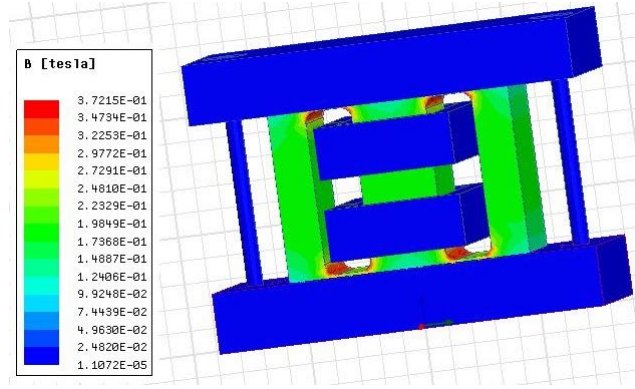


Figure 6.5: Flux density distribution of the optimized HFT

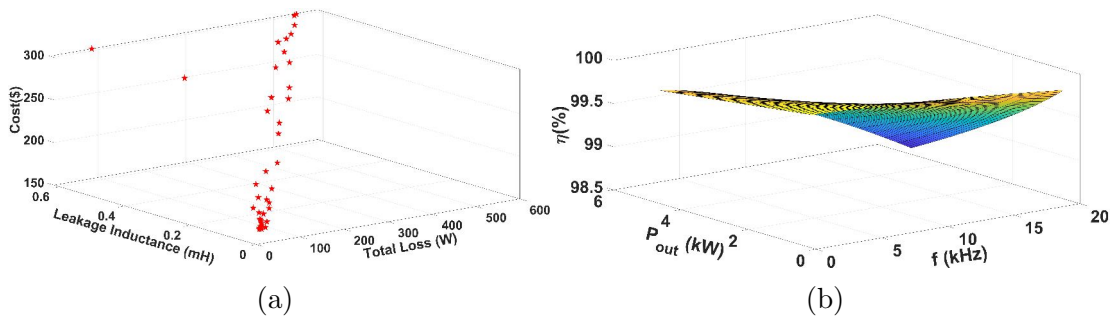
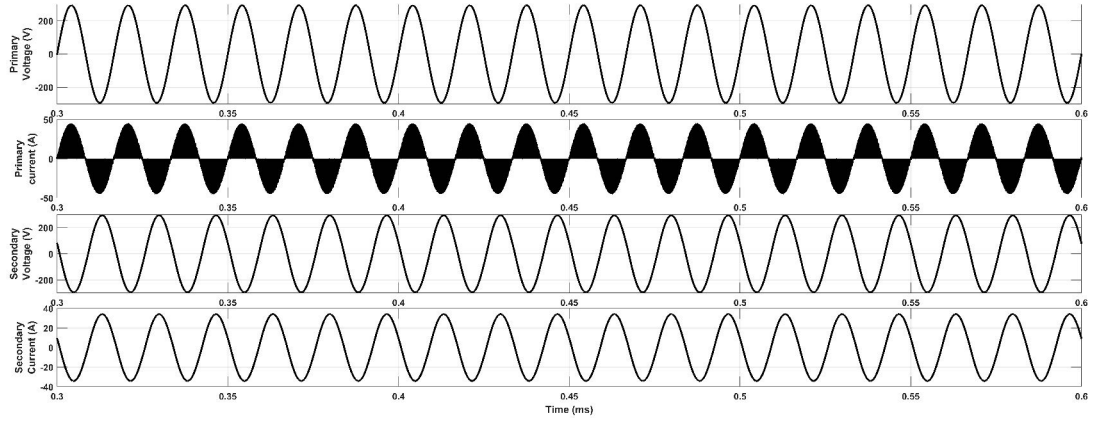
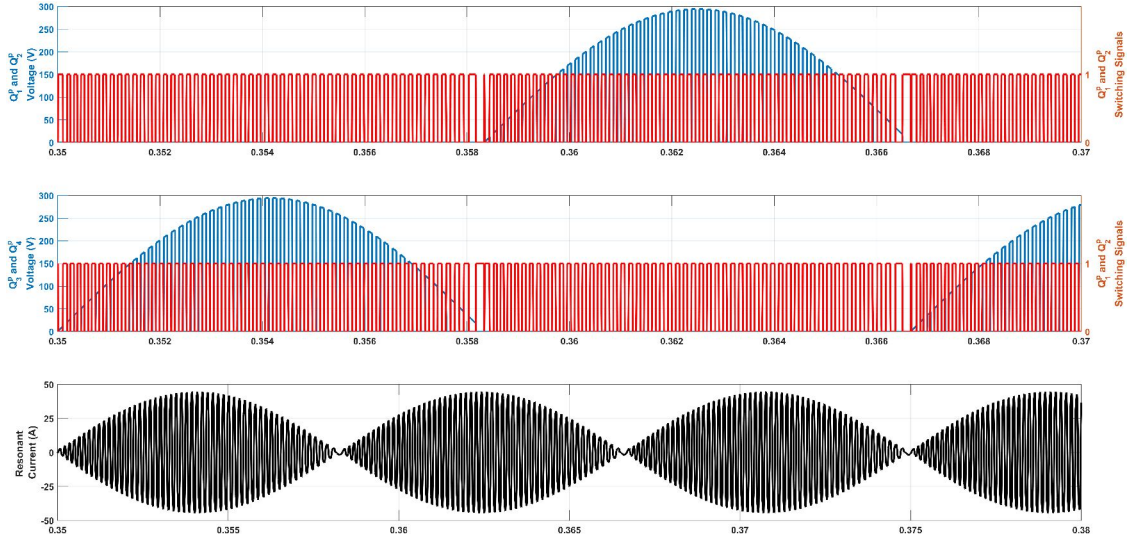


Figure 6.6: (a) 3D plot of Pareto-optimal values of the objective functions (b) HFT's efficiency with varying frequency and output power

The 3D plot of the optimized objectives (based on the Pareto optimal solutions) is as shown in Fig. 6.6a. The plot clearly shows the relationship between the leakage inductance, cost and the total loss in the HFT. A selection of the (based on the objective of priority) operating frequency and the corresponding number of turns can be made from the optimized solutions. Selecting one of the optimal solutions with  $N_p = 17$ ,  $N_p = 17$  and switching frequency of  $17kHz$ , a 3D electromagnetic model is developed. The flux density distribution of the HFT is as shown in Fig. 6.5. The flux density distribution (with maximum of  $0.37T$ ) is well below the maximum saturation flux density of the *AMCC – 50* core which is  $1.56T$ . Table 6.2 shows the inductance values, switching frequency, power loss, efficiency and cost of the selected HFT from the optimization results.



(a)



(b)

Figure 6.7: (a) Plot showing the MC-SST input voltage, primary current, secondary voltage and secondary output current (b) Plot showing voltage across Primary switches and switching signal as well as the resonant current within the LC tank

Table 6.2: HFT parameters used based on one of the optimal solutions

$L_{p,s}$ (mH)	$N_{p,s}$ (Turns)	$L_k$ ( $\mu$ H)	$L_m$ (mH)	f (kHz)	$P_t$ (W)	$\eta$ (%)	$C_t$ ( $\$$ )
1.64	16	75.1	1.62	17	81.33	98.6	199

The varying load conditions (from no load to full load) during the SST operation will cause a variation in operating switching frequency of the converter. This variation in switching frequency will impact the efficiency of the HFT. Since the proposed controller is self-tuned and soft-switched at all loading conditions, the

converter losses are significantly minimized. The frequency/output power sweep of the HFT is as shown in surface plot in Fig. 6.6b. The plot shows how the frequency and load variation impacts the efficiency of the HFT and consequently the efficiency of the entire MC-based SST.

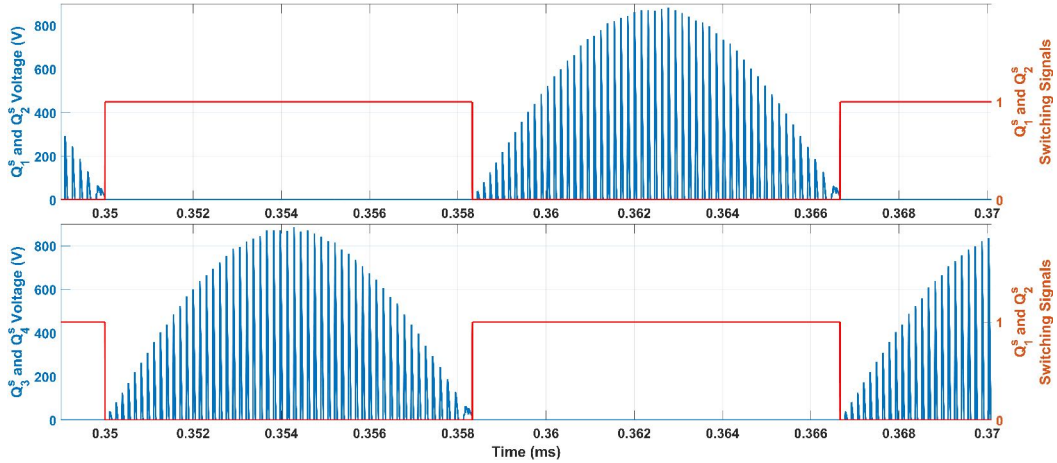


Figure 6.8: Plot showing voltage across secondary switches and their switching signals

### 6.4.2 MC-based SST simulation results

The SST simulation results is as shown in Figs. 6.7 and 6.8. As seen in Fig. 6.7a, the output voltage of the converter is well regulated at  $208V_{rms}$ ,  $295V_{pp}$  with the input voltage set at the same value. The secondary current is in phase with its voltage due to the purely resistive nature of the load. Figs. 6.7b and 6.8 show that the proposed controller is able to achieve zero voltage switching across all the primary and secondary sides converter switches. This is crucial in order to minimize the switching losses and maximize the efficiency of the entire SST MC-based topology. The resonant current plot is also as shown in Fig. 6.8. The perfectly sinusoidal nature of the resonant current plot when zoomed-in shows that the controller is able to self-tune irrespective of the changes in load.



## 6.5 Summary

Highly efficient and cost effective SSTs are desirable for future deployment on distribution and transmission feeders. Direct AC-AC MC-based SSTs are promising candidates due to the absence of an intermediate DC link which necessitates the use of DC link capacitors. For resonant MC-based SSTs, achieving high efficiency, cost effectiveness, self-tuning and soft switching become highly imperative. This chapter proposed a simplified logic based controller for the converter switches and a physics based design optimization algorithm for the SST's HFT. The results showed that the proposed logic based controller can achieve soft switching at various loading conditions, automatically tune itself based on the variation in resonant frequency as well as bidirectionally transfer power between the primary and secondary converters. The proposed HFT optimization algorithm will allow designers to analyze the various trade-offs in the design objectives and select the right parameters for the HFT.

## CHAPTER 7

### VOLTAGE-CONTROLLED RESONANT DC/DC CONVERTER FOR SST APPLICATION

This chapter presents an amplitude modulation technique based on resonant current control for voltage regulation. The error in the output voltage is used to regulate the quantum energy in the resonant tank. The converter switching frequency is synchronized with the resonant current to achieve a self-tuned controller. Several control techniques have been proposed for resonant DC/DC converters. Phase shift modulation methods which includes the single [232], dual [233] and triple [234, 235], and extended-phase-shifts [236, 237] modulation techniques have all been proposed in by several authors. It is difficult to achieve ZVS with these modulation techniques when the converter is operated in a wide range of voltage gain [238]. Hybrid control techniques with different resonant tank topologies have been proposed by [239–243] in order to increase the input voltage gain of the converter. Authors of [244] presents a modulation technique that regulates the output voltage of a resonant DC-DC converter based on the input voltage as a feed-forward loop and also regulates the output by changing the switching frequency. Reference [238] proposes a series resonant DC-DC converter that changes its operation states based on the level of the input and output voltages. The proposed converter uses a fixed-frequency PWM which makes its gain independent of its magnetizing inductance consequently reduces the complexity in designing the resonant tank. Authors of [245] uses a semi-active rectifier to enable a voltage step-up on the output side of a series resonant converter. The converter is regulated at a constant switching frequency which is almost the same as the resonant frequency. However, most of these control schemes in literature are usually very complicated with the need for very costly DSPs and FPGA, while some still falls short in achieving a wide voltage regulating range.

These drawbacks are addressed in the proposed controller. The proposed con-

troller modulates the amplitude resonant current in the resonant tank based on the output voltage error to determine quantum energy injection or free oscillation.

## 7.1 Theoretical Analysis and modelling of resonant DC-DC Converter

Since the high harmonic contents of the square wave produced by the DC inverter is filtered out by the resonant tank at resonant frequency, the fundamental approximation of the converter is used for analyzing the behavior of the converter . Also, the overall power transfer from  $V_{in}$  to  $V_{out}$  is contributed by only the fundamental component of the inverted DC voltage. Low ripple approximation method can be used since the output filter is much more greater than the resonant capacitor. The equivalent circuit of the converter is as shown Fig. 7.1. From Fig. 7.1, the voltage gain in time and frequency domain is as derived in equations (7.1) and (7.3) respectively where  $n$  is the high frequency transformer turns ratio.

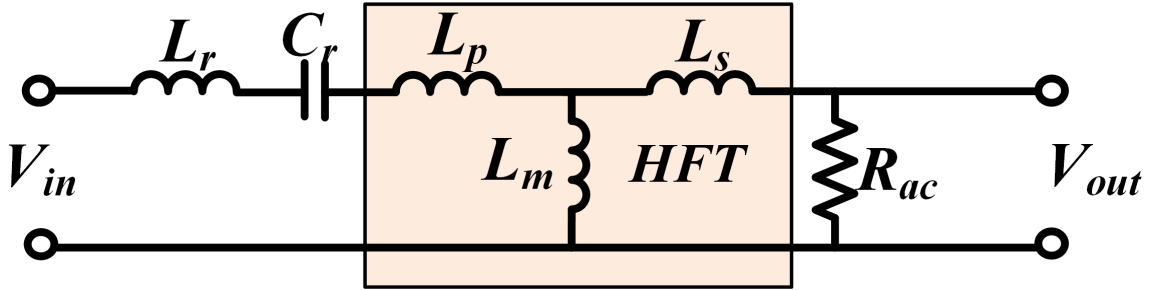


Figure 7.1: Converter equivalent circuit

$$H(s) = \frac{V_o(s)}{V_{in}(s)} = \frac{s^2 L_m R_{ac}^{eq} C_r}{s \left[ 1 + \frac{s^2 [L'_1 C_r (n^2 L_2 + L_m) + n^2 L_m L_2 C_r]}{n^2 L_2 + L_m} \right] \times (L_m + n^2 L_2) + R_{ac}^{eq} \left[ 1 + s^2 (L'_1 + L_m) \right]} \quad (7.1)$$

substituting  $s = j\omega$

$$\begin{aligned}
H(j\omega) &= \frac{V_o(j\omega)}{V_{in}(j\omega)} \\
&= \frac{-\omega^2 L_m R_{ac}^{eq} C_r}{j\omega \left[ 1 + \frac{-\omega^2 [L'_1 C_r (n^2 L_2 + L_m) + n^2 L_m L_2 C_r]}{n^2 L_2 + L_m} \right] \times} \\
&\quad (L_m + n^2 L_2) + R_{ac}^{eq} \left[ 1 - \omega^2 (L'_1 + L_m) \right]
\end{aligned} \tag{7.2}$$

$$\begin{aligned}
|H(j\omega)| &= \frac{V_o(j\omega)}{V_{in}(j\omega)} \\
&= \frac{\omega^2 L_m R_{ac}^{eq} C_r}{j\omega \left[ 1 - \frac{\omega^2}{\omega_o^2} \right] (L_m + n^2 L_2) + R_{ac}^{eq} \left[ 1 - \frac{\omega^2}{\omega_1^2} \right]}
\end{aligned} \tag{7.3}$$

where

$$R_{ac}^{eq} = \frac{8n^2}{\pi} R_o^{load}$$

$$L'_1 = L_1 + L_r$$

$$L_R = L'_1 + L_m / n^2 L_2$$

$$L_p = L_m + L'_1$$

$$\omega_o = \frac{1}{\sqrt{L_R C_r}}$$

$$\omega_1 = \frac{1}{\sqrt{L_p C_r}}$$

Figure 7.2 shows that the  $H_{j\omega}$  changes as the resonant frequency varies. This causes the voltage output  $V_{out}$  to vary significantly with changes in load.

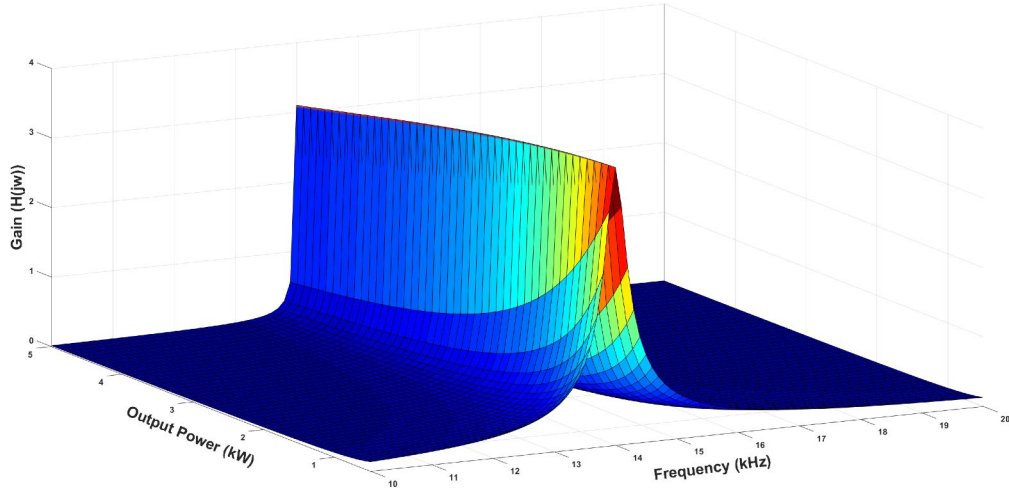


Figure 7.2: Surface gain plot of the resonant under varying load and frequency with  $L_m/L'_1 = 5$

## 7.2 Proposed Voltage Regulation Controller

This chapter proposes a voltage control technique by regulating the energy stored in the resonant tank by varying the resonant current. The concept plot for the proposed resonant current control is as shown in 7.3. Energy is regenerated when

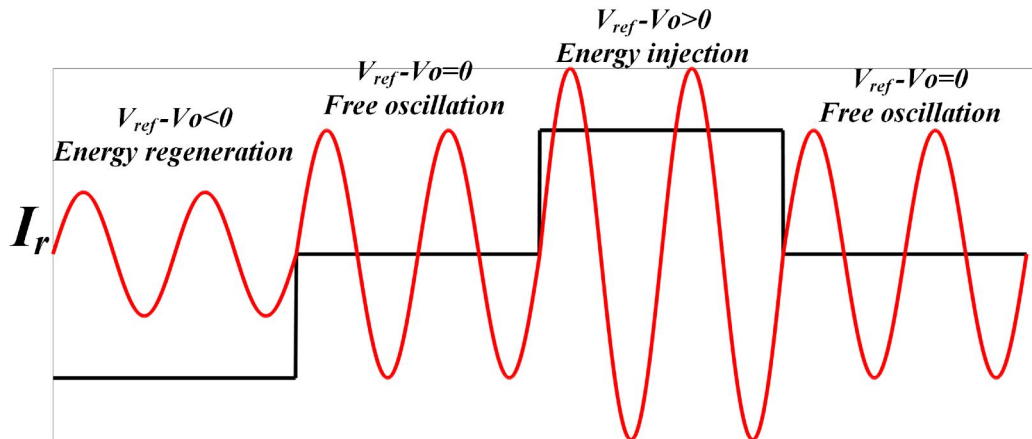


Figure 7.3: Conceptual plot of the proposed controller

$V_{out} > V_{ref}$  (which decreases the resonant current) and injected when  $V_{out} < V_{ref}$  (which increases the resonant current). The converter freely oscillates the energy stored in the resonant tank whenever  $V_{out} = V_{ref}$ . The six modes of the converter operation is as shown in Fig. 7.4. In order to achieve soft switching, the change in mode is done at the zero crossing points to minimize the switching losses. The

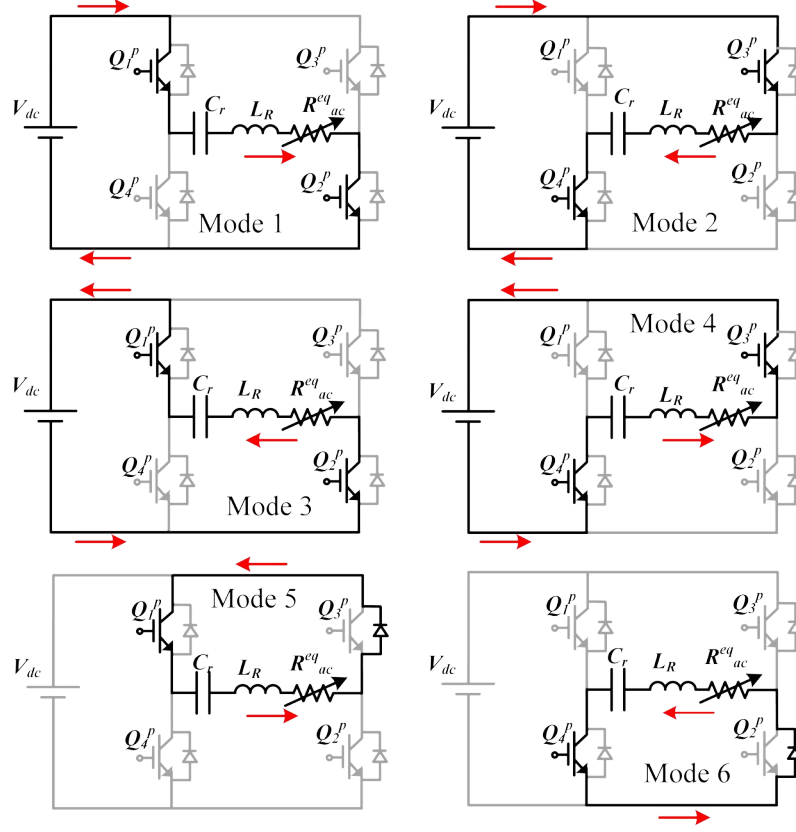


Figure 7.4: Six operation modes of the proposed controller

discretized control law for the converter is as expressed in (7.4)- (7.6). The logic states of the primary converter switches is as presented in Table 7.1.  $E_{i/r}$  is the signal to either inject/regenerate or freely oscillate,  $D_v$  is the sign of the difference of  $\Delta V[k]$  and  $I_d$  is the direction of the resonant current. From Table 7.1, the switching logic design can be realized using equation (7.7).

$$\Psi[k+1] = \begin{cases} \text{Energy injection mode} \\ |V_{in}| & \Delta V[k] > 0 & I_{res}[k] > 0 \\ -|V_{in}| & \Delta V[k] > 0 & I_{res}[k] < 0 \end{cases} \quad (7.4)$$

$$\Psi[k+1] = \begin{cases} \text{Energy regeneration mode} \\ |V_{in}| & \Delta V[k] < 0 & I_{res}[k] > 0 \\ -|V_{in}| & \Delta V[k] < 0 & I_{res}[k] < 0 \end{cases} \quad (7.5)$$

$$\Psi[k + 1] = \begin{cases} \text{Free oscillation mode} \\ 0 & \Delta V[k] = 0 \quad I_{res}[k] > 0 \\ 0 & \Delta V[k] = 0 \quad I_{res}[k] < 0 \end{cases} \quad (7.6)$$

where  $\Delta V[k] = V_{ref}[k] - V_{out}[k]$ ,  $I_{res}$  is the resonant current and  $V_{in}$  is the input voltage.

Table 7.1: Logic for Converter Operating Modes

Modes	$E_{i/r}$	$D_v$	$I_d$	$Q_1^p$	$Q_2^p$	$Q_3^p$	$Q_4^p$
1	0	0	0	1	1	0	0
2	0	0	1	0	0	1	1
3	0	1	0	0	0	1	1
4	0	1	1	1	1	0	0
5	1	0	0	0	0	0	0
6	1	0	1	0	0	0	1

$$\begin{aligned} Q_1^p &= \bar{D}_v \bar{I}_d + \bar{E}_{i/r} D_v I_d \\ Q_2^p &= \bar{E}_{i/r} (\bar{D}_v \bar{I}_d + D_v I_d) \\ Q_3^p &= \bar{E}_{i/r} (D_v \oplus I_d) \\ Q_4^p &= \bar{E}_{i/r} (D_v \oplus I_d) + \bar{E}_{i/r} \bar{D}_v I_d \end{aligned} \quad (7.7)$$

### 7.3 Simulation Results and Analysis

The schematic of the proposed controller and the converter is as shown in Fig. 7.5.

The converter and the controller is simulated using MATLAB/Simulink. The high frequency transformer used for the simulation has a primary and secondary inductance of  $1.64mH$ , its leakage inductance is  $76\mu H$  and its turns ratio is 1:1. The compensation/resonant capacitor is  $2.5\mu F$ . The output voltage reference is set at  $180V$  while the input was set at steps of  $150V$ ,  $250V$  and  $210V$  during the simulation. The simulation results is as shown in figures 7.6 and 7.7. The input

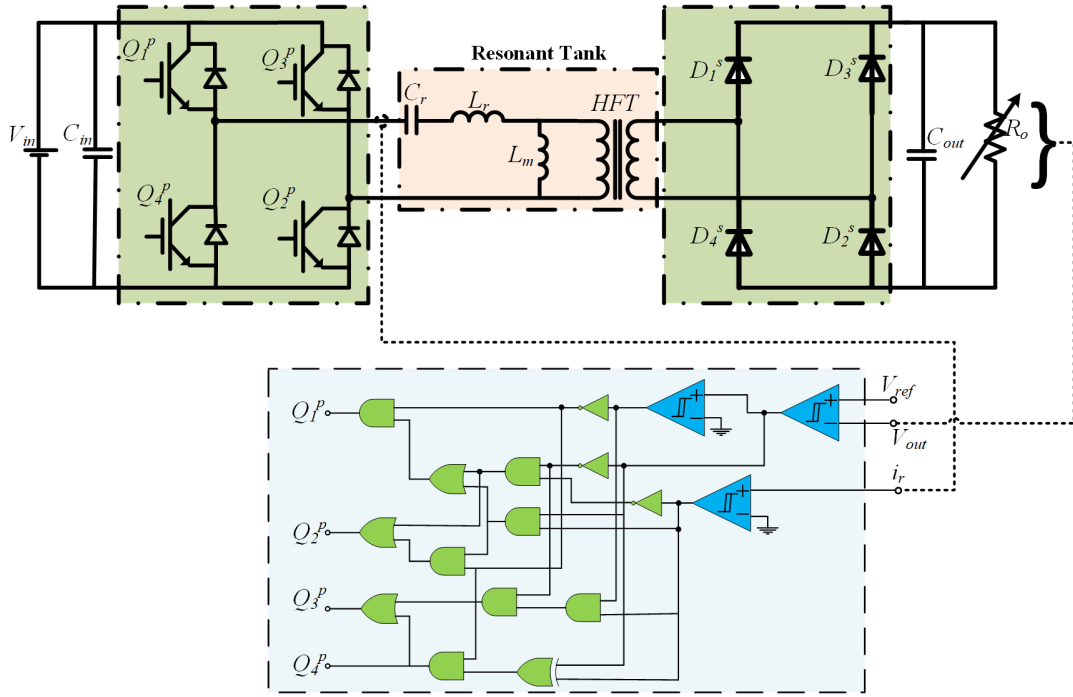


Figure 7.5: Converter with the proposed controller

voltage  $V_{in}$ , output voltage  $V_{out}$  and the resonant current  $I_r$  plots is as shown in Fig. 7.6. The figure shows that as  $V_{in}$  changes, the resonant current is regulated in order to keep the  $V_{out}$  within the reference voltage. The MOSFET voltage and current is as shown in Fig. 7.7. It can be seen from the figure that soft switching is achieved on the primary side of the converter.

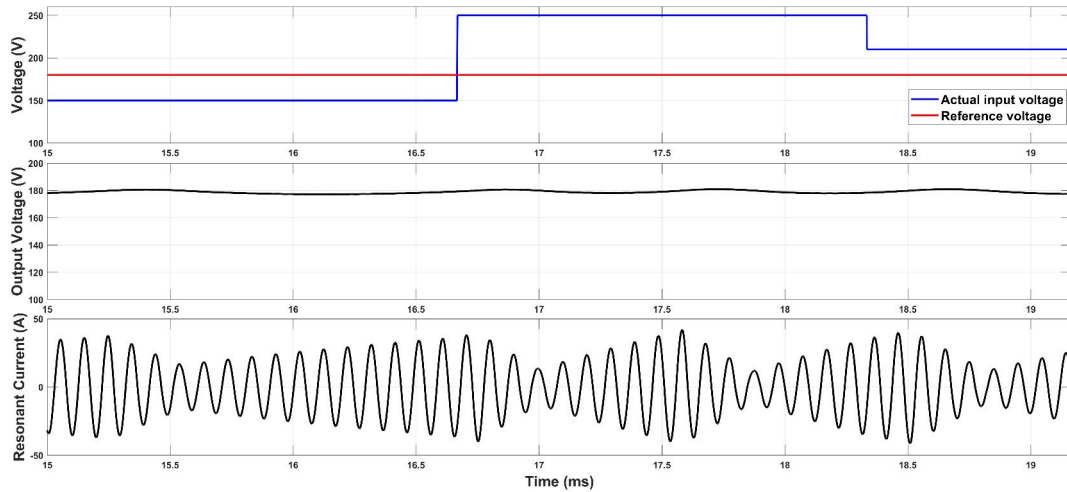


Figure 7.6: Plot of changes in input voltage, regulated output voltage and resonant current



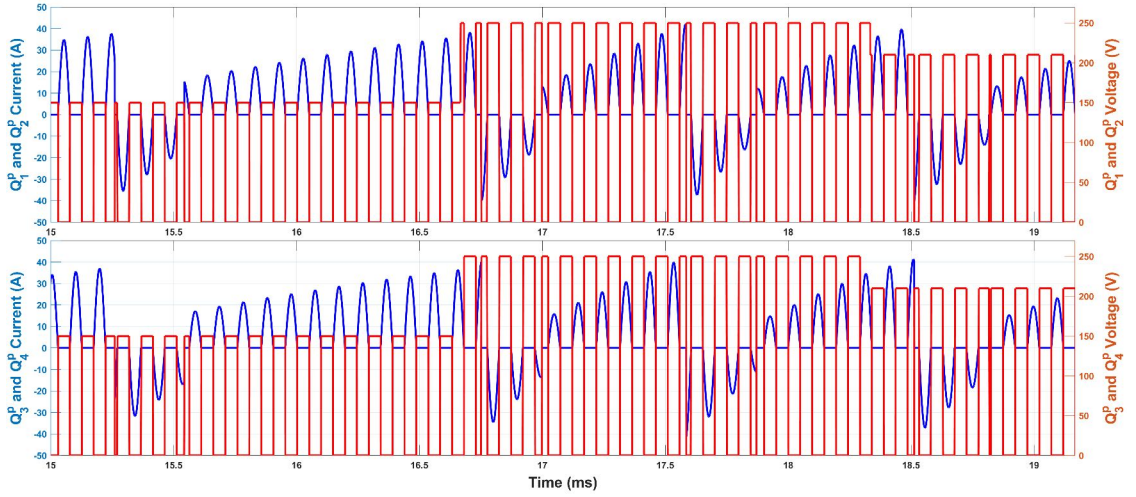


Figure 7.7: Primary converter switches voltage and current

## 7.4 Experimental Results and Analysis

In order to validate the performance of the proposed controller, the experimental setup shown in Fig. 7.8 is used. The experimental parameters of the HFT, the

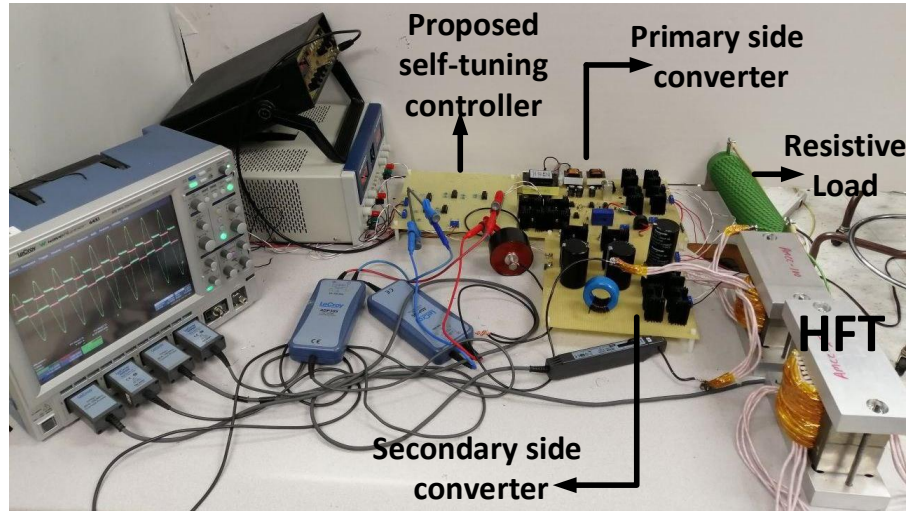


Figure 7.8: Experimental setup to validate the proposed controller

resonant capacitor and the output filter capacitor is presented in Table 7.2.

The reference output voltage for the experimental setup is set at 30V. The experimental results is as shown in figures 7.9b-7.11. With  $V_{in}$  is set at 40V and 50V in Figs. 7.9a and 7.9b respectively,  $V_{out}$  is well regulated at 30V by the controller as proposed.

Table 7.2: Experimental specifications

Description	Value
Compensation Capacitor	$2.5\mu F$
Primary and Secondary Inductance $L_{p,s}$	$1.64mH$
Number of turns $N_{p,s}$	16 Turns
Leakage Inductance $L_k$	$75.1\mu H$
Magnetizing Inductance $L_m$	$1.62mH$
Output filter capacitor	$0.5mF$

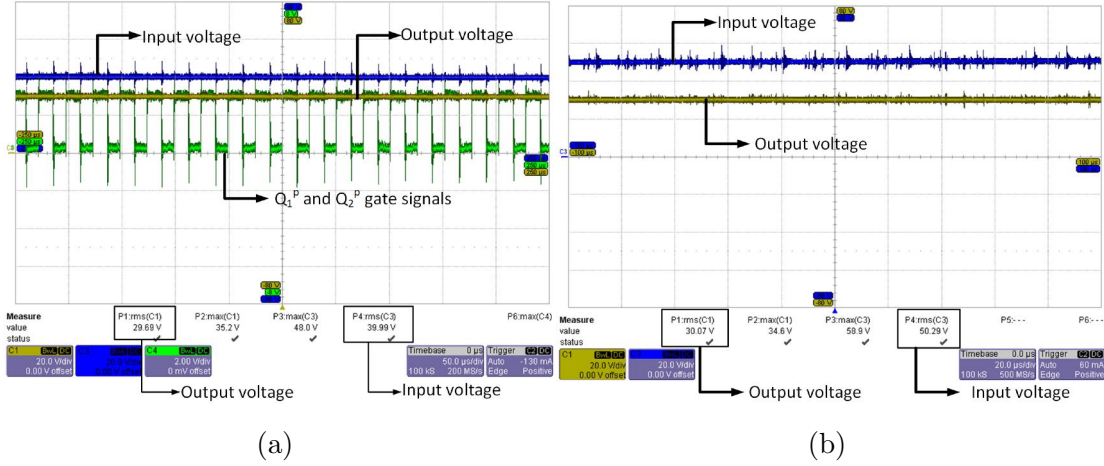


Figure 7.9: (a) Output voltage with input voltage set at 40V (b) Output voltage with input voltage set at 50V

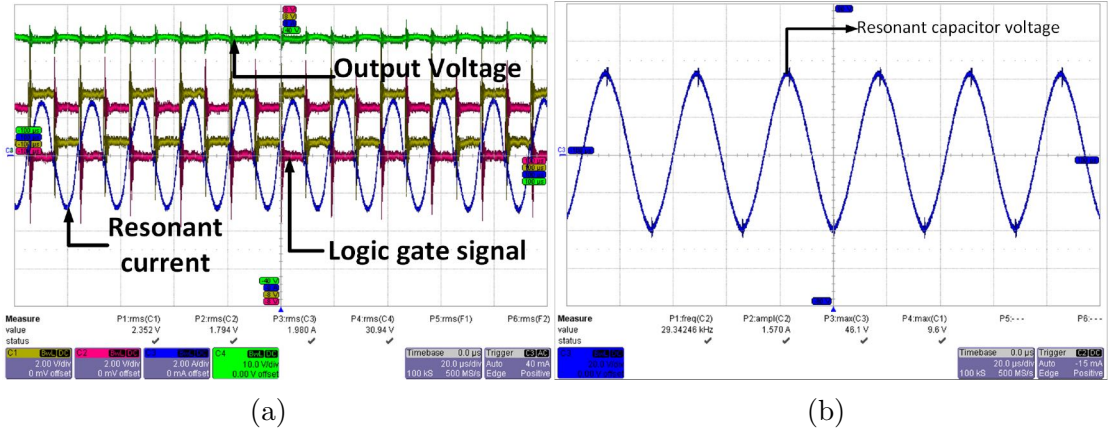


Figure 7.10: (a) Primary converter gate signal showing ZCS. (b) Plot of voltage across resonant capacitor

The proposed controller is able to achieve zero current switching on the primary switches of the converter. This is as shown in Fig. 7.10a. The realization of the

ZCS allows the converter achieves a low switching loss and improved efficiency. The voltage across the resonant capacitor is shown in Fig. 7.10b while the resonant current is as shown in Fig. 7.11.

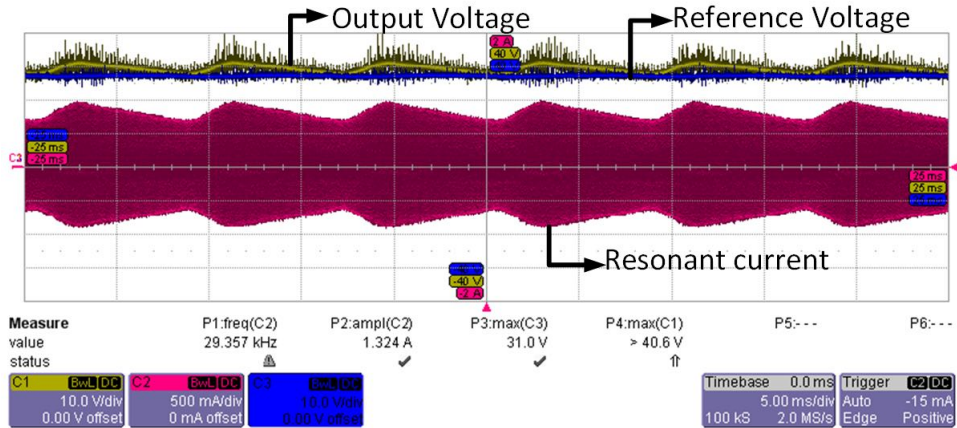


Figure 7.11: Plot of input/output voltage and resonant current.

## 7.5 Summary

A voltage controller for a series resonant DC/DC converter is proposed in this chapter for solid state transformer applications. The proposed controller is based regulating the quantum energy injection/regeneration using the resonant current of the converter and the output voltage error. The controller enable soft switching across the four switches of the primary converter. The proposed controller was developed using logic gates with simulation performed on MATLAB/Simulink. The resonant current in LLC tank can be effectively regulated to achieve the desired reference output voltage. This was verified through simulation and validated through experimental results.

## CHAPTER 8

### CONCLUSIONS AND FUTURE WORK

This thesis explores the challenges with high penetration of renewable energy sources such as PV systems. Voltage control and optimization becomes highly important due to the intermittent nature of the power generation from PV systems. Three approaches were used to develop solutions that addresses the voltage control and optimization problems with high PV penetration in smart grid.

In chapter 2, various challenges with PV penetrated network and classified them based on their areas of impact. With the inevitable future increase in PV penetration, this chapter also took an extensive look at different future scenarios and their impacts with higher levels PV penetration in the network. The present technical solutions with the existing penetration was also presented. Many of these existing solutions need further development with some future research direction indicated in this chapter. This review showed that the technical, operational and environmental challenges with PV integrated network are still incipient and would become more prominent with increased level of penetration, especially within the context of the future scenarios earlier discussed. The dynamics of the smart grid is expected to change with these future scenarios. More advanced and adaptive techniques have to be developed to mitigate the challenges that would arise in these scenarios.

In chapter 3, a comprehensive review of different methods and techniques of PV aggregation highlighting their various strength and weaknesses has been presented. By using some real data from the power generation of four PV sites in Florida, an analysis of the various impacts of PV aggregation is also presented. The study of how the correlation in the power output and irradiance data affects various PV aggregation is also shown in this chapter. The effect of PV density on the variability of the aggregated PV fleets, how distance between PV sites also affects the aggregated PV systems are also presented. An analysis of the aggregation

of four PV fleets was done with different combinations of the PV fleets using statistical models and discrete meyer wavelet to study the reduction in variabilities with different combinations of the PV fleets. The result showed that the relative sizes of the PV fleets have significant impacts on the reduction in variabilities of the aggregated system. The correlation between these sites also shows significant influence in the reduction in variability of the aggregated PV systems. Also the larger the aggregated system, the more the reduction in variability.

In chapter 4, a novel effort to explore a multi-mode and multi-droop settings of SIs (Volt-Watt, Volt VAR P-priority, Volt VAR Q-priority, constant power factor (leading and lagging) as part of a single OPF formulation, on the same feeder for effective voltage control and optimization. and finally proposes a two-stage OPF and two-stage HOPF which allow the SI mode, SI settings, OLTC/VR tap position and Caps status to be optimally determined on hourly basis while the optimal active and reactive power is dispatched on one-minute basis. The 2S-HOPF gives the highest priority of voltage control to the SI. The proposed formulation and algorithms are tested on the standard IEEE 123 test feeder. The results show the effectiveness and feasibility of proposed algorithms. This chapter also presented a multi-objective optimization technique for volt-var control with high PV penetration on the distribution feeder using genetic algorithm. This optimization was solved to minimize the distribution system losses while keeping the voltage of the nodes close to the lower threshold of the ANSI C84.1 standard. This was done to take the benefit of CVR into effect. The results shows the effectiveness of the technique in the use of CVR and also in minimizing the system losses. There are also some trade offs in keeping the voltage lower where the overall system losses was slightly increased beyond the normal value.

In chapter 5, A multiphysics-based and multi-objective optimization approach for HFT design is presented in this chapter. The variables of the optimization are the core parameters and the transformer number of turns. The core param-

eters dimension constraints were formulated in a way to ensure the feasibility of practical implementation. The proposed algorithm results show the optimal core parameters and winding number of turns based on the trade-offs between set objectives (efficiency, cost and power density). The core sizes were defined a way to allow practical implementation based on of-the-shelf core dimensions. From the POS, a case study of two HFTs, namely  $HFT_1$  and  $HFT_2$  were investigated and implemented. The multiphysics results presented show the coupling between electromagnetic, thermal and fluid models of the HFTs. The experimental implementation of  $HFT_1$  and  $HFT_2$  shows a good agreement between the optimization results and the experimental values. At low power level, the efficiencies of the HFTs were 97% for  $HFT_1$  and 90% for  $HFT_2$  with high values of efficiencies expected when loaded at rated power.

In chapter 6, Highly efficient and cost effective SSTs are desirable for future deployment on distribution and transmission feeders. Direct AC-AC MC-based SSTs are promising candidates due to the absence of an intermediate DC link which necessitates the use of DC link capacitors. For resonant MC-based SSTs, achieving high efficiency, cost effectiveness, self-tuning and soft switching become highly imperative. This chapter proposed a simplified logic based controller for the converter switches and a physics based design optimization algorithm for the SST's HFT. The results showed that the proposed logic based controller can achieve soft switching at various loading conditions, automatically tune itself based on the variation in resonant frequency as well as bidirectionally transfer power between the primary and secondary converters. The proposed HFT optimization algorithm will allow designers to analyze the various trade-offs in the design objectives and select the right parameters for the HFT.

In chapter 7, A voltage controller for a series resonant DC/DC converter is proposed in this chapter for solid state transformer applications. The proposed controller is based regulating the quantum energy injection/regeneration using

the resonant current of the converter and the output voltage error. The controller enable soft switching across the four switches of the primary converter. The proposed controller was developed using logic gates with simulation performed on MATLAB/Simulink. The resonant current in LLC tank can be effectively regulated to achieve the desired reference output voltage. This was verified through simulation and validated through experimental results.

## 8.1 Future work

The following areas are suggested for future works in relation to the research presented in this thesis:

1. Data-driven PV aggregation analysis and OPF Solving voltage-frequency control and optimization algorithms (based on my early studies) for distribution feeders is highly computationally expensive with increasing grid-tied RES. The control setpoints and operational droop settings has to be sent via communication channels at specified time internals based on the solution of these algorithms. In this work, developing machine learning algorithms that will be trained with several droop models and functions of PV-SIs and the corresponding feeder performance parameters and models. The developed ML model can be used to predict the feeder voltage, frequency and other power quality parameters without necessarily solving a new optimization algorithm. Thereby easing need for expensive servers, and frequent communication with the PV-SIs. The developed models can also be programed on the SIs microcontrollers thereby allow for more autonomous control for the PV-SIs.
2. Enhancing the Speed of Physics-Based Multi-Objective Optimization Using Parallel Processing. The developed physics-based multi-objective optimization of magnetic structures is highly effective for obtaining optimal structures. The only drawback of this method is the optimization time.

However, using parallel processing the optimization can be performed in a much shorter time. This can be achieved by performing the 2D or 3D FEAs for individuals at the same time.

3. Development of Direct Current-fed AC-AC Converters Topologies With Built-in Power Factor Correction. The AC-AC converter which are developed in this thesis require the use of power filters to current and voltage harmonic mitigation and power factor improvement. The development of direct AC-AC Converters topologies with built-in power factor correction are suggested as a future work. This can be achieved developing current-fed matrix converter topologies. The current-fed matrix converters can be developed by adding input inductors to the topology and modifying the developed switching mechanism to cope with new inductive elements. These types of converters are expected inherently have low current harmonics to be more compact.



## BIBLIOGRAPHY

- [1] US Energy Information Administration, “Top 10 net solar photovoltaic generation from utility and small scale, Year-to-Date through June 2017 (Thousand Megawatthours),” 2017. [Online]. Available: <https://www.eia.gov/electricity/monthly/epm{-}table{-}grapher.php?t=epmt{-}1{-}17{-}b>
- [2] Wells and Peggy, “Wind and Solar Data and Projections from the U.S. Energy Information Administration: Past Performance and Ongoing Enhancements,” *U.S. Energy Inf. Adm.*, no. March, 2016. [Online]. Available: <https://www.eia.gov/outlooks/aeo/supplement/renewable/pdf/projections.pdf>
- [3] J. Giraldez, M. Emmanuel, A. Hoke, and S. Suryanarayanan, “Impacts of voltage-based grid support functions on energy production of pv customers,” in *Proc. 2019 IEEE Power Energy Society General Meeting (PESGM)*, 2019, pp. 1–5.
- [4] S. Ghosh and S. Rahman, “Global deployment of solar photovoltaics: Its opportunities and challenges,” *IEEE PES Innov. Smart Grid Technol. Conf. Eur.*, pp. 1–6, 2017.
- [5] U.S. Department of Energy Office of Energy Efficiency & Renewable Energy Solar Energy Technologies Program Systems Integration Subprogram, “High penetration of photovoltaic (pv) systems into the distribution grid,” U.S. department of Energy, Tech. Rep., 2009.
- [6] T. Olowu, A. Sundararajan, M. Moghaddami, and A. Sarwat, “Future challenges and mitigation methods for high photovoltaic penetration: A survey,” *Energies*, vol. 11, no. 7, p. 1782, 2018.
- [7] K. Klima, J. Apt, M. Bandi, P. Happy, C. Loutan, and R. Young, “Geographic smoothing of solar photovoltaic electric power production in the western usa,” *Journal of Renewable and Sustainable Energy*, vol. 10, no. 5, p. 053504, 2018.
- [8] M. Chamana, B. H. Chowdhury, and F. Jahanbakhsh, “Distributed control of voltage regulating devices in the presence of high pv penetration to mitigate ramp-rate issues,” *IEEE Transactions on Smart Grid*, vol. PP, no. 99, pp. 1–1, 2017.
- [9] S. R. Abate, T. E. McDermott, M. Rylander, and J. Smith, “Smart inverter settings for improving distribution feeder performance,” in *2015 IEEE Power Energy Society General Meeting*, July 2015, pp. 1–5.
- [10] T. O. Olowu, M. Jafari, and A. I. Sarwat, “A multi-objective optimization technique for volt-var control with high pv penetration using genetic algo-

- rithm,” in *2018 North American Power Symposium (NAPS)*, Sep. 2018, pp. 1–6.
- [11] M. Jafari, T. O. Olowu, and A. I. Sarwat, “Optimal smart inverters volt-var curve selection with a multi-objective volt-var optimization using evolutionary algorithm approach,” in *2018 North American Power Symposium (NAPS)*, Sep. 2018, pp. 1–6.
- [12] H. Chen and D. Divan, “Design of a 10-kv·a soft-switching solid-state transformer (s4t),” *IEEE Transactions on Power Electronics*, vol. 33, no. 7, pp. 5724–5738, July 2018.
- [13] —, “Soft-switching solid-state transformer (s4t),” *IEEE Transactions on Power Electronics*, vol. 33, no. 4, pp. 2933–2947, April 2018.
- [14] A. Murata, H. Yamaguchi, and K. Otani, “A method of estimating the output fluctuation of many photovoltaic power generation systems dispersed in a wide area,” *Electrical Engineering in Japan (English translation of Denki Gakkai Ronbunshi)*, vol. 166, no. 4, pp. 9–19, 2009.
- [15] T. E. Hoff and R. Perez, “Quantifying PV power Output Variability,” *Solar Energy*, vol. 84, no. 10, pp. 1782–1793, 2010. [Online]. Available: <http://dx.doi.org/10.1016/j.solener.2010.07.003>
- [16] M. S. Lave, “Analyzing and simulating the variability of solar irradiance and solar pv powerplants,” Ph.D. dissertation, UC San Diego, 2012.
- [17] M. Lave and J. Kleissl, “Solar variability of four sites across the state of Colorado,” *Renewable Energy*, vol. 35, no. 12, pp. 2867–2873, 2010. [Online]. Available: <http://dx.doi.org/10.1016/j.renene.2010.05.013>
- [18] —, “Optimum fixed orientations and benefits of tracking for capturing solar radiation in the continental United States,” *Renewable Energy*, vol. 36, no. 3, pp. 1145–1152, 2011. [Online]. Available: <http://dx.doi.org/10.1016/j.renene.2010.07.032>
- [19] M. Lave, J. Kleissl, and E. Arias-Castro, “High-frequency irradiance fluctuations and geographic smoothing,” *Solar Energy*, vol. 86, no. 8, pp. 2190–2199, 2012.
- [20] M. Lave and J. Kleissl, “Cloud speed impact on solar variability scaling - Application to the wavelet variability model,” *Solar Energy*, vol. 91, pp. 11–21, 2013. [Online]. Available: <http://dx.doi.org/10.1016/j.solener.2013.01.023>
- [21] M. Lave, J. Kleissl, and J. S. Stein, “A wavelet-based variability model (WVM) for solar PV power plants,” *IEEE Transactions on Sustainable Energy*, vol. 4, no. 2, pp. 501–509, 2013.

- [22] Electric Power Research Institute (EPRI), “Common Functions for Smart Inverters: 4th Edition,” p. 170, 2016. [Online]. Available: <https://www.epri.com/{#}/pages/product/000000003002008217/>
- [23] National Renewable Energy Laboratory (NREL), “Advanced Inverter Functions To Support High Levels Of Distributed Solar ,” *NREL Technical Report NREL/TP-5200-57991*, pp. 1–8, 2013.
- [24] X. Zhao, L. Chang, R. Shao, and K. Spence, “Power system support functions provided by smart inverters—a review,” *CPSS Transactions on Power Electronics and Applications*, vol. 3, no. 1, pp. 25–35, March 2018.
- [25] A. Nelson, A. Nagarajan, K. Prabakar, V. Gevorgian, B. Lundstrom, S. Nepal, A. Hoke, M. Asano, R. Ueda, J. Shindo *et al.*, “Hawaiian electric advanced inverter grid support function laboratory validation and analysis,” National Renewable Energy Lab.(NREL), Golden, CO (United States), Tech. Rep., 2016.
- [26] X. She, A. Q. Huang, and R. Burgos, “Review of solid-state transformer technologies and their application in power distribution systems,” *IEEE Journal of Emerging and Selected Topics in Power Electronics*, vol. 1, no. 3, pp. 186–198, 2013.
- [27] X. She, R. Burgos, G. Wang, F. Wang, and A. Q. Huang, “Review of solid state transformer in the distribution system: From components to field application,” *2012 IEEE Energy Conversion Congress and Exposition, ECCE 2012*, pp. 4077–4084, 2012.
- [28] K. V. Autkar and S. Dhamse, “Solid state transformer for doubly fed induction generator based wind energy conversion system: A review,” in *2018 International Conference on Computation of Power, Energy, Information and Communication (ICCPEIC)*. IEEE, 2018, pp. 129–134.
- [29] Y. P. Chang, “Optimal the tilt angles for photovoltaic modules in Taiwan,” *Int. J. Electr. Power Energy Syst.*, vol. 32, no. 9, pp. 956–964, 2010. [Online]. Available: <http://dx.doi.org/10.1016/j.ijepes.2010.02.010>
- [30] M. Oshiro, K. Tanaka, T. Senjyu, S. Toma, A. Yona, A. Y. Saber, T. Funabashi, and C.-H. Kim, “Optimal voltage control in distribution systems using PV generators,” *Int. J. Electr. Power Energy Syst.*, vol. 33, no. 3, pp. 485–492, 2011. [Online]. Available: <http://linkinghub.elsevier.com/retrieve/pii/S0142061510001997>
- [31] H. Setiadi, A. U. Krismanto, N. Mithulananthan, and M. J. Hossain, “Modal interaction of power systems with high penetration of renewable energy and BES systems,” *Int. J. Electr. Power Energy Syst.*, vol. 97, no. June 2017, pp. 385–395, 2018. [Online]. Available: <https://doi.org/10.1016/j.ijepes.2017.11.021>

- [32] APS Panel and Public affairs, “Integrating Renewable Electricity on the Grid A Report by the APS Panel on Public Affairs,” *Leadership*, pp. 1–38, 2010.
- [33] H. Alatrash, R. A. Amarin, and C. Lam, “Enabling large-scale PV integration into the grid,” *2012 IEEE Green Technol. Conf.*, no. Lv, 2012.
- [34] A. Anzalchi and A. Sarwat, “Overview of technical specifications for grid-connected photovoltaic systems,” *Energy Conversion and Management*, vol. 152, pp. 312 – 327, 2017. [Online]. Available: <http://www.sciencedirect.com/science/article/pii/S0196890417308737>
- [35] A. D. Suma Jothibasur and S. Santoso, “The Full Cost of Electricity ( FCE ) Integrating Photovoltaic Generation,” *Integr. Photovolt. Gener.*, 2016.
- [36] H. Jain, B. Palmintier, I. Krad, and D. Krishnamurthy, “Studying the impact of distributed solar pv on power systems using integrated transmission and distribution models,” in *2018 IEEE/PES Transmission and Distribution Conference and Exposition (T&D)*. IEEE, 2018, pp. 1–5.
- [37] B. Palmintier, R. Broderick, B. Mather, M. Coddington, K. Baker, F. Ding, M. Reno, M. Lave, and A. Bharatkumar, “On the Path to SunShot: Emerging Issues and Challenges in Integrating Solar with the Distribution System,” *Nrel/Tp-5D00-6533, Sand2016-2524 R*, no. May, 2016. [Online]. Available: <http://www.nrel.gov/docs/fy16osti/65331.pdf>
- [38] J. V. Appen, M. Braun, T. Stetz, K. Diwold, and D. Geibel, “Time in the sun: The challenge of high pv penetration in the german electric grid,” *IEEE Power and Energy Magazine*, vol. 11, no. 2, pp. 55–64, March 2013.
- [39] Y.-K. Wu, Y. Guan-Ting, and M. Shaaban, “Impact analysis of large pv integration: Case studies in taiwan,” in *2016 IEEE/IAS 52nd Industrial and Commercial Power Systems Technical Conference (I CPS)*, May 2016, pp. 1–10.
- [40] A. Rodriguez-Calvo, R. Cossent, and P. Frías, “Integration of PV and EVs in unbalanced residential LV networks and implications for the smart grid and advanced metering infrastructure deployment,” *Int. J. Electr. Power Energy Syst.*, vol. 91, pp. 121–134, 2017. [Online]. Available: <http://dx.doi.org/10.1016/j.ijepes.2017.03.008>
- [41] M. Patsalides, A. Stavrou, V. Efthymiou, and G. E. Georghiou, “Towards the establishment of maximum PV generation limits due to power quality constraints,” *Int. J. Electr. Power Energy Syst.*, vol. 42, no. 1, pp. 285–298, 2012. [Online]. Available: <http://dx.doi.org/10.1016/j.ijepes.2012.03.043>
- [42] A. Hoke, R. Butler, J. Hambrick, and B. Kroposki, “Maximum Photovoltaic Penetration Levels on Typical Distribution Feeders,” *IEEE Trans. Sustain. Energy*, no. July, 2012.

- [43] L. Mukwekwe, C. Venugopal, and I. E. Davidson, "A review of the impacts and mitigation strategies of high pv penetration in low voltage networks," in *2017 IEEE PES PowerAfrica*, June 2017, pp. 274–279.
- [44] D. Cheng, B. A. Mather, R. Seguin, J. Hambrick, and R. P. Broadwater, "Photovoltaic (pv) impact assessment for very high penetration levels," *IEEE Journal of photovoltaics*, vol. 6, no. 1, pp. 295–300, 2015.
- [45] G. Yang, F. Marra, M. Juamperez, S. B. Kjaer, S. Hashemi, J. Østergarrd, H. H. Ipsen, and K. H. Fredriksen, "Voltage rise mitigation for solar PV integration at LV grids: Studies from PVNET. dk," *J. Mod. Power Syst. Clean Energy*, vol. 3, no. 3, pp. 411–421, 2015.
- [46] M. Coddington, B. Kroposki, T. Basso, K. Lynn, C. Herig, and W. Bower, "High-Penetration Photovoltaic Standards and Codes Workshop," *NREL/Tp-550-48378*, pp. 1–120, 2010.
- [47] J. H. R. Enslin, "Network Impacts of High Penetration of Photovoltaic Solar Power Systems," *IEEE PES Gen. Meet.*, pp. 1–5, 2010. [Online]. Available: <http://ieeexplore.ieee.org/document/5589675/>
- [48] J. Bank, B. Mather, J. Keller, and M. Coddington, "High penetration photovoltaic case study report," National Renewable Energy Lab.(NREL), Golden, CO (United States), Tech. Rep., 2013.
- [49] J. Bebic, "Power system planning: emerging practices suitable for evaluating the impact of high-penetration photovoltaics," National Renewable Energy Laboratory (NREL), Golden, CO., Tech. Rep., 2008.
- [50] D. McPhail, B. Croker, and B. Harvey, "A study of solar PV saturation limits for representative low voltage networks," *Proc. 2016 Australas. Univ. Power Eng. Conf. AUPEC 2016*, pp. 0–5, 2016.
- [51] A. Anzalchi, A. Sundararajan, A. Moghadasi, and A. Sarwat, "Power quality and voltage profile analyses of high penetration grid-tied photovoltaics: A case study," in *2017 IEEE Industry Applications Society Annual Meeting*, Oct 2017, pp. 1–8.
- [52] J. Weiss, "Solar Energy Support in Germany. A Closer Look," *Sol. Energy Ind. Assoc.*, no. July, 2014. [Online]. Available: <http://www.seia.org/research-resources/solar-energy-support-germany-closer-look>
- [53] S. Lewis, "Carnarvon: A case study of increasing levels of pv penetration in an isolated electricity supply system," *UNSW Centre for Energy and Environmental Markets for the Austr PV Assoc*, 2012.

- [54] P. Denholm and R. Margolis, “Energy Storage Requirements for Achieving 50 % Solar Photovoltaic Energy Penetration in California,” *NREL*, no. August, 2016.
- [55] D. Steen, “Integrating Solar and Wind Into the Electricity Grid,” *Syst. Perspect. Renew. Power*, pp. 94–107, 2014.
- [56] M. Baquedano-Aguilar, D. Colomé, E. Agüero, and M. Molina, “Impact of increased penetration of large-scale pv generation on short-term stability of power systems,” in *2016 IEEE 36th Central American and Panama Convention (CONCAPAN XXXVI)*. IEEE, 2016, pp. 1–6.
- [57] E. Stewart, J. MacPherson, S. Vasilic, D. Nakafuji, and T. Aukai, “Analysis of high-penetration levels of photovoltaics into the distribution grid on oahu, hawaii: Detailed analysis of heco feeder wf1,” National Renewable Energy Laboratory (NREL), Golden, CO., Tech. Rep., 2013.
- [58] European Photovoltaic Industry Association, “Connecting the sun - solar photovoltaics on the road to large scale grid integration,” European Photovoltaic Industry Association, Tech. Rep., 2008.
- [59] N. Phuangpornpitak and S. Tia, “Opportunities and challenges of integrating renewable energy in smart grid system,” *Energy Procedia*, vol. 34, no. Supplement C, pp. 282 – 290, 2013, 10th Eco-Energy and Materials Science and Engineering Symposium. [Online]. Available: <http://www.sciencedirect.com/science/article/pii/S1876610213009995>
- [60] M. Ding, Z. Xu, W. Wang, X. Wang, Y. Song, and D. Chen, “A review on china’s large-scale pv integration: Progress, challenges and recommendations,” *Renewable and Sustainable Energy Reviews*, vol. 53, pp. 639–652, 2016.
- [61] R. Shah, N. Mithulananthan, R. C. Bansal, and V. K. Ramachandaramurthy, “A review of key power system stability challenges for large-scale PV integration,” *Renew. Sustain. Energy Rev.*, vol. 41, pp. 1423–1436, 2015. [Online]. Available: <http://dx.doi.org/10.1016/j.rser.2014.09.027>
- [62] H. Mortazavi, H. Mehrjerdi, M. Saad, S. Lefebvre, D. Asber, and L. Lenoir, “A Monitoring Technique for Reversed Power Flow Detection with High PV Penetration Level,” *IEEE Trans. Smart Grid*, vol. 6, no. 5, pp. 2221–2232, 2015.
- [63] S. Lewis, “Analysis and management of the impacts of a high penetration of photovoltaic systems in an electricity distribution network,” *Innov. Smart Grid Technol. Asia*, no. June 2010, pp. 1–7, 2011. [Online]. Available: [http://ieeexplore.ieee.org/xpls/abs/\\_all.jsp?arnumber=6257068](http://ieeexplore.ieee.org/xpls/abs/_all.jsp?arnumber=6257068)
- [64] O. Poosri and C. Charoenlarnpparut, “Harmonics Impact of Rooftop

- Photovoltaic Penetration Level on Low Voltage Distribution System,” *Int. J. Electron. Electr. Eng.*, vol. 4, no. 3, pp. 221–225, 2016. [Online]. Available: <http://www.ijeee.net/index.php?m=content{&c=index{&a=show{&catid=62{&id=279>
- [65] L. H. Ketut Dartawan, Ricardo Austria and M. Suehiro, “Harmonic Issues That Limit Solar Photovoltaic,” *World Renew. Energy Forum 2012*, pp. 1–7, 2013. [Online]. Available: <https://ases.conference-services.net/resources/252/2859/pdf/SOLAR2012{-}0482{-}fullpaper.pdf>
- [66] A. F. A. Kadir, T. Khatib, and W. Elmenreich, “Integrating Photovoltaic Systems in Power System: Power Quality Impacts and Optimal Planning Challenges,” *Int. J. Photoenergy*, vol. 2014, 2014.
- [67] Y. Tang and R. Ayyanar, “Methodology of Automated Protection Analysis for Large Distribution Feeders With High Penetration of Photovoltaic Systems,” *IEEE Power Energy Technol. Syst. J.*, vol. 4, no. 1, pp. 1–9, 2017. [Online]. Available: <http://ieeexplore.ieee.org/document/7493637/>
- [68] Z. Ziadi, S. Taira, M. Oshiro, and T. Funabashi, “Optimal power scheduling for smart grids considering controllable loads and high penetration of photovoltaic generation,” *IEEE Trans. Smart Grid*, vol. 5, no. 5, pp. 2350–2359, 2014.
- [69] D. Taggart, K. Hao, R. Jenkins, and R. VanHatten, “Power factor control for grid-tied photovoltaic solar farms,” in *proceedings of the 14th Annual Western Power Delivery Automation Conference, Spokane, WA*, 2012.
- [70] P.-J. Alet, B. Bletterie, A. Goršek, A. Abart, M. Heidl, F. Baccaro, M. D. Felice, V. Efthymiou, C. Mayr, G. Graditi, M. Juel, D. Moser, M. Petitta, S. Tselepis, and G. Yang, “Quantification, challenges and outlook of pv integration in the power system: a review by the european pv technology platform a,” *31st Eur. Photovolt. Sol. Energy Conf. 2015*, no. February 2016, pp. 2937–2943, 2011.
- [71] B. F. Katiraei, “Studies for Utility-Scale Photovoltaic Distributed Generation,” *Ieee Power Energy Mag.*, vol. 9, no. 3, pp. 62–71, 2011. [Online]. Available: <http://ieeexplore.ieee.org/xpl/freeabs{-}all.jsp?arnumber=5753332>
- [72] M. Ebad and W. M. Grady, “An approach for assessing high-penetration PV impact on distribution feeders,” *Electr. Power Syst. Res.*, vol. 133, pp. 347–354, apr 2016. [Online]. Available: <http://linkinghub.elsevier.com/retrieve/pii/S0378779615004034>
- [73] G. Xu, W. Yu, D. Griffith, N. Golmie, and P. Moulema, “Toward Integrating Distributed Energy Resources and Storage Devices in Smart Grid,” *IEEE Internet Things J.*, vol. 4, no. 1, pp. 192–204, 2017.

- [74] R. Tonkoski, D. Turcotte, and T. H. El-Fouly, "Impact of high pv penetration on voltage profiles in residential neighborhoods," *IEEE Transactions on Sustainable Energy*, vol. 3, no. 3, pp. 518–527, 2012.
- [75] W. E. Ibraheem, C. K. Gan, and M. R. A. Ghani, "Impact of Photovoltaic (PV) Systems on Distribution Networks," *Int. Rev. Model. Simul.*, vol. 2, no. 4604, pp. 70–74, 2014.
- [76] A. N. Azmi, I. N. Dahlberg, M. L. Kolhe, and A. G. Imenes, "Impact of increasing penetration of photovoltaic (pv) systems on distribution feeders," in *2015 International Conference on Smart Grid and Clean Energy Technologies (ICSGCE)*. iee, 2015, pp. 70–74.
- [77] K. Hao, S. Achanta, B. Rowland, and A. Kivi, "Mitigating the impacts of photovoltaics on the power system," *2016 Saudi Arab. Smart Grid Conf. SASG 2016*, no. April 2016, 2017.
- [78] M. Cohen, P. Kauzmann, and D. Callaway, "Economic effect of distributed pv generation on california's distribution system," *Energy Institute at Haas*, 2015.
- [79] A. Anzalchi, M. M. Pour, and A. Sarwat, "A combinatorial approach for addressing intermittency and providing inertial response in a grid-connected photovoltaic system," in *2016 IEEE Power and Energy Society General Meeting (PESGM)*, July 2016, pp. 1–5.
- [80] D. Feldman, D. Boff, and D. R. Margolis, "Q3/Q4 2016 solar industry update," *U.S. Dep. Energy*, 2016. [Online]. Available: <https://www.nrel.gov/docs/fy17osti/67639.pdf>
- [81] M. J. Alam, K. M. Muttaqi, and D. Sutanto, "A novel approach for ramp-rate control of solar PV using energy storage to mitigate output fluctuations caused by cloud passing," *IEEE Trans. Energy Convers.*, vol. 29, no. 2, pp. 507–518, 2014.
- [82] A. Kankiewicz, D. Moon, and M. Sengupta, "Observed Impacts of Transient Clouds on Utility-Scale PV Fields," *ASES Natl. Sol. Conf.*, vol. 2009, no. December 2009, pp. 1–4, 2010. [Online]. Available: <http://proceedings.ases.org/wp-content/uploads/2014/02/2010-112.pdf>
- [83] I. G. E. Outlook, "Entering the decade of electric drive," 2020.
- [84] M. Amini and A. I. Sarwat, "Optimal reliability-based placement of plug-in electric vehicles in smart distribution network," *International Journal of Energy Science*, vol. 4, no. 2, 2014.
- [85] A. Gholami, M. Jamei, J. Ansari, and A. I. Sarwat, "Combined economic and emission dispatch incorporating renewable energy sources and plug-in



- hybrid electric vehicles,” *International Journal of Energy Science*, vol. 4, no. 2, 2014.
- [86] C. Cao, L. Wang, and B. Chen, “Mitigation of the impact of high plug-in electric vehicle penetration on residential distribution grid using smart charging strategies,” *Energies*, vol. 9, no. 12, 2016.
- [87] E. Alghsoon, A. Harb, and M. Hamdan, “Power Quality and Stability Impacts,” *8th Int. Renew. Energy Congr. (IREC 2017) Power*, no. Irec, 2017.
- [88] C. Wu, F. Wen, Y. Lou, and F. Xin, “Probabilistic load flow analysis of photovoltaic generation system with plug-in electric vehicles,” *Int. J. Electr. Power Energy Syst.*, vol. 64, pp. 1221–1228, 2015. [Online]. Available: <http://linkinghub.elsevier.com/retrieve/pii/S0142061514005651>
- [89] B. Memisevic, F. Masic, A. Bosovic, and M. Music, “Impact of plug-in electric vehicles and photovoltaic technologies on the power distribution network (case-study of a suburban medium-voltage network),” *Elektrotehniski Vestnik*, vol. 84, no. 3, p. 117, 2017.
- [90] R. M. Oviedo, Z. Fan, S. Gormus, and P. Kulkarni, “A residential PHEV load coordination mechanism with renewable sources in smart grids,” *Int. J. Electr. Power Energy Syst.*, vol. 55, pp. 511–521, 2014. [Online]. Available: <http://dx.doi.org/10.1016/j.ijepes.2013.10.002>
- [91] A. Gharaibeh, M. A. Salahuddin, S. J. Hussini, A. Khreishah, I. Khalil, M. Guizani, and A. Al-Fuqaha, “Smart Cities: A Survey on Data Management, Security and Enabling Technologies,” *IEEE Commun. Surv. Tutorials*, vol. X, no. X, pp. 1–1, 2017. [Online]. Available: <http://ieeexplore.ieee.org/document/8003273/>
- [92] M. Akcin, A. Kaygusuz, A. Karabiber, S. Alagoz, B. B. Alagoz, and C. Keles, “Opportunities for energy efficiency in smart cities,” *4th Int. Istanbul Smart Grid Congr. Fair, ICSG 2016*, no. April, 2016.
- [93] H. Larsen and L. Sønderberg Petersen, *Risø energy report 10 : Energy for smart cities in an urbanised world*, ser. Denmark. Forskningscenter Risoe. Risoe-R. Danmarks Tekniske Universitet, Risø Nationallaboratoriet for Bæredygtig Energi, 2011, no. 1778(EN).
- [94] J. Coughlin, J. Grove, L. Irvine, J. F. Jacobs, S. J. Phillips, L. Moynihan, and J. Wiedman, “A Guide to Community Solar: Utility, Private, and Non-Profit Development,” *U.S. Dep. Energy*, p. 56, 2010. [Online]. Available: <http://www.nrel.gov/docs/fy12osti/54570.pdf>
- [95] E. Ghiani, M. Garau, G. Celli, F. Pilo, and G. Marongiu, “Smart integration and aggregation of nanogrids: Benefits for users and DSO,” *2017 IEEE Manchester PowerTech*, pp. 1–6, 2017. [Online]. Available:

<http://ieeexplore.ieee.org/document/7981205/>

- [96] Z. Mošna, J. Boška, P. K. Knížová, T. Šindelářová, D. Kouba, J. Chum, L. Rejtek, K. Potužníková, F. Arikani, and C. Toker, “Observation of the solar eclipse of 20 march 2015 at the pruhonice station,” *Journal of Atmospheric and Solar-Terrestrial Physics*, vol. 171, pp. 277–284, 2018.
- [97] K. Burges, M. Döring, R. Kuwahata, U. Bachmann, and R. Sikora, “Operating Power Systems with high Photovoltaic Generation during a Solar Eclipse Challenges and Operational Measures,” *4th Sol. Integr. Work.*, 2014.
- [98] R. Fritz, “How an energy supply system with a high pv share handled a solar eclipse,” *International Energy Agency Photovoltaic Power Systems Programme: Kassel, Germany*, pp. 1–18, 2016.
- [99] K. Maslo, “Impact of Photovoltaics on Frequency Stability of Power System during Solar Eclipse,” *IEEE Trans. Power Syst.*, vol. 31, no. 5, pp. 3648–3655, 2016.
- [100] N. A. E. R. Corporation, “A Wide-Area Perspective on the August 21 , 2017 Total Solar Eclipse,” NERC, Tech. Rep., 04 2017.
- [101] U.S. Energy Information Administration, “Solar eclipse on August 21 will affect photovoltaic generators across the country- Today in Energy - US,” 2017. [Online]. Available: <https://www.eia.gov/todayinenergy/detail.php?id=32372>
- [102] Wikipedia, “Solar eclipse of April 8, 2024,” 2017. [Online]. Available: [https://en.wikipedia.org/wiki/Solar\\_eclipse\\_of\\_April\\_8,\\_2024](https://en.wikipedia.org/wiki/Solar_eclipse_of_April_8,_2024)
- [103] NASA, “Nasa - solar eclipses: 2021 - 2030,” 2013. [Online]. Available: <https://eclipse.gsfc.nasa.gov/SEdecade/SEdecade2021.html>
- [104] GWAC, “GridWise Transactive Energy Framework Draft Version,” *Grid-Wise Archit. Counc. Trans. Energy*, vol. 1, pp. 1–23, 2013.
- [105] Z. Liu, Q. Wu, S. Huang, and H. Zhao, “Transactive energy: A review of state of the art and implementation,” *2017 IEEE Manchester PowerTech*, pp. 1–6, 2017. [Online]. Available: <http://ieeexplore.ieee.org/document/7980892/>
- [106] T. Sahin and D. Shereck, “Renewable energy sources in a transactive energy market,” in *The 2014 2nd International Conference on Systems and Informatics (ICSAI 2014)*. IEEE, 2014, pp. 202–208.
- [107] M. Coddington, B. Kroposki, T. Basso, K. Lynn, D. Sammon, and T. Yohn, “Photovoltaic Systems Interconnected onto Secondary Network Distribution Systems – Success Stories Photovoltaic Systems Interconnected onto

Secondary Network Distribution Systems – Success Stories,” *Contract*, no. May 2015, 2009.

- [108] M. Coddington, “Session 9: Photovoltaic System Case Studies And Electric Distribution Planning for DER,” *International Smart Grid Action Network*, 2015.
- [109] M. M. Aman, G. Bin Jasmon, H. Bin Mokhlis, Q. A. Khan, A. H. B. A. Bakar, and M. Karimi, “Modeling and simulation of digital frequency relay for generator protection,” *PECon 2012 - 2012 IEEE International Conference on Power and Energy*, no. June, pp. 701–706, 2012.
- [110] Y. Xue and J. M. Guerrero, “Smart inverters for utility and industry applications,” in *Proceedings of PCIM Europe 2015; International Exhibition and Conference for Power Electronics, Intelligent Motion, Renewable Energy and Energy Management*, 2015, pp. 1–8.
- [111] R. J. Nigel, “Integration of network protector relays on downtown distribution networks with penetration of renewable energy,” Master’s thesis, Louisiana State University, 2014.
- [112] R. Mack, M. Sakib, and S. Succar, “Impacts of substation transformer back-feed at high pv penetrations,” in *2017 IEEE Power Energy Society General Meeting*, July 2017, pp. 1–5.
- [113] IEEE Standards Coordinating Committee 21, “IEEE standard for interconnection and interoperability of distributed energy resources with associated electric power systems interfaces,” *IEEE Std 1547-2018 (Revision of IEEE Std 1547-2003)*, pp. 1–138, April 2018.
- [114] S. D. Patil, S. G. Kadwane, and S. P. Gawande, “Current Control of Grid Tied Inverter through SHEPWM Method,” *Energy Procedia*, vol. 117, pp. 643–650, 2017. [Online]. Available: <http://dx.doi.org/10.1016/j.egypro.2017.05.166>
- [115] H. Li, C. Wen, K.-H. Chao, and L.-L. Li, “Research on Inverter Integrated Reactive Power Control Strategy in the Grid-Connected PV Systems,” *Energies*, vol. 10, no. 7, p. 912, 2017. [Online]. Available: <http://www.mdpi.com/1996-1073/10/7/912>
- [116] H. Jafarian, N. Kim, B. Parkhideh, and J. Enslin, “Analysis of smart inverter functions of decentralized grid-connected AC-stacked PV inverter architecture,” *Conference Proceedings - IEEE Applied Power Electronics Conference and Exposition - APEC*, pp. 3594–3600, 2017.
- [117] G. Todeschini, “Control and derating of a pv inverter for harmonic compensation in a smart distribution system,” in *2017 IEEE Power Energy Society General Meeting*, July 2017, pp. 1–5.

- [118] E. Ozdemir, S. Ozdemir, K. Erhan, and A. Aktas, “Energy storage technologies opportunities and challenges in smart grids,” in *2016 International Smart Grid Workshop and Certificate Program (ISGWCP)*. IEEE, 2016, pp. 1–6.
- [119] H. Zhou, T. Bhattacharya, D. Tran, T. S. T. Siew, and A. M. Khambadkone, “Composite energy storage system involving battery and ultracapacitor with dynamic energy management in microgrid applications,” *IEEE Transactions on Power Electronics*, vol. 26, no. 3, pp. 923–930, 2011.
- [120] R. Blonbou, S. Monjoly, and J.-L. Bernard, “Dynamic energy storage management for dependable renewable electricity generation,” in *Energy Storage*, A. F. Zobaa, Ed. Rijeka: InTech, 2013, ch. 11. [Online]. Available: <https://doi.org/10.5772/52411>
- [121] S. F. Pinto, P. V. Mendes, and J. Fernando Silva, “Modular Matrix Converter Based Solid State Transformer for smart grids,” *Electric Power Systems Research*, vol. 136, pp. 189–200, 2016.
- [122] A. Al-Hafri, H. Ali, A. Ghias, and Q. Nasir, “Transformer-less based solid state transformer for intelligent power management,” *5th International Conference on Electronic Devices, Systems and Applications (ICEDSA)*, no. 1, pp. 1–4, 2016. [Online]. Available: <http://ieeexplore.ieee.org/document/7818507/>
- [123] F. Vaca-Urbano and M. S. Alvarez-Alvarado, “Power quality with solid state transformer integrated smart-grids,” *2017 IEEE PES Innovative Smart Grid Technologies Conference - Latin America, ISGT Latin America 2017*, vol. 2017-January, pp. 1–6, 2017.
- [124] W. Yu, “Solid State Transformer For Power Distribution Applications,” *U.S Department of Energy*, 2017.
- [125] J. W. Van Der Merwe and H. Du, “The solid-state transformer concept: A new era in power distribution,” *IEEE AFRICON Conference*, 2009.
- [126] J. S. Hong and M. Kim, “Game-Theory-Based Approach for Energy Routing in a Smart Grid Network,” *Journal of Computer Networks and Communications*, vol. 2016, 2016.
- [127] P. H. Nguyen, W. L. Kling, G. Georgiadis, M. Papatriantafillou, L. A. Tuan, and L. Bertling, “Distributed routing algorithms to manage power flow in agent-based active distribution network,” *IEEE PES Innovative Smart Grid Technologies Conference Europe, ISGT Europe*, pp. 1–7, 2010.
- [128] Y. Kado, D. Shichijo, K. Wada, and K. Iwatsuki, “Multiport power router and its impact on future smart grids,” *Radio Science*, vol. 51, no. 7, pp. 1234–1246, 2016.

- [129] K. Hayashi, R. Kato, R. Torii, H. Taoka, and R. Abe, “Bi-directional power flow through a digital grid router,” *Journal of International Council on Electrical Engineering*, vol. 5, no. 1, pp. 42–46, 2015. [Online]. Available: <http://www.tandfonline.com/doi/full/10.1080/22348972.2015.1068511>
- [130] Y. Liu, Y. Fang, and J. Li, “Interconnecting microgrids via the energy router with smart energy management,” *Energies*, vol. 10, no. 9, 2017.
- [131] A. Kordonis, R. Takahashi, and T. Hikihara, “AC/AC converter towards power routing systems in smart-grids: Advantage on operation by nonlinear dynamics,” *2013 IEEE 2nd Global Conference on Consumer Electronics, GCCE 2013*, no. May 2014, pp. 158–159, 2013.
- [132] Y. Xu, J. Zhang, W. Wang, A. Juneja, and S. Bhattacharya, “Energy router: Architectures and functionalities toward energy internet,” *2011 IEEE International Conference on Smart Grid Communications, SmartGridComm 2011*, pp. 31–36, 2011.
- [133] Q. Zhu, D. Wei, and T. Basar, “Secure routing in smart grids,” in *Workshop on Foundations of Dependable and Secure Cyber-Physical Systems (FD-SCPS)*, 2011, pp. 55–59.
- [134] J. Wang, Q. OU, and H. Shen, “An overview of smart grid routing algorithms,” in *AIP Conference Proceedings*, vol. 1864, no. 1. AIP Publishing, 2017, p. 020098.
- [135] J. Lin, W. Yu, X. Yang, G. Xu, and W. Zhao, “On false data injection attacks against distributed energy routing in smart grid,” *Proceedings - 2012 IEEE/ACM 3rd International Conference on Cyber-Physical Systems, IC-CPS 2012*, pp. 183–192, 2012.
- [136] R. Lee, *Software Engineering, Artificial Intelligence, Networking and Parallel/Distributed Computing*. Springer, 2009, vol. 209. [Online]. Available: <http://link.springer.com/10.1007/978-3-642-01203-7>
- [137] A. S. Meliopoulos, E. Polymeneas, Z. Tan, R. Huang, and D. Zhao, “Advanced distribution management system,” *IEEE Transactions on Smart Grid*, vol. 4, no. 4, pp. 2109–2117, 2013.
- [138] D. E. McNair, D. J. Phelan, and L. Coleman, “Voices of Experience: Insights into Advanced Distribution Management Systems,” *DoE*, no. 159, 2015. [Online]. Available: <http://energy.gov/oe/downloads/voices-experience-insights-advanced-distribution-management-systems>
- [139] N. Goel and M. Agarwal, “Smart grid networks: A state of the art review,” *2015 International Conference on Signal Processing and Communication (ICSC)*, pp. 122–126, 2015. [Online]. Available: <http://ieeexplore.ieee.org/lpdocs/epic03/wrapper.htm?arnumber=7150632>

- [140] Schneider Electric, “Creating a Reliable and Secure Advanced Distribution Management System,” *White Paper*, 2014.
- [141] M. E. Aljahani, “An enhanced self-healing protection system in smart grid: using advanced and intelligent devices and applying hierarchical routing in sensor network technique,” Master’s thesis, Western Michigan University, 2014.
- [142] S. Voima, H. Laaksonen, and K. Kauhaniemi, “Adaptive protection scheme for smart grids,” *Developments in Power System Protection (DPSP 2014), 12th IET International Conference on*, pp. 1–6, 2014. [Online]. Available: <http://bibliotecavirtual.ups.edu.ec:2065/ielx7/6819621/6809516/06822947.pdf?tp={&}arnumber=6822947{&}isnumber=6809516{&}5Cnhttp://bibliotecavirtual.ups.edu.ec:2065/xpls/abs{-}all.jsp?arnumber=6822947>
- [143] K. Kauhaniemi and S. Voima, “Adaptive relay protection concept for smart grids,” in *Renewable Efficient Energy II Conference*, 2012, pp. 1–10.
- [144] V. A. Papaspiliotopoulos, G. N. Korres, and N. D. Hatziaargyriou, “Protection coordination in modern distribution grids integrating optimization techniques with adaptive relay setting,” *2015 IEEE Eindhoven PowerTech, PowerTech 2015*, no. 308755, 2015.
- [145] S. Grillo, M. Bertolo, and E. Ragaini, “Adaptive protection algorithms for smart distribution systems: Hardware-in-the-loop testing and validation,” in *2018 IEEE International Conference on Environment and Electrical Engineering and 2018 IEEE Industrial and Commercial Power Systems Europe (EEEIC/I&CPS Europe)*. IEEE, 2018, pp. 1–6.
- [146] Y. Ates, A. Boynuegri, M. Uzunoglu, A. Nadar, R. Yumurtacı, O. Erdinc, N. Paterakis, and J. Catalão, “Adaptive Protection Scheme for a Distribution System Considering Grid-Connected and Islanded Modes of Operation,” *Energies*, vol. 9, no. 5, p. 378, 2016. [Online]. Available: <http://www.mdpi.com/1996-1073/9/5/378>
- [147] A. Hussain and H. M. Kim, “A hybrid framework for adaptive protection of microgrids based on IEC 61850,” *International Journal of Smart Home*, vol. 10, no. 5, pp. 285–296, 2016.
- [148] P. T. Manditereza and R. C. Bansal, “Multi-Agent Based Distributed Voltage Control Algorithm for Smart Grid Applications,” *Electric Power Components and Systems*, vol. 44, no. 20, pp. 2352–2363, 2016.
- [149] G. H. Merabet, M. Essaaidi, H. Talei, M. R. Abid, N. Khalil, M. Madkour, and D. Benhaddou, “Applications of Multi-Agent Systems in Smart Grids: A survey,” *2014 International Conference on Multimedia Computing and Systems (ICMCS)*, pp. 1088–1094, 2014. [Online]. Available: <http://ieeexplore.ieee.org/document/6911384/>

- [150] J. Xie and C.-C. Liu, “Multi-agent systems and their applications,” *Journal of International Council on Electrical Engineering*, vol. 7, no. 1, pp. 188–197, 2017. [Online]. Available: <https://www.tandfonline.com/doi/full/10.1080/22348972.2017.1348890>
- [151] C. Yilmaz, S. Albayrak, and L. Marco, “Smart Grid Architectures and the Multi-Agent System Paradigm,” *The Fourth International Conference on Smart Grids, Green Communications and IT Energy-aware Technologies*, no. c, pp. 90–95, 2014. [Online]. Available: <http://www.dai-labor.de/fileadmin/Files/Publikationen/Buchdatei/Yilmaz2014Smart.pdf>
- [152] R. F. Sampaio, L. S. Melo, R. P. Leão, G. C. Barroso, and J. R. Bezerra, “Automatic restoration system for power distribution networks based on multi-agent systems,” *IET Generation, Transmission & Distribution*, vol. 11, no. 2, pp. 475–484, 2017. [Online]. Available: <http://digital-library.theiet.org/content/journals/10.1049/iet-gtd.2016.1018>
- [153] H. Wan, K. K. Li, and K. P. Wong, “An adaptive multiagent approach to protection relay coordination with distributed generators in industrial power distribution system,” *IEEE Transactions on Industry Applications*, vol. 46, no. 5, pp. 2118–2124, 2010.
- [154] P. Peidaee, A. Kalam, and M. H. Moghaddam, “Developing a simulation framework for integrating multi-agent protection system into smart grids,” in *2017 Australasian Universities Power Engineering Conference (AUPEC)*. IEEE, 2017, pp. 1–6.
- [155] C. Liu, Z. Hussain, Z. Chen, and C. Leth, “Multi-agent system based adaptive protection for dispersed generation integrated distribution systems,” *International Journal of Smart Grid and Clean Energy Multi-agent*, 2013.
- [156] M. Nick, R. Cherkaoui, and M. Paolone, “Optimal siting and sizing of distributed energy storage systems via alternating direction method of multipliers,” *2014 Power Systems Computation Conference*, pp. 1–7, 2014. [Online]. Available: <http://ieeexplore.ieee.org/lpdocs/epic03/wrapper.htm?arnumber=7038335>
- [157] V. Sok and T. Tayjasanant, “Determination of optimal siting and sizing of energy storage system in PV-connected distribution systems considering minimum energy losses,” *ECTI-CON 2017 - 2017 14th International Conference on Electrical Engineering/Electronics, Computer, Telecommunications and Information Technology*, no. 2, pp. 451–454, 2017.
- [158] S. Y. Reddy, D. S. Reddy, and G. K. Rao, “Optimal siting and sizing of solar power sources in interconnection grid system,” *Journal of Electrical Engineering*, vol. 16, no. 4, pp. 1–8, 2016.
- [159] M. Jamaly, J. L. Bosch, and J. Kleissl, “Aggregate ramp rates of distributed

- photovoltaic systems in San Diego county,” *IEEE Transactions on Sustainable Energy*, vol. 4, no. 2, pp. 519–526, 2013.
- [160] V. Sok and T. Tayjasanant, “Determination of optimal siting and sizing of energy storage system in PV-connected distribution systems considering minimum energy losses,” *ECTI-CON 2017 - 2017 14th International Conference on Electrical Engineering/Electronics, Computer, Telecommunications and Information Technology*, no. 2, pp. 451–454, 2017.
- [161] M. Mukerji, “Optimal siting and sizing of solar photovoltaic distributed generation to minimize loss, present value of future asset upgrades and peak demand costs on a real distribution feeder,” Master’s thesis, University of Waterloo, 2011.
- [162] L. Luo, W. Gu, X. P. Zhang, G. Cao, W. Wang, G. Zhu, D. You, and Z. Wu, “Optimal siting and sizing of distributed generation in distribution systems with PV solar farm utilized as STATCOM (PV-STATCOM),” *Applied Energy*, vol. 210, no. May 2017, pp. 1092–1100, 2018. [Online]. Available: <https://doi.org/10.1016/j.apenergy.2017.08.165>
- [163] S. Sukumar, H. Mokhlis, S. Mekhilef, M. Karimi, and S. Raza, “Ramp-rate control approach based on dynamic smoothing parameter to mitigate solar PV output fluctuations,” *Int. J. Electr. Power Energy Syst.*, vol. 96, no. September 2017, pp. 296–305, 2018. [Online]. Available: <https://doi.org/10.1016/j.ijepes.2017.10.015>
- [164] W. Jewell and R. Ramakumar, “The effects of moving clouds on electric utilities with dispersed photovoltaic generation,” *IEEE Transactions on Energy Conversion*, vol. EC-2, no. 4, pp. 570–576, 1987.
- [165] W. T. Jewell and T. D. Unruh, “Limits on cloud-induced fluctuation in photovoltaic generation,” *IEEE Transactions on Energy Conversion*, vol. 5, no. 1, pp. 8–14, 1990.
- [166] E. Kern and M. Russell, “Spatial and temporal irradiance variations over large array fields,” *Photovoltaic Specialists Conference*, pp. 1043–1050, 1988. [Online]. Available: [http://ieeexplore.ieee.org/xpls/abs/\\_all.jsp?arnumber=105864](http://ieeexplore.ieee.org/xpls/abs/_all.jsp?arnumber=105864)
- [167] E. Wiemken, H. Beyer, W. Heydenreich, and K. Kiefer, “Power characteristics of PV ensembles: experiences from the combined power production of 100 grid connected PV systems distributed over the area of Germany,” *Solar Energy*, vol. 70, no. 6, pp. 513–518, 2001. [Online]. Available: <http://linkinghub.elsevier.com/retrieve/pii/S0038092X00001468>
- [168] A. E. Curtright and J. Apt, “The character of power output from utility-scale photovoltaic systems,” *Progress in Photovoltaics: Research and Applications*, vol. 16, no. 3, pp. 241–247, may 2008. [Online]. Available:



<http://doi.wiley.com/10.1002/pip.786>

- [169] K. Otani, J. Minowa, and K. Kurokawa, "Study on areal solar irradiance for analyzing areally-totalized pv systems," *Solar Energy Materials and Solar Cells*, vol. 47, no. 1, pp. 281 – 288, 1997. [Online]. Available: <http://www.sciencedirect.com/science/article/pii/S0927024897000500>
- [170] N. Kawasaki, T. Oozeki, K. Otani, and K. Kurokawa, "An evaluation method of the fluctuation characteristics of photovoltaic systems by using frequency analysis," *Solar Energy Materials and Solar Cells*, vol. 90, no. 18-19, pp. 3356–3363, 2006.
- [171] T. E. Hoff and R. Perez, "Modeling PV fleet output variability," *Solar Energy*, vol. 86, no. 8, pp. 2177 – 2189, 2012, progress in Solar Energy 3. [Online]. Available: <http://www.sciencedirect.com/science/article/pii/S0038092X11004154>
- [172] M. Lave, J. Stein, A. Ellis, C. Hansen, and E. Nakashima, "Ota City : Characterizing Output Variability from 553 Homes with Residential PV Systems on a Distribution Feeder," *City*, no. November, 2011.
- [173] R. Perez, M. David, T. Hoff, S. Kivalov, and J. Kleissl, "Spatial and temporal variability of solar energy," *Asrc.Albany.Edu*, no. figure 1, 2015. [Online]. Available: <http://asrc.albany.edu/people/faculty/perez/2015/SEVAR.pdf>
- [174] I. Ziari, G. Ledwich, and A. Ghosh, "A new technique for optimal allocation and sizing of capacitors and setting of ltc," *International Journal of Electrical Power & Energy Systems*, vol. 46, pp. 250–257, 2013.
- [175] J.-H. Choi, S.-J. Ahn, H.-K. Nam, J.-C. Kim, S.-I. Moon, W.-W. Jung, and I.-K. Song, "The coordinate control method of ltc transformer and capacitor banks at distribution substation," *Journal of Electrical Engineering and Technology*, vol. 7, no. 3, pp. 320–329, 2012.
- [176] F. Ding, A. Nagarajan, S. Chakraborty, M. Baggu, A. Nguyen, S. Walinga, M. McCarty, and F. Bell, "Photovoltaic impact assessment of smart inverter volt-var control on distribution system conservation voltage reduction and power quality," NREL (National Renewable Energy Laboratory (NREL), Golden, CO (United States)), Tech. Rep., 2016.
- [177] P. Michael and P. Joe, "Impact of ieee 1547 standard on smart inverters," *IEEE PES Industry Technical Support Task Force, Tech. Rep.*, 2018.
- [178] S. Ghosh, S. Rahman, and M. Pipattanasomporn, "Distribution voltage regulation through active power curtailment with pv inverters and solar generation forecasts," *IEEE Transactions on Sustainable Energy*, vol. 8, no. 1, pp. 13–22, 2017.

- [179] D. G. Photovoltaics and E. Storage, “IEEE standard for interconnection and interoperability of distributed energy resources with associated electric power systems interfaces,” *IEEE Std*, pp. 1547–2018, 2018.
- [180] R. R. Jha, A. Dubey, C. Liu, and K. P. Schneider, “Bi-level Volt-VAR optimization to coordinate smart inverters with voltage control devices,” *IEEE Transactions on Power Systems*, vol. 34, no. 3, pp. 1801–1813, May 2019.
- [181] M. Farivar, C. R. Clarke, S. H. Low, and K. M. Chandy, “Inverter var control for distribution systems with renewables,” in *Proc. IEEE International Conference on Smart Grid Communications (SmartGridComm)*, 2011, pp. 457–462.
- [182] C. Zhang and Y. Xu, “Hierarchically-Coordinated Voltage/VAR Control of Distribution Networks Using PV Inverters,” *IEEE Transactions on Smart Grid*, vol. 11, no. 4, pp. 2942–2953, 2020.
- [183] Q. Yang, G. Wang, A. Sadeghi, G. B. Giannakis, and J. Sun, “Two-timescale voltage control in distribution grids using deep reinforcement learning,” *IEEE Transactions on Smart Grid*, vol. 11, no. 3, pp. 2313–2323, 2020.
- [184] F. Ding and M. Baggu, “Coordinated use of smart inverters with legacy voltage regulating devices in distribution systems with high distributed pv penetration — increase cvr energy savings,” *IEEE Transactions on Smart Grid*, pp. 1–1, 2018.
- [185] X. Sun, J. Qiu, and J. Zhao, “Optimal local volt/var control for photovoltaic inverters in active distribution networks,” *IEEE Transactions on Power Systems*, pp. 1–1, 2021.
- [186] X. Sun and J. Qiu, “Two-stage volt/var control in active distribution networks with multi-agent deep reinforcement learning method,” *IEEE Transactions on Smart Grid*, pp. 1–1, 2021.
- [187] M. Ebeed, S. Kamel, and F. Jurado, “Chapter 7 - optimal power flow using recent optimization techniques,” in *Classical and Recent Aspects of Power System Optimization*, A. F. Zobaa, S. H. Abdel Aleem, and A. Y. Abdelaziz, Eds. Academic Press, 2018, pp. 157–183. [Online]. Available: <https://www.sciencedirect.com/science/article/pii/B9780128124413000070>
- [188] S. Jothibasu and S. Santoso, “Sensitivity analysis of photovoltaic hosting capacity of distribution circuits,” in *2016 IEEE Power and Energy Society General Meeting (PESGM)*, 2016, pp. 1–5.
- [189] K. H. Youssef, “A new method for online sensitivity-based distributed voltage control and short circuit analysis of unbalanced distribution feeders,” *IEEE Transactions on Smart Grid*, vol. 6, no. 3, pp. 1253–1260, 2015.

- [190] M. Ahmed, R. Bhattarai, S. J. Hossain, S. Abdelrazek, and S. Kamalasadán, “Coordinated voltage control strategy for voltage regulators and voltage source converters integrated distribution system,” *IEEE Transactions on Industry Applications*, vol. 55, no. 4, pp. 4235–4246, 2019.
- [191] K. M. Muttaqi, A. D. T. Le, M. Negnevitsky, and G. Ledwich, “A coordinated voltage control approach for coordination of oltc, voltage regulator, and dg to regulate voltage in a distribution feeder,” *IEEE Transactions on Industry Applications*, vol. 51, no. 2, pp. 1239–1248, 2015.
- [192] C. Li, V. R. Disfani, H. V. Haghi, and J. Kleissl, “Optimal voltage regulation of unbalanced distribution networks with coordination of oltc and pv generation,” in *Proc. 2019 IEEE Power Energy Society General Meeting (PESGM)*, 2019, pp. 1–5.
- [193] L. Gan, N. Li, U. Topcu, and S. H. Low, “Exact convex relaxation of optimal power flow in radial networks,” *IEEE Transactions on Automatic Control*, vol. 60, no. 1, pp. 72–87, 2015.
- [194] R. A. Jabr, “Robust volt/var control with photovoltaics,” *IEEE Transactions on Power Systems*, vol. 34, no. 3, pp. 2401–2408, 2019.
- [195] J. Seuss, M. J. Reno, R. J. Broderick, and S. Grijalva, “Analysis of pv advanced inverter functions and setpoints under time series simulation,” *Sandia National Laboratories SAND2016-4856*, 2016.
- [196] “Opti toolbox probs/mixed integer nonlinear program (minlp),” <https://www.inverseproblem.co.nz/OPTI/index.php/Probs/MINLP>, (Accessed on 04/07/2021).
- [197] M. Jafaritarposhti, S. H. Fathi, and H. A. Abyaneh, “Impact of critical clearing time on over-current relays coordination in a multi-machine power system in presence of resistive sfcl,” in *11th International Conference on Protection and Automation in Power System, Iran University of Science and Technology*, 2017.
- [198] D. Garcia, J. Valencia, and G. Hausman, “2016 Department of Energy efficiency requirements for distribution transformers,” EATON, Tech. Rep., 01 2016.
- [199] M. A. Bahmani, T. Thiringer, and M. Kharezy, “Design methodology and optimization of a medium-frequency transformer for high-power dc–dc applications,” *IEEE Transactions on Industry Applications*, vol. 52, no. 5, pp. 4225–4233, Sep. 2016.
- [200] R. Petkov, “Optimum design of a high-power, high-frequency transformer,” *IEEE Trans. Power Electron.*, vol. 11, no. 1, pp. 33–42, 1996.

- [201] M. Mogorovic and D. Dujic, "Medium frequency transformer leakage inductance modeling and experimental verification," in *2017 IEEE Energy Conversion Congress and Exposition (ECCE)*, Oct 2017, pp. 419–424.
- [202] —, "100 kw, 10 khz medium-frequency transformer design optimization and experimental verification," *IEEE Transactions on Power Electronics*, vol. 34, no. 2, pp. 1696–1708, Feb 2019.
- [203] H. Chen and D. Divan, "High-frequency transformer design for the soft-switching solid state transformer (s4t)," in *2017 IEEE Applied Power Electronics Conference and Exposition (APEC)*, March 2017, pp. 2534–2541.
- [204] Y. Xu, L. Chen, W. Guo, C. Shangguan, J. Zuo, and K. He, "Optimal design of medium-frequency fe-based amorphous transformer based on genetic algorithm," *IEEE Transactions on Plasma Science*, vol. 46, no. 10, pp. 3240–3248, 2018.
- [205] T. O. Olowu, H. Jafari, M. Moghaddami, and A. I. Sarwat, "Physics-based design optimization of high frequency transformers for solid state transformer applications," in *2019 IEEE Industry Applications Society Annual Meeting*, 2019, pp. 1–6.
- [206] W. G. Hurley and W. H. Wölfle, *Transformers and Inductors for Power Electronics: Theory, Design and Applications*. John Wiley & Sons, 2013.
- [207] K. D. Hoang and J. Wang, "Design optimization of high frequency transformer for dual active bridge DC-DC converter," *Proc. - 2012 20th Int. Conf. Electr. Mach. ICEM 2012*, pp. 2311–2317, 2012.
- [208] F. Tourkhani and P. Viarouge, "Accurate analytical model of winding losses in round litz wire windings," *IEEE Transactions on Magnetics*, vol. 37, no. 1, pp. 538–543, Jan 2001.
- [209] R. Chang, C. Chen, C. Wang, and Y. Tzou, "Calculation of losses and temperature rise for high frequency transformer under forced-air convection," in *IECON 2010 - 36th Annual Conference on IEEE Industrial Electronics Society*, Nov 2010, pp. 1–6.
- [210] Hitachi Metals America, Ltd, "Powerlite® c-cores." [Online]. Available: <https://www.hitachimetals.com/materials-products/amorphous-nanocrystalline/powerlite-c-cores.php>
- [211] A. Ehsanifar, M. Dehghani, and M. Allahbakhshi, "Calculating the leakage inductance for transformer inter-turn fault detection using finite element method," in *2017 Iranian Conference on Electrical Engineering (ICEE)*, May 2017, pp. 1372–1377.
- [212] H. F. Farahani, "Finite element analysis to find the optimal windings ar-

rangements for reduction of leakage inductance in high frequency transformers,” *Australian Journal of Basic and Applied Sciences*, vol. 5, no. 11, pp. 219–227, 2011.

- [213] Z. Ouyang, O. C. Thomsen, and M. A. Andersen, “The analysis and comparison of leakage inductance in different winding arrangements for planar transformer,” in *2009 International Conference on Power Electronics and Drive Systems (PEDS)*. IEEE, 2009, pp. 1143–1148.
- [214] H. Choi, “Analysis and design of llc resonant converter with integrated transformer,” in *APEC 07 - Twenty-Second Annual IEEE Applied Power Electronics Conference and Exposition*, Feb 2007, pp. 1630–1635.
- [215] S. Abdel-Rahman, “Resonant llc converter: Operation and design,” *Infineon Technologies North America (IFNA) Corp.*, 2012.
- [216] M. Moghaddami and A. Sarwat, “Time-dependent multi-physics analysis of inductive power transfer systems,” in *2018 IEEE Transportation Electrification Conference and Expo (ITEC)*, June 2018, pp. 130–134.
- [217] M. Moghaddami, A. I. Sarwat, and F. De Leon, “Reduction of Stray Loss in Power Transformers Using Horizontal Magnetic Wall Shunts,” *IEEE Trans. Magn.*, vol. 53, no. 2, 2017.
- [218] M. Moghaddami, A. Anzalchi, and A. I. Sarwat, “Finite element based design optimization of magnetic structures for roadway inductive power transfer systems,” in *2016 IEEE Transportation Electrification Conference and Expo (ITEC)*, June 2016, pp. 1–6.
- [219] COMSOL Multiphysics, “Heat transfer module user’s guide,” June 2019.
- [220] C. Multiphysics, “Introduction to comsol multiphysics®,” *COMSOL Multiphysics, Burlington, MA, accessed Feb*, vol. 9, p. 2018, 1998.
- [221] COMSOL Multiphysics, “Cfd module user’s guide,” June 2019.
- [222] M. Moghaddami and A. I. Sarwat, “Single-phase soft-switched ac–ac matrix converter with power controller for bidirectional inductive power transfer systems,” *IEEE Transactions on Industry Applications*, vol. 54, no. 4, pp. 3760–3770, 2018.
- [223] S. Dharmasena, T. O. Olowu, and A. I. Sarwat, “Bidirectional ac/dc converter topologies: A review,” in *2019 SoutheastCon*, 2019, pp. 1–5.
- [224] Y. Liu, Y. Liu, B. Ge, and H. Abu-Rub, “Interactive grid interfacing system by matrix-converter-based solid state transformer with model predictive control,” *IEEE Transactions on Industrial Informatics*, vol. 16, no. 4, pp. 2533–2541, 2020.

- [225] Y. Liu, Y. Liu, H. Abu-Rub, B. Ge, R. S. Balog, and Y. Xue, "Model predictive control of a matrix-converter based solid state transformer for utility grid interaction," in *2016 IEEE Energy Conversion Congress and Exposition (ECCE)*, 2016, pp. 1–6.
- [226] Y. Liu, Y. Liu, H. Abu-Rub, and B. Ge, "Model predictive control of matrix converter based solid state transformer," in *2016 IEEE International Conference on Industrial Technology (ICIT)*, 2016, pp. 1248–1253.
- [227] H. J. Cha and P. N. Enjeti, "A three-phase ac/ac high-frequency link matrix converter for vsfc applications," in *IEEE 34th Annual Conference on Power Electronics Specialist, 2003. PESC '03.*, vol. 4, 2003, pp. 1971–1976 vol.4.
- [228] H. Keyhani, H. A. Toliyat, M. Harfman-Todorovic, R. Lai, and R. Datta, "An isolated resonant ac-link three-phase ac–ac converter using a single hf transformer," *IEEE Transactions on Industrial Electronics*, vol. 61, no. 10, pp. 5174–5183, 2014.
- [229] K. Basu and N. Mohan, "A single-stage power electronic transformer for a three-phase pwm ac/ac drive with source-based commutation of leakage energy and common-mode voltage suppression," *IEEE Transactions on Industrial Electronics*, vol. 61, no. 11, pp. 5881–5893, 2014.
- [230] K. Koiwa, J. Itoh, and M. Shioda, "Improvement of waveform for high frequency ac-linked matrix converter with svm based on virtual indirect control," in *2015 IEEE Applied Power Electronics Conference and Exposition (APEC)*, 2015, pp. 3359–3366.
- [231] K. Inoue, M. Shioda, M. Katade, A. Goto, S. Morishita, J. Itoh, and K. Koiwa, "Space vector modulation based on virtual indirect control for high frequency ac-linked matrix converter," in *2014 International Power Electronics Conference (IPEC-Hiroshima 2014 - ECCE ASIA)*, 2014, pp. 130–137.
- [232] M. N. Kheraluwala, R. W. Gascoigne, D. M. Divan, and E. D. Baumann, "Performance characterization of a high-power dual active bridge dc-to-dc converter," *IEEE Transactions on Industry Applications*, vol. 28, no. 6, pp. 1294–1301, Nov 1992.
- [233] H. Bai and C. Mi, "Correction to "eliminate reactive power and increase system efficiency of isolated bidirectional dual-active-bridge dc–dc converters using novel dual-phase-shift control" [nov 08 2905-2914]," *IEEE Transactions on Power Electronics*, vol. 27, no. 9, pp. 4177–4177, Sep. 2012.
- [234] F. Krismer and J. W. Kolar, "Accurate small-signal model for the digital control of an automotive bidirectional dual active bridge," *IEEE Transactions on Power Electronics*, vol. 24, no. 12, pp. 2756–2768, Dec 2009.

- [235] Y. Shen, X. Sun, W. Li, X. Wu, and B. Wang, “A modified dual active bridge converter with hybrid phase-shift control for wide input voltage range,” *IEEE Transactions on Power Electronics*, vol. 31, no. 10, pp. 6884–6900, Oct 2016.
- [236] B. Zhao, Q. Yu, and W. Sun, “Extended-phase-shift control of isolated bidirectional dc–dc converter for power distribution in microgrid,” *IEEE Transactions on Power Electronics*, vol. 27, no. 11, pp. 4667–4680, Nov 2012.
- [237] G. Oggier, G. O. García, and A. R. Oliva, “Modulation strategy to operate the dual active bridge dc-dc converter under soft switching in the whole operating range,” *IEEE Transactions on Power Electronics*, vol. 26, no. 4, pp. 1228–1236, April 2011.
- [238] Y. Shen, H. Wang, A. Al-Durra, Z. Qin, and F. Blaabjerg, “A structure-reconfigurable series resonant dc–dc converter with wide-input and configurable-output voltages,” *IEEE Transactions on Industry Applications*, vol. 55, no. 2, pp. 1752–1764, 2019.
- [239] F. Musavi, M. Craciun, D. S. Gautam, W. Eberle, and W. G. Dunford, “An llc resonant dc–dc converter for wide output voltage range battery charging applications,” *IEEE Transactions on Power Electronics*, vol. 28, no. 12, pp. 5437–5445, 2013.
- [240] X. Zhao, L. Zhang, R. Born, and J. Lai, “A high-efficiency hybrid resonant converter with wide-input regulation for photovoltaic applications,” *IEEE Transactions on Industrial Electronics*, vol. 64, no. 5, pp. 3684–3695, 2017.
- [241] H. Wu, T. Mu, X. Gao, and Y. Xing, “A secondary-side phase-shift-controlled llc resonant converter with reduced conduction loss at normal operation for hold-up time compensation application,” *IEEE Transactions on Power Electronics*, vol. 30, no. 10, pp. 5352–5357, 2015.
- [242] T. LaBella, W. Yu, J. Lai, M. Senesky, and D. Anderson, “A bidirectional-switch-based wide-input range high-efficiency isolated resonant converter for photovoltaic applications,” *IEEE Transactions on Power Electronics*, vol. 29, no. 7, pp. 3473–3484, 2014.
- [243] Mao Xingkui, Huang Qisheng, Ke Qingbo, Xiao Yudi, Zhang Zhe, and M. A. E. Andersen, “Grid-connected photovoltaic micro-inverter with new hybrid control llc resonant converter,” in *IECON 2016 - 42nd Annual Conference of the IEEE Industrial Electronics Society*, 2016, pp. 2319–2324.
- [244] S. Shao, Y. Li, J. Sheng, C. Li, W. Li, J. Zhang, and X. He, “A modular multilevel resonant dc–dc converter,” *IEEE Transactions on Power Electronics*, vol. 35, no. 8, pp. 7921–7932, 2020.
- [245] A. Chub, A. Bakeer, and D. Vinnikov, “Step-up series-resonant dc-dc con-

verter with switched mode rectifier operating at fixed switching frequency,” in *2020 IEEE 11th International Symposium on Power Electronics for Distributed Generation Systems (PEDG)*, 2020, pp. 597–601.



## VITA

### TEMITAYO OLAYEMI OLOWU

Born in, Lagos, Nigeria

- 2001                   OND, Electrical and Electronics Engineering  
The Federal Polytechnic Ado-Ekiti  
Ekiti, Nigeria
- 2005                   HND, Electrical and Electronics Engineering  
The Federal Polytechnic Ado-Ekiti  
Ekiti, Nigeria
- 2010                   B.Eng, Electrical and Electronics Engineering  
University of Benin, Benin City  
Nigeria
- 2015                   M.Eng, Electrical and Electronics Engineering  
University of Benin, Benin City  
Nigeria
- 2020                   MS, Electrical Engineering  
Florida International University, Miami, FL  
Miami, United States
- 2021                   PhD, Electrical Engineering  
Florida International University, Miami, FL  
Miami, United States

### PUBLICATIONS AND PRESENTATIONS

For full list of publication, please visit:

[https://scholar.google.com/citations?hl=en&user=-vDgYk8AAAAJ&view\\_op=list\\_works&sortby=pubdate](https://scholar.google.com/citations?hl=en&user=-vDgYk8AAAAJ&view_op=list_works&sortby=pubdate)